Democratic and Popular Republic of Algeria

Ministry of Higher Education and Scientific Research

University of Kasdi Merbah, Ouargla

Faculty of new information and communication technologies

Department of Electronics and Telecommunications

Thesis Submitted to the Department of Electronics and telecommunications in
Candidacy for Candidacy for the Degree of “Doctor” 3rd Cycle LMD in Telecommunications
System

Theme

Multimodality image registration and fusion techniques using meta-heuristic algorithm based approaches

Presented by: Hedifa Dida

Committee members

Fouad	Chebbara	Pr	Ouargla University	President
Fella	Charif	MCA	Ouargla University	Supervisor
Abderrazak	Benchabane	MCA	Ouargla University	Co - Supervisor
Djamel	Samai	MCA	Ouargla University	Examiner
Messaoud	Hettiri	MCA	Eloued University	Examiner
Riadh	Ajgou	MCA	Eloued University	Examiner

Academic Year: 2022/2023

Dedication

This thesis will be completed after mentioning the support of my beloved and dear mother. I dedicate this thesis to my dear mother "Salima" and my brothers for their love and support throughout my life.

I also dedicate this thesis to the lights of my life: the sons of my brother Salima and Sharaf Eddin.

I dedicate this thesis to all my family, To all my friends To all those who were giving me any kind of support.

Acknowledgments

First and foremost, praise and thanks to ALLAH the sacred and the mighty for giving me the ability and helping me in accomplishing this thesis.

Then, I would like to express my sincerest gratitude to my supervisors Dr. Charif Fella and Benchabane Abderrazak for his continuous support, help, guidance, motivation and patience throughout this thesis.

My sincere thanks also go to Pr. Chebbara Fouad and Dr. Samai Djamel who provided me the opportunity to join the PhD study. I acknowledge them for their encouragement, motivation, advice and insight.

A very special thanks go to the honorable members of my dissertation committee who accepted to examine and evaluate this thesis, namely, Dr. Hettiri Messaoud and Dr. Ajgou Riadh from El Oued university; Dr. Chebbara Fouad and. Dr. Samai Djamel from the university of Ouargla.

I also acknowledge my gratitude to Dr. Khaled Bensid, Head of the Electronics and Telecommunications Department, for his support in completing this thesis.

ABSTRACT

Since the emergence of the process of registration and fusion images, research has increased rapidly due to the importance of this technology and the need for it in all fields. The success of this process depends mainly on the effectiveness of the method used. Therefore, the use of an effective method to carry out this process is the main objective of this study. This process aims to provide an image with complementary information that facilitates the analysis process. Many methods have been adopted for recording and merging images, but most of them lead to undesirable effects such as distortions that appear in the resulting image. In this thesis, we present a new method for image registration with optimization-based meta-heuristic algorithms. On the other hand, an effective method for multi-focus image fusion was adopted based on the fast guided filter. Due to the medical field's need for an adequate image to diagnose special diseases, including incurable tumors, the proposed approach has been applied to medical images. On the other hand, with the emergence of Covid-19, these methods were applied to the pictures of the person with Covid-19 to facilitate the process of diagnosing infection with this disease. The proposed approaches have greatly contributed to providing computed tomography (CT) images of the visible quality of the lungs of COVID-19 patients, facilitating rapid diagnosis of the disease. The same for the proposed approaches of image fusion have contributed to overcoming the defects of image sensors through multi-focus image fusion. In addition, images from various imaging technologies are fused to facilitate the diagnosis process. Through the obtained results, the proposed methods for recording and merging various images showed high accuracy and speed compared to other modern methods.

Keywords: Image Registration, Image Fusion, Meta-heuristic, Optimization, Medical Image, Guided Filter.

RESUME

Depuis l'émergence du procédé de recalage et de fusion d'images, la recherche s'est rapidement développée en raison de l'importance de cette technique et de son besoin dans tous les domaines. Le succès de ce processus dépend principalement de l'efficacité de la méthode utilisée. Par conséquent, l'utilisation d'une méthode efficace pour mener à bien ce processus est l'objectif principal de cette étude. Ce processus vise à fournir une image avec des informations complémentaires qui facilitent le processus d'analyse. De nombreuses méthodes ont été adoptées pour enregistrer et fusionner des images, mais la plupart d'entre elles conduisent à des effets indésirables tels que des distorsions qui apparaissent dans l'image résultante. Dans cette thèse, nous présentons une nouvelle méthode de recalage d'images avec des algorithmes méta-heuristiques basés sur l'optimisation. D'autre part, une méthode efficace de fusion d'images multi-focus a été adoptée sur la base du filtre guidé rapide. En raison du besoin du domaine médical d'une image adéquate pour diagnostiquer des maladies particulières, y compris des tumeurs incurables, l'approche proposée a été appliquée aux images médicales. D'autre part, avec l'émergence du Covid-19, ces méthodes ont été appliquées aux photos de la personne atteinte du Covid-19 pour faciliter le processus de diagnostic de l'infection par cette maladie. Les approches proposées ont grandement contribué à fournir des images de tomodensitométrie (TDM) de la qualité visible des poumons des patients COVID-19, facilitant le diagnostic rapide de la maladie. De même pour les approches proposées de fusion d'images ont contribué à pallier les défauts des capteurs d'images grâce à la fusion d'images multi-focal. De plus, les images de diverses technologies d'imagerie sont fusionnées pour faciliter le processus de diagnostic. A travers les résultats obtenus, les approches proposées pour recaler et fusionner diverses images ont montré une précision et une vitesse élevées par rapport aux autres méthodes modernes.

Mots clés : Recalage d'images, Fusion d'images, Méta-heuristique, Optimisation, Image médicale, Filtre guidé.

الملخص

منذ ظهور عملية التسجيل ودمج الصور، ازداد البحث بشكل سريع نظرا لأهمية هذه التقنية والحاجة إليها في كافة المجالات. يعتمد نجاح هذه العملية بشكل أساسي على فعالية الطريقة المستخدمة. لذلك، فإن استخدام طريقة فعالة لتنفيذ هذه العملية هو الهدف الرئيسي لهذه الدراسة. تهدف هذه العملية إلى توفير صورة بمعلومات تكميلية تسهل عملية التحليل. تم اعتماد العديد من الطرق لتسجيل الصور ودمجها، ولكن معظمها يؤدي إلى تأثيرات غير مرغوب فيها مثل التشوهات التي تظهر في الصورة الناتجة. في هذه الرسالة، نقدم طريقة جديدة لتسجيل الصور باستخدام خوارزميات الكشف عن مجريات الأمور القائمة على التحسين. من ناحية أخرى، تم اعتماد طريقة فعالة لدمج الصور متعددة التركيز بناءً على المرشح السريع التوجيه. نظرًا لحاجة المجال الطبي إلى صورة مناسبة لتشخيص الأمراض الخاصة، بما في ذلك الأورام المستعصية، فقد تم تطبيق النهج المقترح على الصور الطبية. من ناحية أخرى، ومع ظهور فيروس كورونا Covid-19، تم تطبيق هذه الأساليب على صور الشخص المصاب بـ Covid-19 لتسهيل عملية تشخيص الإصابة بهذا المرض. لقد ساهمت الأساليب المقترحة بشكل كبير في توفير صور التصوير المقطعي المحوسب (CT) ذات الجودة المرئية لرئتي مرضى COVID-19، مما يسهل التشخيص السريع للمرض. وبالمثل، ساهمت أساليب دمج الصور المقترحة في التغلب على أوجه القصور في مستشعرات الصورة بفضل دمج الصور متعدد البؤر. بالإضافة إلى ذلك، يتم دمج الصور من تقنيات التصوير المختلفة للمساعدة في عملية التشخيص. من خلال النتائج التي تم الحصول عليها، أظهرت الأساليب المقترحة للتسجيل ودمج الصور المختلفة دقة وسرعة عالية مقارنة بالطرق الحديثة الأخرى.

الكلمات الدالة: تسجيل الصور، دمج الصور، الكشف عن مجريات الأمور، التحسين، الصورة الطبية، المرشح الإرشادي.

CONTENTS

CHAPTER 1 INTRODUCTION

CHAPTER 2 GENERALITIES ON IMAGE REGISTRATION AND FUSION

CHAPTER 3. META-HEURISTIC METHODS FOR OPTIMIZATION

CHAPTER 4. IMAGE REGISTRATION BASED ON META-HUEURSTIC ALGORITHMS

CHAPTER 5. MULTI MODAL IMAGE FUSION RESULTS OF: MULTI FOCUS IMAGES AND MEDICAL IMAGES

LISTE OF FIGURES

LISTE OF TABLES

Nomenclatures

CT	Computer Tomography
COVID-19	COronaVIrus Disease
CBF	Cross-Bilateral Filter
CNN	Convolutional neural network
FGF	Fast Guided Filter
GF	Guided Filter
GWO	Grey wolf optimizer
GGO	Ground-Glass Opacity
HPSGWO	Hybrid PSO-GWO
IF	Image Fusion
IR	Image Registration
ISCA	Improved Sine Cosine Algorithm
ICA	Independent Component Analysis
IFGD	Image Fusion using luminance gradients
MI	Mutual Information
MRI	Magnetic Resonance Imaging
MACBFF	Multiscale Alternative approach to Cross Bilateral Filter
MSMFM	Multi-sacle Morphological Focus Measure
PET	Positron Emission Tomography
PSO	Particle swarm optimization
PCA	Principle Component Analysis
SCA	Sine Cosine algorithm
SSIM	Structural SImilarity Metric
SPECT	Single Photon Emission Tomography
WSSM	Wavelet Based Statistical Sharpness Measure

1.1. Introduction

In recent years, the technology side has witnessed rapid growth in various fields and touched different aspects of human life, especially those related to imaging techniques. With the emergence of advanced imaging (Ex. smart phones, laptops and smart photography equipment) devices that accompany the individual wherever he goes and documents many of the events facing him, the image has become of great importance. This importance appears through the information presented by the target image, and the individual needs it to communicate and exchange congratulations on occasions, as well as express his condition. The human need for imaging technologies expands to other fields, such as medical imaging, satellite imaging, electronics, and robotics, etc. In the medical field, the radiologist, in diagnosing incurable diseases and tumors, relies on imaging techniques that show them clarifying information about the disease. This information varies according to the different imaging techniques used, for example, positron emission tomography (PET), single photon emission tomography (SPECT), computer tomography (CT), and magnetic resonance imaging (MRI) all imaging techniques that have had a major role in the development of the field of medicine and overcoming the consequences of diagnosing diseases. On the other hand, the electronic field needs the image in many aspects, especially those related to the printed circuit boards (PCB). The machine that produces this type of circuit treats it as an image so that these elements are printed on an electronic board, and in the end, a printed circuit board is obtained. This is only related to the medical and electronic fields and there are many fields that depend on an image, these two areas have been explained as an example but are not limited. Despite all this development in imaging techniques in various fields and their widespread use, the question arises whether the image produced by these techniques contains sufficient information in all cases?, Or, in other words, do these images need processing after they are produced?

Image registration and fusion are techniques that have been widely used that align the corresponding features in some sensed images with respect to a reference and provide a more representative output image by merging the input images with each other, respectively. **Figure 1-1** shows the evolution of the image fusion process in recent years. Achieving effective registration and fusion of target images mainly depends on the method used in this process. The adoption of a method with high accuracy in fusion and speed in performance will have a major role in facilitating the process of analyzing these images. The same thing with regard to image registration, providing an effective optimization algorithm ensures good registration of the input images.

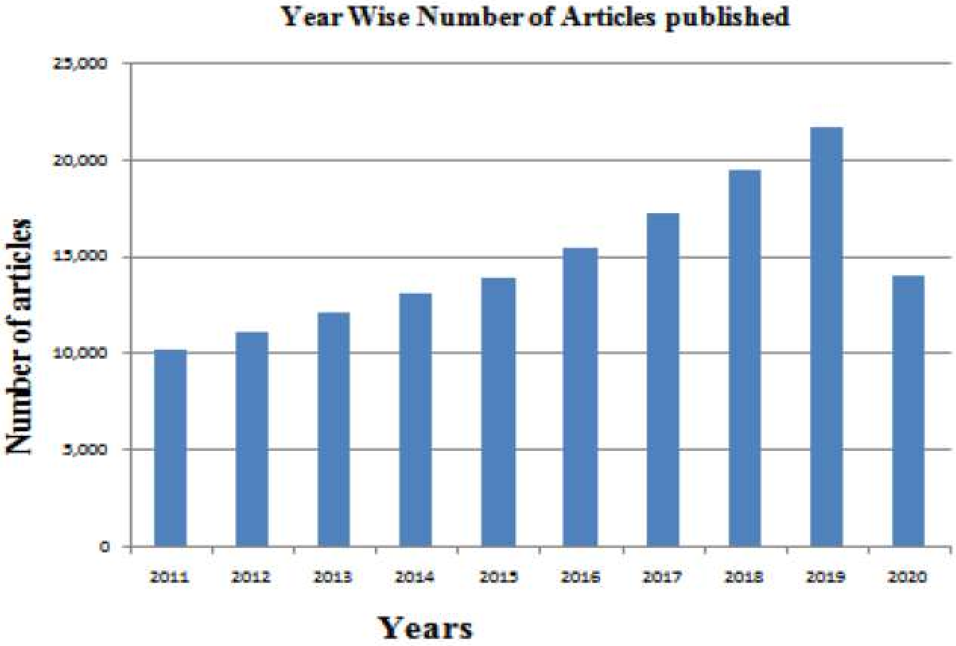

Figure 1-1 The number of articles related to image fusion in recent years [1].

1.2. Statement of the problem

Up to now, the field of image analysis has witnessed many developments in images registration and fusion methods. Generally, Image registration methods can be classified into two categories rigid and non-rigid [2], while image fusion methods is classified into three basic categories pixel-level, feature-level and decision-level [3] . In image registration, this process is carried out within a number of steps, the most important of which is the optimization step. The optimization process finds the optimum transformation based on the initial parameters to achieve efficient registration. Many methods have been used to register images, but most of them do not achieve the required quality in the resulting image and contain unwanted distortions, which makes the analysis process difficult. The same goes for image fusion. Several methods have been provided to achieve an effective fusion of source images. These methods have been used in many fields and have played a major role in the development of many fields, especially those related to the medical aspect and the process of diagnosing diseases as shown in **Figure 1-2**. Despite the development of the methods of image fusion and their widespread use in various fields, they remain limited and result in a loss of information during the fusion process. In addition, unwanted defects appear in the fused image. Therefore, we used and developed a new meta-heuristic algorithm of optimization and took advantage of their features to achieve optimal registration on the one hand, and apply new effective methods to provide a fused image with sufficient supplementary information on the other hand.

The main objective of our work is to use meta-heuristic optimization algorithms in image registration and develop new algorithms to provide a registered image with complementary information that facilitates its processing in various fields. On the other hand, it aims to develop new methods to combine images.

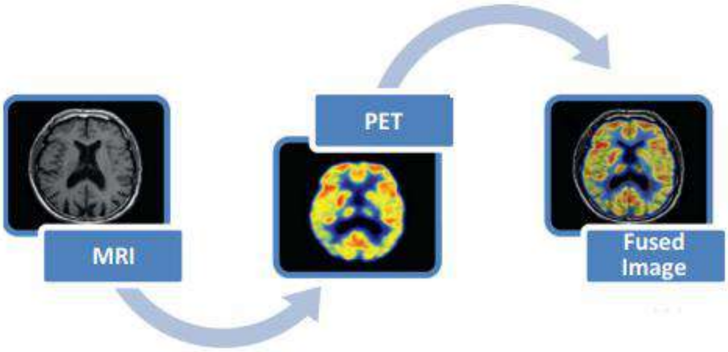

(a) The first modality

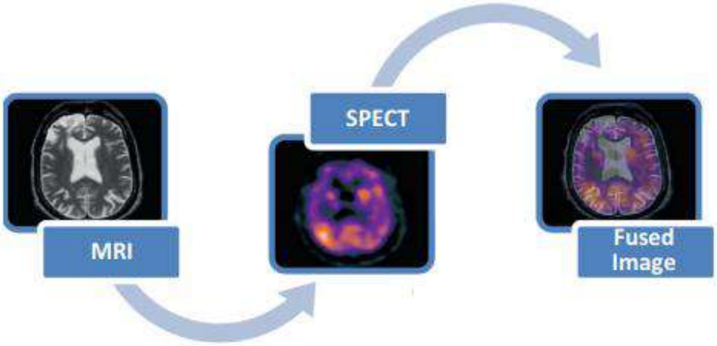

(b) The second modality

Figure 1-2 Examples of fusion of medical imaging modalities.

1.3. Area contribution

Due to the problem of providing a registered image with perfect transformation, as well as the absence of an effective method to provide effective image fusion, the field of image analysis continues to suffer in various fields. In this thesis, we propose a new approach for image registration based on meta-heuristic algorithms and used new methods to achieve an effective fusion of images. To achieve this goal, the guiding optimization algorithm was applied, which is a class of intelligent, self-algorithms for finding near-optimum solutions to hard optimization problems, mimicking intelligent processes and behaviors observed from nature, sociology, thinking, and other disciplines [4]. On the other hand, the fast guided filter has been applied for multi-focus image fusion and provides an image free from the part of the blur caused by the defects of modern imaging sensors. Moreover, a cross binary filter has been used for multi-modal image fusion to obtain a base layer by looking at another image for guiding purposes.

This thesis makes significant contributions in the following areas:

- The application of many meta-heuristics algorithms (PSO, GWO, SCA, CSA, ABC, and FA), especially the modern ones, to achieve a near-perfect registration of medical images and images of printed circuit boards.

- Application of gray wolf and sine cosine algorithms for image registration of printed circuit boards aimed at minimizing ruin to these circuits by providing a high-quality image.
- Application of gray wolf algorithm for multi-modal image registration between computed tomography (CT) and magnetic resonance (MR) images.
- Develop a new meta-heuristics algorithm (HPSGWO) and apply it to computerized tomography (CT) images of a lung infected with COVID-19, with the aim of providing an image that facilitates the diagnosis of this serious disease.
- Use a Multi-modal Alternative approach to cross bilateral filter (MACBFF) for multi-modal medical image fusion. In this case, of the study, it was applied for a fusion of several medical images (The images fused: CT, MRI, PET, SPECT).
- Application of fast guided filter for multi-focus image fusion based on focus region detection.

1.4. Thesis organization

The thesis is organized as follows, with the exception of the first chapter, which contains a general introduction:

- The second chapter is dedicated to introduce a general explanation of the technique of registration and fusion images. Definition of image fusion, image fusion categorization, multi focus image fusion and approaches of image fusion. Then image registration, image registration model and framework, image registration techniques, registration evaluation metrics, finally and advantages and disadvantages of image fusion..

- The third chapter included an explanation of meta-heuristic algorithms and their types, some famous algorithms and applications of meta-heuristic algorithms. Then we are here interested in the meta-heuristics algorithms, their definition, giving a classification of the meta-heuristics algorithms, the meta-heuristics algorithms used in image registration, and finally the applications of the meta-heuristic algorithms.

- In the fourth chapter, we present the results of image registration based on the proposed method. Firstly, includes the experimental setup that contains the databases used. Second, the experimental results are divided into three sections. The first section shows the results of applying the grey wolf optimizer algorithm in CT and MRI image registration. The second section shows the first developed method HPSWGO and the results it achieved in CT images registration of the lung of a COVID-19 patient. While the third section shows the second developed method ISCA and the results it achieved in CT images registration of the lung of a COVID-19 patient.

- The fifth chapter is devoted to image fusion. We first explained the image databases used in the fusion process based on the proposed methods. Second, the proposed method of multi-focus image fusion based on focus region detection and fast guided filter is presented, then an analysis of parameters, and finally qualitative and quantitative analysis of the proposed method. Third, presented multi-modal medical image fusion based on a multi-scale alternative approach to cross-bilateral filter. We started this section with decomposition and reconstruction by the CBF. Then the proposed method. Finally, qualitative and quantitative analysis of the second proposed method.

2.1. Introduction

Image fusion (IF) is an emerging field in image processing fields in which generating an informative image with the integration of images obtained by different sensors for decision making [3]. Effective image fusion achieves the preservation of vital information by extracting all the important information from the images without producing any inconsistencies in the resulting image. This resulting or fused image is considered more suitable for human and machine perception. The most important step in the image fusion process is the image registration (IR). IR is the process of calculation of a spatial transformation function between two images to be superimposed on the optimum of their resemblance criteria [5]. On the other hand, image registration (IR) is an important process because it provides images with complementary information by aligning the sensible image with high accuracy with the reference image. This process plays an important role in the multi-temporal analysis, multi-modal analysis, and scene to model registration [3].

This chapter aims to introduce the registration and fusion of images and explain the different levels and methods in detail. We also present the various measures of measuring the effectiveness of these two processes, as well as their We also present the various metrics for measuring the effectiveness of these two processes, as well as their advantages and disadvantages.

2.2. Image fusion

Image fusion is a process of combining useful and complementary information of source images into a single image called a fused image (FI). Image fusion, by definition, can fusion significant information from many source images to create a single image contains richer information and is more beneficial for subsequent applications [5]. IF is not only a simple overlay of multiple images and just can create a new image with more valuable information, but this technology belongs to the fusion of visual information in multi-sensor information fusion. It uses computer technology to process multi-modal images after choosing a database to frame the same scene or different scenes, so as to maximize the effective information obtained from these scenes.

The process of fusion goes through important stages to apply this technique, these stages are presented as follows:

- Image registration
- Fusion processing
- Performance evalution
- Fused image

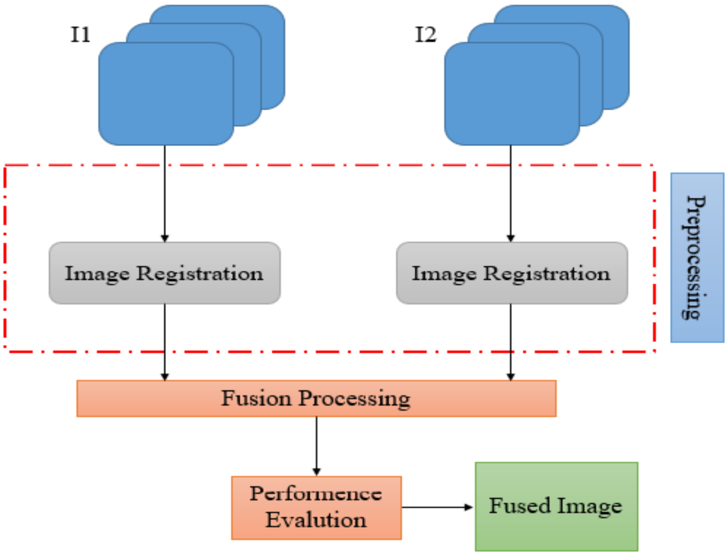

Figure 2-1 General schema of image fusion process.

2.2.1. Image fusion categorization

Initially, the fundamental goal of fusion was to allow humans to observe and make decisions. The first and simplest type of fusion is pixel averaging. Despite the simplicity of this form, it is unsatisfactory, provides artifacts, and leads to the abolition of the pattern and the reduction of contrast, resulted in the emergence of new forms. There are three fundamental levels for images fusion [5], Pixel-Level fusion, Feature-Level combination, and Decision-Level combination, as shown in **Figure 2-2**.

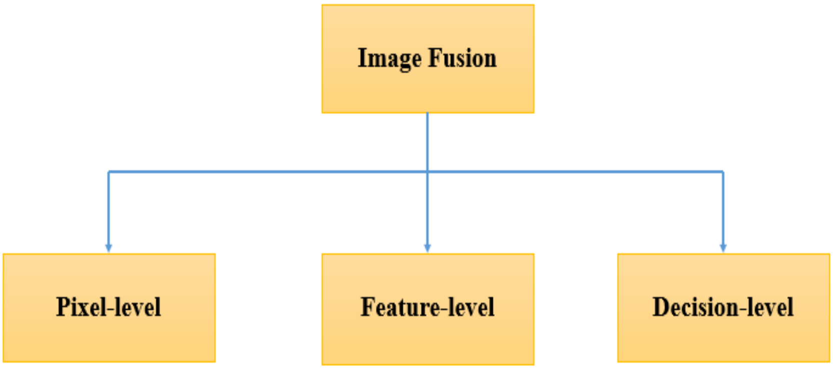

Figure 2-2 Categorization of image fusion.

2.2.1.1. Pixel-level

Pixel-level is the lowest level of the image fusion process. It deals directly with the pixels. The advantages of this level are to detect unwanted noise, to provide detail information, less complexity, and ease of implementation. However, these methods do not handle mis-registration and can cause blocking artefact [6]. This method can be mathematically expressed as follows:

$$f(x,y)=\frac{1}{N}\sum_{i=0}^{N} I_i(x,y) \quad (2\text{-}1)$$

Where $f(x,y)$ denotes a fused image, $I_i(x,y)$ represent the source images, $i=1, 2, \ldots\ldots N$. This method is simple, easily to implement, and low cost computationally, by using this method all information content within images are treated the same. However the result of this method is unsatisfactory because this method introduces artifacts, causes pattern cancellation and contrast reduction [7]. In mid-eighties, Burt and Adelson introduced a novel method of image fusion based on hierarchical image decomposition, namely Laplacian pyramid.

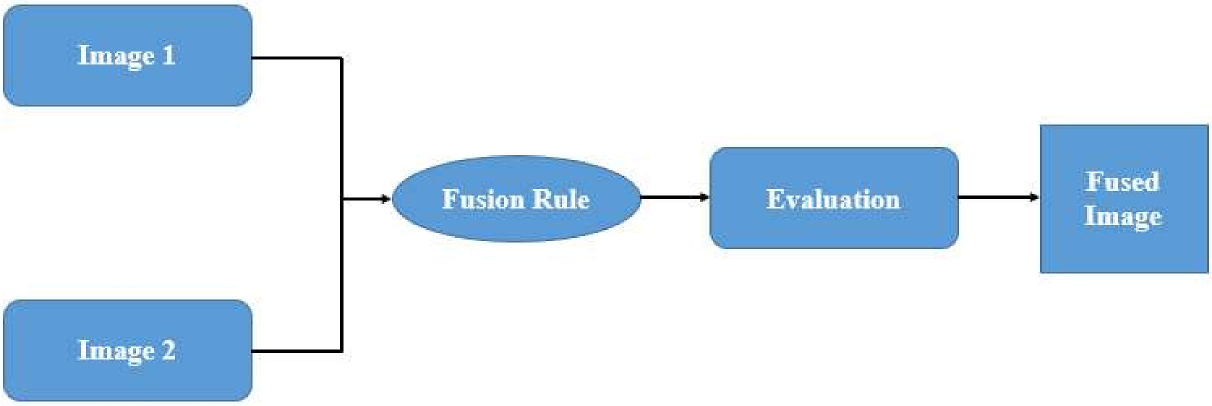

Figure 2-3 Pixel-level of image fusion.

2.2.1.2. Feature-level

In feature level process, features are extracted from input images. Image is segmented in continuous regions and fuse them using fusion rule. Features of images are combined such as size, shape, contrast, pixel intensities, edge and texture [8]. At this level, their calculations ordinarily fragment the image under contiguous regions and blend the regions together using their properties. These characteristics used may a got chance to be determined starting with every image alternately they may a get chance to be obtained by the simultaneous preparing of the significant amount from the input images.

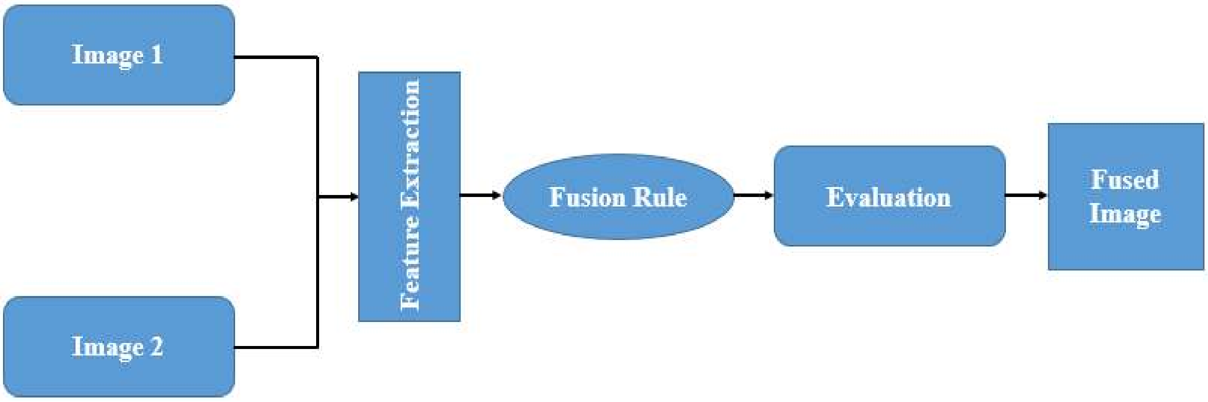

Figure 2-4 Feature-level of image fusion.

2.2.1.3. Decision-level

The decision level integrates the findings of numerous algorithms to produce a final fused judgment by integrating information at a higher level of abstraction [8].

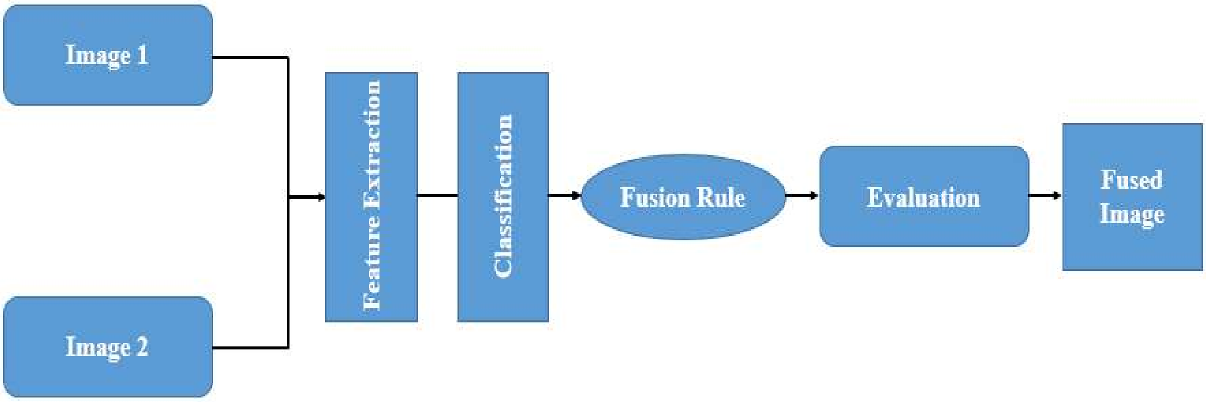

Figure 2-5 Decision-level of image fusion.

In the previous three cases, in order to extract information, the source images are processed individually, each one separately. Through the information obtained, decision rules are applied to them to reinforce the common interpretation. In general, fusion methods can also be categorized based on domain and on the input data and the purpose.

Image fusion methods can be divided into two categories based on their domains [9]:

- In spatial field techniques, the image pixels are directly dealt with to process their values and achieve the desired result. These techniques include Averaging, select maximum/minimum method, Bovey transforms, Intensity hue saturation method (IHS), High pass filtering method (HPF) and Principal component analysis method (PCA). The spatial domain has the disadvantage of spatial distortion in the new fused image that which is optimized in the frequency domain

- In the frequency domain, to get a fused image the image must be transformed into the frequency domain and the frequency coefficients are also combined. Some of the transform domain fusion techniques include discrete stationary wavelet transform and wavelet transform

Image fusion methods can also be classified based on the input data and the purpose [10] [11]:

- Multi-view fusion
  Multi-view fusion is defined as the combination of images captured by a sensor from different viewing points at the same time. This type of fusion provides high-resolution images.
- Multi-temporal fusion
  Here images taken at different time slots are combined in order to detect changes between them or to produce accurate images of objects.
- Multi-focus fusion
  In multi-focus fusion, images of different focal lengths from various imaging equipment are combined into a single image of better quality.
- Multi-modal fusion
  Multi-modal fusion Indicates that the target images are from different sensors. This fusion is used in applications like medical diagnosis, security, surveillance, etc.

2.2.2. Multi focus image fusion methods

Due to the rapid development witnessed in the field of image fusion in recent years, new methods have emerged after they were limited to the method of spatial domain and transform domain. The emergence of multi-focus image fusion resulted in the suggestion of other methods of image fusion that fall within the field of transform domain and spatial domain in the literature [6]. On the other hand, the study based on deep learning emerged as a very important process in multi-focus image fusion.

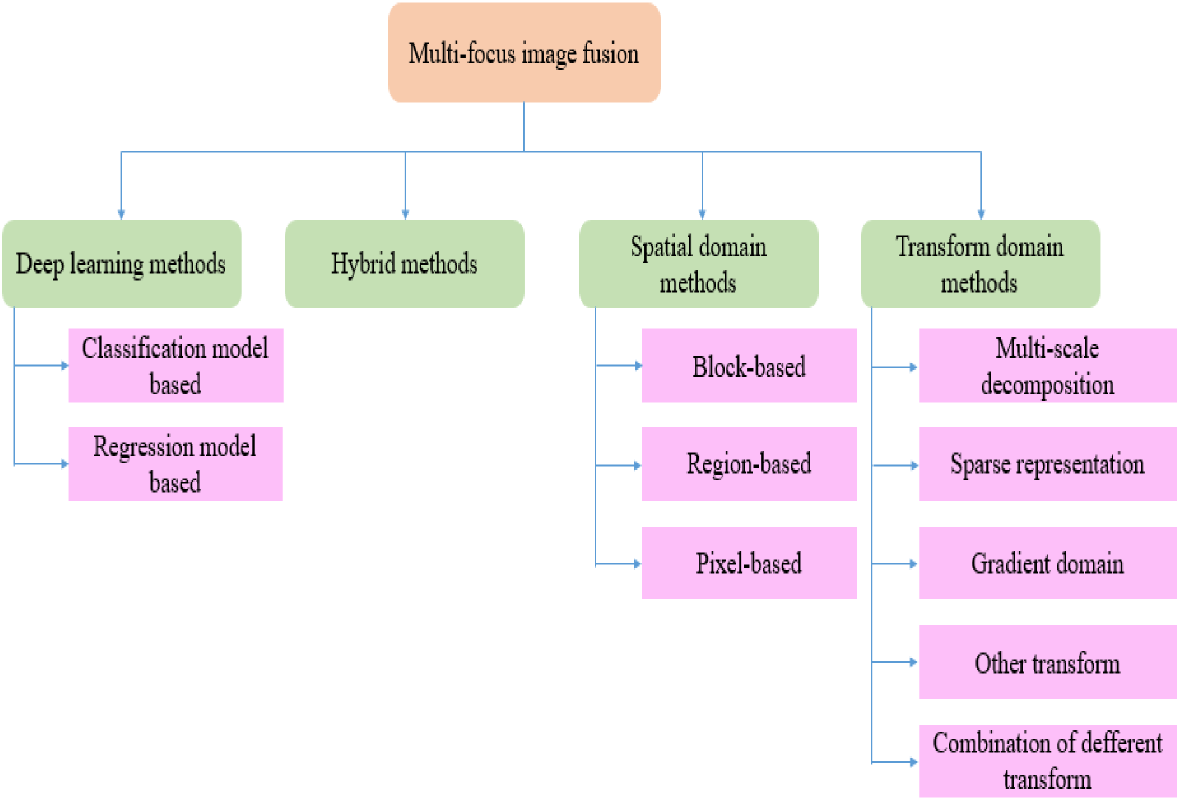

Figure 2-6 A new taxonomy for image fusion.

2.2.2.1. Transform domain methods

As the name suggests, in the spatial domain methods the source image is fused in the spatial domain, i.e, using some spatial features of the images [12]. This approach consists of five methods which are presented as follows

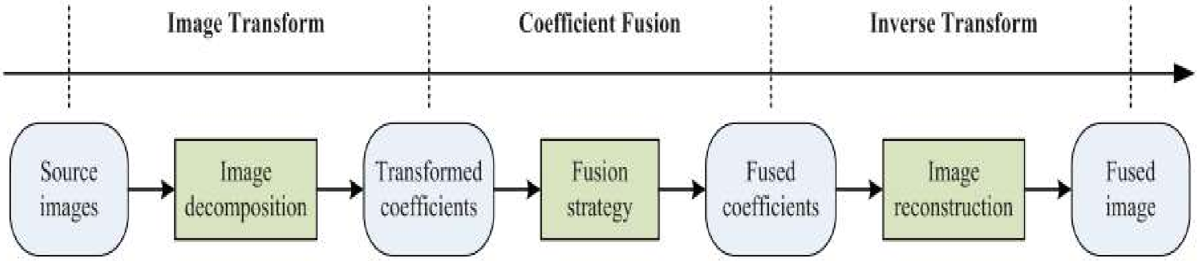

Figure 2-7 A schematic diagram of transform domain methods in general.

- **Multi-scale decomposition**

Coinciding with the emergence of multi-resolution analysis theories such as image pyramids and wavelets, the study of multi-focus image fusion can be traced back to the 1980s and 1990s [12]. After the emergence of these theories, studies based on multi-scale decomposition flourished in the field of multi-focus image fusion.

- **Sparse reprsentation (SR)**

In the past decade, SR-based methods have rapidly spread as an influential branch in the field of multi-focus images image fusion. SR is said to be in line with the physiological characteristics of the human visual system since it represents the natural sparsity of signals [12]. The sliding window approach is used to partition each source image into a number of overlapping patches, and the orthogonal matching pursuit (OMP) algorithm is used to conduct sparse decomposition on each patch independently. The fundamental premise of SR is that a signal can be approximated by a linear combination of a "few" atoms from a redundant dictionary.

- **Gradient domain (GD)**

The main idea behind the GD-based image fusion method is to fuse source image gradient representations and then reconstruct the fused image by constraining its gradient to the fused gradient [13]. A fused gradient field approach has been proposed in Piella, this approach pertains to images based on the structure tensor. The gradient maps of each source picture are used to compute the structural tensor (a 2 by 2 matrix with each element being a gradient map) is calculated based on the gradient maps of each source image.

The basic idea of GD-based image fusion method is to fuse the gradient representations of source images and then reconstruct the fused image by restricting its gradient to the fused gradient. In Piella proposed a variational approach for image fused gradient domain based on structure tensor. The source images are stacked into a multi-valued image and its structure tensor (a 2 by 2 matrix while each element is a gradient map) is calculated based on the gradient maps of each source image. As a result, the structure tensor contains the combined gradient information of all the source images, and the target gradient can be represented by the eigenvalues and eigenvectors of the structure tensor.

- **Methods based on other transforms**

In addition to the above image transform approaches, some other transforms like independent component analysis (ICA), higher order singular value decomposition (HOSVD), Discrete cosine transform (DCT) compressed sensing (CS) and cartoon-texture decomposition (CTD) have also been successfully applied in multi-focus image fusion. Each source image is divided into a number of patches using the sliding window technique, and each patch is split into the ICA domain. After fusing the transform coefficients, the fused patches are recreated. Finally, the overlapping picture patches are averaged to reconstitute the fused image. It should be noted that the sliding window based fusion scheme described in has a substantial impact on the above-mentioned study of SR-based picture fusion.

- **Methods based on the combination of different transforms**

Transforms are different according to the characteristics that distinguish them. Some multi-focus image fusion methods are suggested that combine multiple transforms to integrate their respective advantages. From there, Li and Yang proposed a hybrid multi-scale technique that combines the curvelet domain to capture more edge information with the wavelet transform to fuse the curvelet coefficients and extract additional small details [14].The SR-based fusion scheme was adopted to provide a new advantage in the fused images sourced from the advantages of other approaches on the one hand and to overcome the disadvantages of each one on the other.

2.2.2.2. Spatial domain methods

- **Block-based methods**

In 2001, Li et al. first introduced a spatial domain multi-focus image fusion method based on a block division scheme, in which each source image is divided into a number of blocks with fixed size. The spatial frequency is employed as activity level measurement of each block and a threshold based adaptive fusion rule is used to obtain the fused block. The fused image is finally constructed after applying a major filtering based consistency verification approach. Since then, block-based methods have emerged as an active direction in multi-focus image fusion and a variety of improvements have been made on activity level measurement, fusion rule, block division strategy, etc.

- **Region-based methods**

To further increase the flexibility of partition for source images, researchers have developed region-based spatial domain fusion methods with image segmentation technique. The framework of region-based methods is similar to that of block-based methods, while the main difference is that the activity level measure is conducted in each segmented region with irregular size rather than the block. Li et al. first introduced a region-based multi-focus image fusion method with a PCNN-based segmentation approach.

- **Pixel-based methods**

In recent years, pixel-based spatial domain methods have become the most popular direction in multi-focus image fusion, owing to their advantage on obtaining precise pixel-wise weigh map for fusion. Most pixel-based methods are designed under the linear weighted sum frame work, namely, the fused image is calculated as the linear weighted sum frame work, namely, the fused image is calculated as the weighted sum of all the source images and the core issue is to obtain the weight map for each source image. In these methods, an activity level measurement, which is also known as focus measure in multi-focus image fusion, is first applied to evaluate the saliency of pixels in source images.

2.2.2.3. Hybrid methods

The spatial domain and transform domain techniques each have their own set of benefits and drawbacks. The advantages of spatial and transform domain approaches are integrated in hybrid based methods to produce more efficient IF methods that can cope with the challenges that classic methods can't. Because deep learning is quickly becoming one of the most popular branches, certain transform or spatial domain approaches have been used with deep learning to improve fusion outcomes.

2.2.2.4. Deep learning methods

Deep learning based methods are classifed as classifcation-based methods and regression based methods. Some of the neural network-based methods mentioned in literature are discussed below:

- **Classification model based methods**

Li et al. created an Multi-Focus Image Fusion (MFIF) approach based on artificial neural networks in 2002 [15]. This method performed better than the DWT method. It was easy in terms of calculation and could be implemented in real-time applications. Even if the source photos were misregistered or the object moved, our approach was able to fuse them together. The main drawback of this system was determining the appropriate block size. Choosing a smaller block size resulted in a saw-tooth effect, whilst choosing a bigger block size resulted in less distinct images because each block may contain two or more objects.

- **Regression model based methods**

Qin et al. looked at a deep learning-based MFIF approach that uses a fully convolutional two-stream learning scheme [16]. Convolutional, fusion, and deconvolutional filters are used to complete this approach. This strategy performs better subjectively and objectively when compared to other spatial and transfer domain methods. Zhao et al. also presented MFIF method based on Multi-Level Deeply Supervised Convolutional Neural Networke [17]. Simultaneous output supervision was used during testing to improve performance. This approach was capable of capturing both low- and high-frequency material, allowing two or more images to be fused.

2.2.3. Approaches of image fusion

In data fusion there are two approaches, image fusion at level of pixel (High-level approach) and feature-level image fusion (Low-level approach).

2.2.3.1. High Level Approach

Fusion is attempted on objects with characteristics, derived from processing of conventional images. These features may be more or less secure, so incorporate. Imprecision as uncertainty [18].

2.2.3.2. Level Approach

Pixel-level fusion is the combination of raw data from multiple images source in a single image. In pixel-level fusion, the fused pixel is derived from a set of pixels in the different inputs. The main advantage of fusion at the pixel is that the original measured quantities are directly involved in the process of fusion [18].

2.3. Image registration

Image registration is defined as the result of the superposition of two or more images of the same subject. This subject was captured at different times, from different points of view or with different sensors [19].

2.3.1. Image Registration Model and Framework

Generally, the image registration process is described as aligning two or more images and combining them to the best similarity criterion. This process is an essential pillar in many applications of image analysis in general and medical imaging in particular [20]. Image registration is based on three components: a transformation which relates the target (sensed or moving) image I_s and source (reference or fixed) image I_r , a similarity measure S which measures the similarity between target and source image, and an optimization algorithm which determines the optimal transformation parameters as a function of the similarity measure [21]. **Figure 2-8** presents the steps required in the image registration process.

In the image registration process, the sensed image undergoes a series of transformations to correspond the reference image depending on a similarity metric. The process of changing the parameters of the transformation continues until the two images are optimal similar. The optimal transformation parameters T of the two images undergoing the registration process can be obtained by maximizing the similarity metric S, the following equation illustrates this process [22]:

$$\hat{T} = \arg\max_{T} S\left[I_r(x,y), I_s(T(x,y))\right] \tag{2-2}$$

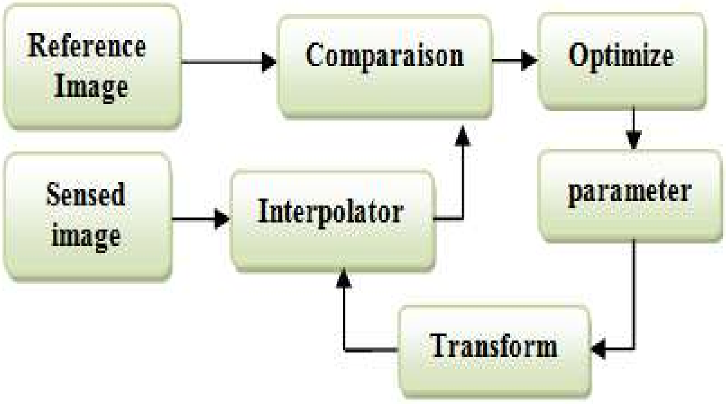

Figure 2-8 Block diagram of image registration process.

2.3.1.1. Transformation

Transformation in image registration is defined as a transformation function that aims to mode a geometric relationship between two or more images. This Transformation function can also cause distortions between the two input images. There are three categories of distortions namely, no distortion, global distortion and local distortion. The ratio of the different distortions between two images mainly relates to the transformation functions, as shown in the following:

- In the first case, a rigid transformation function can be used, such as the conformal transformation function, if there is no distortion, but is only rotation and translation difference between two images.
- In the second case, much transformation functions can be used, such as affine, projective and polynomial transformations for global distortion. The selection of suitable transformation to overcome this distortion depends on the complexity of the image distortions.
- In the third case, the presence of a local distortion necessarily is required a more complex transformation function, such as the polynomial, elastic and radial polynomial functions [23].

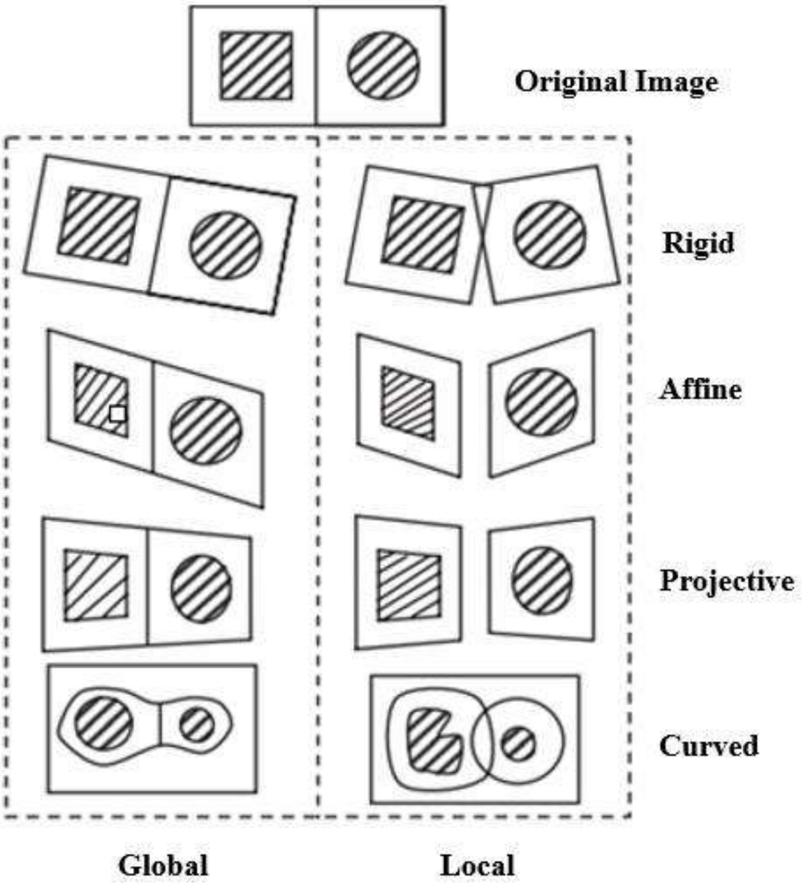

Figure 2-9 Various transformation cases related to registration.

The transformation function's parameters should be estimated using a sufficient number of correspondences once the transformation has been established. The solution of the transformation function is reached using a least square approximation [24]. The examples of various transformations are shown in **Figure 2-9**. A local transformation is used for the entire image, while a global transformation is used for each sub-image [24]. It appears from the aforementioned figure that the same transformation yields entirely different outcomes when applied to global distortion and local distortion.

- **Rigid transformation function**

Rigid transformation in the image registration process depends only on image translation and rotation as shown in the following equation.

$$\begin{pmatrix} X_2 \\ Y_2 \end{pmatrix} = \begin{pmatrix} t_X \\ t_Y \end{pmatrix} + \begin{pmatrix} \cos\theta & -\sin\theta \\ \sin\theta & \cos\theta \end{pmatrix} \begin{pmatrix} X_1 \\ Y_1 \end{pmatrix} \tag{2-3}$$

Where θ indicates image rotation angle, while t_X and t_Y are translations in X and Y directions, respectively,

- **Non-rigid transformation function**

This type of transformation is characterized by large and complex image distortions. There are four categories of this transformation.

Conformal transformation:

$$\begin{pmatrix} X_2 \\ Y_2 \end{pmatrix} = \begin{pmatrix} t_X \\ t_Y \end{pmatrix} + s \begin{pmatrix} \cos\theta & -\sin\theta \\ \sin\theta & \cos\theta \end{pmatrix} \begin{pmatrix} X_1 \\ Y_1 \end{pmatrix} \tag{2-4}$$

Here s is the scale factor.

Affine transformation:

$$\begin{pmatrix} X_2 \\ Y_2 \end{pmatrix} = \begin{pmatrix} t_X \\ t_Y \end{pmatrix} + s \begin{pmatrix} a & b \\ c & d \end{pmatrix} \begin{pmatrix} X_1 \\ Y_1 \end{pmatrix} \tag{2-5}$$

Projective transformation, from 2-D to 2-D:

$$X_2 = \frac{a_{11}x_1 + a_{12}y_1 + a_{13}}{a_{31}x_1 + a_{32}y_1 + a_{33}} \tag{2-6}$$

$$Y_2 = \frac{a_{21}x_1 + a_{22}y_1 + a_{23}}{a_{31}x_1 + a_{32}y_1 + a_{33}} \tag{2-7}$$

Polynomial transformation:

$$X_2 = f(x_1, y_1) \tag{2-8}$$

$$Y_2 = g(x_1, y_1) \tag{2-9}$$

2.3.1.2. Similarity measure

Mutual information of image intensities is a new matching criterion that features robust and completely automatic registration of multi-modal images without prior segmentation [25]. These advantages make the proposed mutual information method suitable for many different applications involving CT images. For two images A and B of individual entropy and joint entropy, the Mutual information between these two images can be calculated as follows:

$$MI(A,B) = H(A) + H(B) - H(A,B) \tag{2-10}$$

Where:

$$H(A) = -\sum_{a} P_A(a) \log_2 P_A(a), \tag{2-11}$$

$$H(A,B) = -\sum_{a,b} P_{A,B}(a,b) \log_2 P_{A,B}(a,b), \tag{2-12}$$

Where $P_A(a)$ and $P_{A,B}(a,b)$ are the marginal distributions of probability that can be viewed as a combined PDF projection onto the axes corresponding to the intensities in images A and B, respectively [26].

2.3.1.3. Optimizer

The optimization is an essential component and very important step in the image registration process. The role of optimization is to search the geometric transformation that is applied to the scene to make it as similar as possible to the model, in other words [27], find the optimum transformation parameters required for aligning the images. There are several optimization methods that differ according to the algorithms used.

2.3.2. Image Registration Techniques

The alignment of the matching features in some detected images with regard to a reference is the registration process's ultimate goal, as was already mentioned. The fusion process cannot be accomplished without such a procedure. Its significance stems from the fact that fusion or fusing of the images is based on the related features of these images. Several methods have been introduced to perform the image registration process. Depending on the number of criteria, these methods can be classified to seven methods: Dimensionality based method, Registration basis, Nature of the transformation, Transformation domain, Interaction, Modalities, Subject [28].

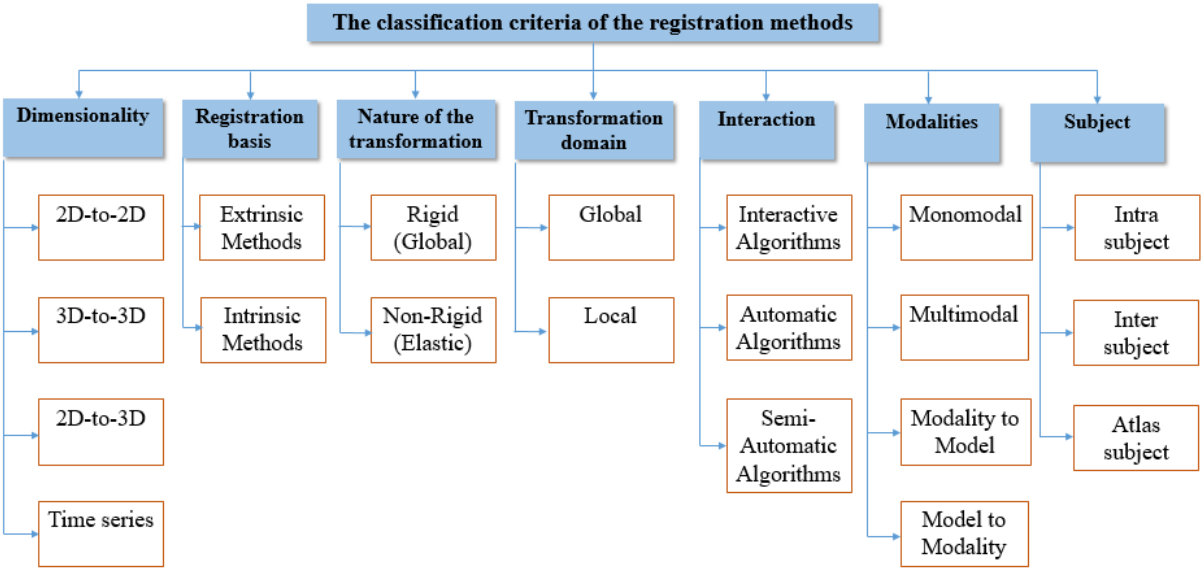

Figure 2-10 The classification of the registration methods.

2.3.2.1. Dimensionality

The dimensionality criterion is divided into two classes: spatial and time-series dimensions [29]. In spatial dimensions, image dimensions refer to the number of geometric dimensions of an image space. During the registration process based on this classification, the required transformation is calculated either by image coordinate systems or physical space and the input image, i.e. this process can be done based on a set of corresponding point pairs or a set of corresponding surface pairs [30].

The dimensionality criterion can be 2D-to-2D, 3D-to-3D, 2D-to-3D or time series. 2D-to-2D images can simply be registered by rotation and two orthogonal translations [29]. In addition, differences in measurement may need to be corrected from the real object for each image. 3D-to-3D registration is used to align tomography datasets or a single tomography image of any spatially defined information. 2D-to-3D registration is used when it is established a correspondence between 3D volumes and projection images, such as X-ray images or optical images. In registration based on time series, the aligning of images are treated in the same or different modalities over different time instances.

2.3.2.2. Registration basis

Depending on the nature of the registration basis, the methods within this group can be classified into Intrinsic and Extrinsic methods [31]. The extrinsic registration is easy and simple to automate, and it does not require complex optimization algorithms because of the easily calculated conversion parameters. The importance of the Intrinsic registration method is demonstrated by providing information about the patient in the medical field, such as apparent prominent landmarks, binary divided structures, or voxel image intensities [30][32].

2.3.2.3. Nature of the transformation

All mapping techniques can be divided into one of two main categories: rigid (global) transformations and non-rigid (elastic/local) transformations. In registration based on rigid transformation, the 2D or 3D images are completely transformed, for example translating, rotating, scaling and/or sharing every depicted object in the same way that in turn preserves distances, lines and angles [33]. This transformation can be translated mathematically as in Equation 2-13. Non-rigid or non-affine methods, as mentioned earlier, it is a method that uses higher order transformations that map lines onto curves [33].

$$\begin{pmatrix} x' \\ y' \\ 1 \end{pmatrix} = \begin{pmatrix} w_{11} & w_{12} & 0 \\ w_{21} & w_{22} & 0 \\ 0 & 0 & 1 \end{pmatrix} \begin{pmatrix} x \\ y \\ 1 \end{pmatrix} \tag{2-13}$$

2.3.2.4. Transformation domain

The coordinate transformation of the images may be global or local. In the global case, mapping parameters that are valid for the entire image are used to accomplish the transformation [28]. While the local case, only a tiny patch of the image surrounding the position of the chosen control point is altered in the local case.

2.3.2.5. Interaction

The Registration using the interaction method is three levels based on the relation between the user and the registration process[29]. First, interactive algorithms in which the user relies on specific programs that provide them with an estimate of the initial conversion parameters to accomplish the registration process [30]. Secondly, unlike interactive algorithms, automatic algorithms work without any interaction at all. Finally, in the semi-automated algorithms, the user relies on dividing the data or directing the algorithm to the desired solution for preparation to the registration process [29].

2.3.2.6. Modalities

Based on the different types of modalities applied to the registration there are four types of registration: mono-modal, multi-modal, modality-to-model and model-to-modality [34]. In multi-modal registration, the images participating in the registration process belong to different modalities, while in mono-modal registration, the process takes place between images of the same medical modality [35]. For a modality-to-model and model-to-modality registration, only one image is included while the model or even patient represents the other registration input.

2.3.2.7. Subject

The subject is an important criterion that provides another division of image registration methods. Subject-based methods can be grouped into intra, inter and, atlas subject registration. Such division is based on whether the involved images belong to the same patient, to different patients, or one of the images belongs to the patient and the other obtained from an information database [28]. Methods of this category are widely used in the process of diagnosing diseases and performing surgeries for providing great clinical information through accurate alignment of images collected from the same subject using the same modality at a different time [36].

The registration based in intra subject is used in the process of diagnosing diseases and performing surgeries for providing great clinical information through accurate alignment of images collected from the same subject using the same modality at a different time [36]. Inter-subject based registration method is usually used in determining the shape and size changes in addition to the grosser topology changes. In this type of registration, the images involved in the registration process belong to different patients. Finally atlas-based registration methods: this class of registration shows help in obtaining statistics about the size and the shape of a particular structure by gathering the input images from a single patient while the other is constructed through a database of image information acquired via many subjects imaging [28].

2.4. Evalution metrics

2.4.1.1. Structural similarity-based metric

Yang et al. [37] Proposed the $\mathrm{Q_Y}$ similarity measure that relies mainly on highly adaptive structural information on the human visual system. This measure is based on SSIM on calculating the similarity ratio between images, as shown by the following equation:

$$\mathrm{Q_Y} = \begin{cases} \lambda(\mathrm{w}) SSIM\ (\mathrm{A},\mathrm{F} \setminus \mathrm{w}) + (1-\lambda(\mathrm{w})) SSIM\ (\mathrm{B},\mathrm{F} \setminus \mathrm{w}), \\ \quad SSIM\ (A,B \setminus w) \geq 0.75 \\ \max(\mathrm{SSIM}(\mathrm{A},\mathrm{F} \setminus \mathrm{w}), \mathrm{SSIM}(\mathrm{B},\mathrm{F} \setminus \mathrm{w})), \\ \quad SSIM\ (A,B \setminus w) < 0.75 \end{cases} \tag{2-14}$$

Where:

$$\lambda(w) = \frac{s(A \setminus w)}{s(A \setminus w) + s(B \setminus w)} \tag{2-15}$$

Here w represent a window of size, $\lambda(w)$ is a local weight while $s(A \setminus w)$ and $s(B \setminus w)$ are the variance of source images A and E in window w, respectively. SSIM (.A, F\iw) and SSIM (.A, F\iw) represents the SSIM map calculated by a sliding win-dow manner between A and F. For two source images X and Y, the definition of the structural similarity metric SSIM measure proposed by Wang et al. [37] is given as follows :

$$\mathrm{SSIM} = (X,\ Y) = \frac{(2\mu_X\mu_Y + C_1)(2\sigma_X\sigma_Y + C_2)}{(\mu_X^2 + \mu_Y^2 + C_1)(\sigma_X^2 + \sigma_Y^2 + C_2)} \tag{2-16}$$

2.4.1.2. Human perception-based metric

By the model of the human visual system, Chen and Blum [20] suggested a human perception-based metric Q_{CB}, which compares the features in the source image with those of the registered image. The measurement can be given as follows:

The first step is to calculate the Q_{GQM} Global Quality Map by:

$$Q_{GQM} = \lambda_A\left(Q_{AF}(i,j)\right) + \lambda_B\left(Q_{BF}(i,j)\right) \tag{2-17}$$

Where $Q_{AR}(i,j)$ and $Q_{BR}(i,j)$ represent the contrast in formation that was transferred from the source images A and B to the registered image R, respectively. λ_A and λ_B denote the saliency maps of Q_{AF} and Q_{BF} respectively. Q_{CB} can be calculated based on Q_{GQM} as shown in equation 2-18:

$$Q_{CB} = \overline{Q_{GQM}} \tag{2-18}$$

A higher Q_{CB} value indicates that the registered image will retain more contrast information from the source images.

2.4.1.3. Edge-based metric

The Q_G scale evaluates the amount of edge information transmitted from the source images to the fused image**.** This scale-based on image features was proposed by Xydeas and Petrovic [21], which can be defined as follows:

$$Q_G = \frac{\sum_{i=1}^{m}\sum_{j=1}^{n}\left(Q^{AF}(i,j)W^{A}(i,j)+Q^{BF}(i,j)W^{B}(i,j)\right)}{\sum_{i=1}^{m}\sum_{j=1}^{n}(W^{A}(i,j)+W^{B}(i,j))} \tag{2-19}$$

Where:

$$Q^{AF} = Q_g^{AF}(i,\ j)Q_0^{AF}(i,j) \tag{2-20}$$

Here denote edge strength $Q_g^{AF}(i,j)$ and $Q_0^{AF}(i,j)$ orientation preservation values specific at pixels (i, j), respectively. Whil $W^{A}(i,j)$ represent the weight coefficient for each edge that shows the importance of that edge. Same definition for $Q^{BF}(i,j)$ and $W^{B}(i,j)$**.** m and n are the size of source image. The value of Q_G is directly proportional to the amount of information transferred, as the higher the value of Q_G, the greater the amount of edge information transferred from the source image to the fused image.

2.4.1.4. Phase congruency-based metric Q_P

This measure was proposed by Zhao et al. [38] based on image match, this match provides an absolute measure of an image feature to determine an evaluation metric. Q_p consists of three basic correlation coefficients to measure the amount of edge and angle information transferred from the source images to the merged image [38]**.** Through these parameters, this scale can be defined as follows:

$$Q_P = \left(P_p\right)^{\alpha}\left(P_M\right)^{\beta}\left(P_M\right)^{\gamma} \tag{2-21}$$

Where p, m and n denote the phase congruency, maximum and mini-mum moments, respectively.

2.4.1.5. Fusion information score

Generally, fusion information score is a measure of fusion performance based on gradation. The degree of fusion information score for the two source images A and B are represented as $Q^{AB/F}$. This metric evaluates the performance of the fusion method based on the amount of edge information transfer from the two source images to the fused image [39]. This scale is satisfies for $Q^{AB/F}$ between 0 and 1. $Q^{AB/F} = 0$ indicate that all source information has been lost, while $Q^{AB/F} = 1$ indicates that all source information are transfed without any loss “ideal fusion“. The general formula for $Q^{AB/F}$ can be given as follows:

$$Q^{AB/F} = \frac{\sum_{n=1}^{N}\sum_{m=1}^{M}\left(Q^{AF}(n,\ m)w^{A}(n,\ m) + Q^{BF}(n,\ m)w^{B}(n,\ m)\right)}{\sum_{i=1}^{N}\sum_{j=1}^{M}(w^{A}(i,\ j) + w^{B}(i,\ j))} \quad (2\text{-}22)$$

Where $Q^{AF}(n,\ m)$ and $Q^{BF}(n,\ m)$ represent measures of edge preservation between the source images (image A and image B) and the fused image. $w^{A}(n,\ m)$ and $w^{B}(n,\ m)$ are the edge preservation values, they relate to the strength of the edges of the image.

2.4.1.6. Fusion Noise $N^{AB/F}$

Fusion artifacts can be defined as the visual information that appears in the fused image and there are no features in the source images. This is considered false information (Noise) and detracts from the quality of the fused image. The total fusion artifacts of the fusion process between the two source images A and B can be evaluated by visually weighted integration of the fusion, noise estimates over the entire fused image as shown in equation 2-23 [40] :

$$N^{AB/F} = \frac{\sum_{\forall\ n,m} N_{n,m}\left(w_{n,m}^{A} + w_{n,m}^{B}\right)}{\sum_{\forall n,m}\left(w_{n,m}^{A} + w_{n,m}^{B}\right)} \quad (2\text{-}23)$$

$$N^{AB/F}\begin{cases} 2 - Q_{n,m}^{AF} - Q_{n,m}^{BF}, \mathit{if}\ \ g_{n,m}^{F} > \left(g_{n,m}^{A}\ \&\ g_{n,m}^{F}\right) \\ \quad 0 \qquad\qquad\qquad\qquad , \mathit{otherwise} \end{cases} \quad (2\text{-}24)$$

Where $N_{n,m}$ indicate the local estimates of fusion artifacts or fusion noise**.**

2.4.1.7. Fusion loss $L^{AB/F}$

This metric represents a measure of the information lost during the image fusion process. The information lost appears in the input images but not in the fused image. A direct information loss can be defined as QAF and QBF values less than 1 but the correct assessment is by one's ability to distinguish it from fusion artifacts [40]. The following equation shows this metric:

$$L^{AB/F} = \frac{\sum_{\forall\ n,m} r_{n,m}\left[\left(1 - Q_{n,m}^{AF}\right)w_{n,m}^{A} + \left(1 - Q_{n,m}^{BF}\right)w_{n,m}^{B}\right]}{\sum_{\forall\ n,m} w_{n,m}^{A} + w_{n,m}^{B}} \quad (2\text{-}25)$$

Where:

$$r_{n,m} = \begin{cases} 1, if \ g^{F}_{n,m} < g^{A}_{n,m} \ or \ g^{F}_{n,m} < g^{B}_{n,m} \\ 0, \quad Otherwise \end{cases} \tag{2-26}$$

Here $r_{n,m}$ indict to the flag and its value is 1.

2.4.1.8. Average pixel intensity (ABI)

ABI or mean μ measures the contrast of the fused image as shown in the following equation:

$$\bar{F} = \mu = \sqrt{\frac{\sum_{m=1}^{p}\sum_{n=1}^{q} f(m,\ n)}{pq}} \tag{2-27}$$

2.4.1.9. Entropy (E)

Entropy can be defined as the process of measuring the amount of information included in the image. The values of this metric range from 0 to 8 [41].

$$E_n = -\sum_{i=0}^{n} p(a_i)\log(a_i) \tag{2-28}$$

Where a_i indicates the ith point is its gray-scale values and the probability.

2.4.1.10. Standard deviation (SD or σ)

Standard deviation indicates a spread in the data or the variation of the current pixel intensity value with respect to the average pixel intensity value in the fused image [39].

$$SD = \sqrt{\frac{\sum_{m=1}^{p}\sum_{n=1}^{q} (f(m,\ n) - \bar{F})}{pq}} \tag{2-29}$$

Where $f\ (m,n)$ is the input image of size $q \times p$ and $\bar{F}$ indicates Mean or average pixel intensity (μ).

2.4.1.11. Fusion Symmetry (FS)

FS metric [42] how much indicate symmetric the fused image is, with respect to the input images.

$$FS = abs\left(\frac{I_{AF}}{I_{AF} + I_{BF}} - 0.5 \right) \tag{2-30}$$

The lower the FS value, the better the performance of the method.

2.4.1.12. Correlation Coefficient (CC)

CC metric is used to compute the spectral feature similarity between the reference and the fused image. The value of this metric should be high i.e. close to 1 for better performance [3].

$$CC = \frac{\sum_{i,j}\left[\left(X_{i,j} - \bar{x}\right).\left(\hat{X}_{i,j} - \bar{\hat{x}}\right)\right]}{\sqrt{\sum_{i,j}\left[\left(X_{i,j} - \bar{x}\right)^2\right].\sum_{i,j}\left[\left(\hat{X}_{i,j} - \bar{\hat{x}}\right)^2\right]}} \tag{2-31}$$

2.4.1.13. Normalized Mutual Information (NMI)

The metric NMI is robust to change overlapping tissue regions, as it relies on a Parzen-window approach to estimate the probability density function [43]. For images A and B, the NMI is given as follows:

$$NMI(A,B) = \frac{H(A) + H(B)}{H(A,B)} \tag{2-32}$$

2.4.1.14. SImilarity Metric (SSIM)

SSIM basically compares the standard image and the image to be detected from three aspects: Brightness, Contrast, and Structure Similarity [44].

$$SSIM\left(I_g, I_{s\_reg}\right) = \frac{\left(2\mu_g\mu_{s\_reg} + \left(k_1L\right)^2\right)\left(2\sigma_{gs\_reg} + \left(k_2L\right)^2\right)}{\left(\mu_g^2 + \mu_{s\_reg}^2 + \left(k_1L\right)^2\right)\left(\sigma_g^2 + \sigma_{s\_reg}^2 + \left(k_2L\right)^2\right)} \tag{2-33}$$

Where μ_g, μ_{s_reg}, σ_g, and σ_{s_reg} are the local means, standard deviations, and cross-covariance for images I_g, I_{s_reg}. k_1, k_2 are parameters with small values and L is the maximum pixel value.

2.4.1.15. Dice Similarity Coefficient

The Dice Similarity Coefficient (DSC) is defined as an instrument of determining a similarity measure between images A and B, and it can be given as follows [45]:

$$DSC = (A,B) = \frac{2|A \cap B|}{|A| \cap |B|} \tag{2-34}$$

2.4.1.16. Mean squared error (MSE)

To assess the performance of the two methods, SCA and ISCA the SSIM, the mean squared error (MSE) and absolute error (AE) between true $T^{*}=\left(t_{x}^{*},\ t_{y}^{*},\ \theta^{*}\right)$ and estimated $T=\left(t_{x},\ t_{y,}\ \ \theta\right)$ transformation. They are defined as:

$$MSE=\frac{1}{MN}\sum_{i=1}^{M}\sum_{j=1}^{N}\left(I_{r}\left(i,\ j\right)-I_{m_{reg}}\left(i,j\right)\right)^{2} \tag{2-35}$$

$I_{r}\left(i,j\right)$ and $I_{m\_reg}\left(i,j\right)$ are the pixel values of the ground truth and registered images, $M\times N$ is the size of images.

2.5. Advantages and disadvantages of image fusion

2.5.1. Advantages

- It is easiest to interpret.
- Fused image is true in color.
- It is best for identification and recognition.
- It is low in cost.
- It has a high resolution used at multiscale images.
- Through image fusion there is improved fused images in fog.
- Image fusion maintains ability to read out signs in all fields.
- Image fusion has so many contrast advantages basically it should enhance the image. with all the perspectives of image.
- It increases the situational or conditional awareness.
- Image fusion reduced the data storage and data transmission.

2.5.2. DisAdvantages

- Images have less capability in adverse weather conditions it is commonly occurred when image fusion is done by single sensor fusion technique.
- Not easily visible at night it is mainly due to camera aspects whether it is in day or night.
- More source energy is necessary for the good visualization of mages based on spatial frequency.
- Due to rain or fog visualization is not cleared if one click the two source images in this type of weather conditions it will give the worst output.

- In this process there is huge chances of data loss.
- It needs the proper maintenance.
- Processing of data is very slow when images are fused.

2.6. Conclusion

Image registration and fusion is a widely used technique because it provides complementary information useful in the analysis process. These two techniques have very important stages for successfully applying this technique. The application of image registration and fusion Technique also depends on the existence of an effective method that reduces defects resulting from the weakness of other methods. This chapter we mainly dedicated to the background of our work, which was divided into two main sections, the first section is devoted to image registration, while the second is devoted to image fusion. In this chapter, we have presented the concept of image registration and fusion and their most important steps, in addition to the classifications and evaluation metrics. Finally, the main advantages and disadvantages were discussed.

3.1. Introduction

Optimization can be defined as the process of finding the optimal solution. This process is considered a branch of applied mathematics and numerical analysis. There are some simple problems that can be solved by relying on traditional simple analysis methods based on mathematical analysis, while most problems are difficult to solve using methods based on analysis. Because we know that nature is an integrated system that provides solutions to most natural problems, relying on nature to provide solutions to difficult problems is the right decision.

In the period between 1940-1980 Meta-heuristic science emerged from the system of nature and has been widely used since the year 2000 until now [4]. A meta-heuristic is formally defined as an iterative generation process which guides a subordinate heuristic by combining intelligently different concepts for exploring (global search) and exploiting (local search) the search space; learning strategies are used to structure information in order to find efficiently near-optimal solutions.

In the remainder of this chapter, we provide an overview of optimization methods and a classification of these methods. Then we turn to the meta-heuristic optimization algorithms, Classification of meta-heuristic algorithms, and meta-heuristic algorithm for image registration. Finally, applications of meta-heuristics algorithms.

3.2. Optimization methods

The origins of optimization methods may be traced back to the days of Newton, Bernoulli, Lagrange, Cauchy, and Gibbs, when the calculus of variations was used to establish mathematical analysis. Such optimization approaches are commonly referred to as mathematical programming, and they have spawned a large body of advanced literature over the years. The demand for optimizing more sophisticated and intrinsically nonlinear optimization problems arose with the introduction of computers, resulted in new advances in optimization theory.

From a general point of view, optimization is part of nature. Any decision we make to solve a problem can be considered an attempt to address an optimal or near-optimal situation. Thus, any problem related to improvement can be considered a decision-making problem, and the question in this case is whether there is a better solution to this problem than the one we found or not. In other words, optimization entails finding the best solution feasible to improve the performance of the system in question. Optimization, as described by Beightler et al. [46], is a three-step decision-making process: (1) modeling the problem based on the knowledge of the problem, (2) finding measures of effectiveness or the objective function, and (3) the optimization method or optimization theory.

3.3. Classification of the optimization methods

According to the nature of the algorithm, optimization algorithms are divided into three categories: deterministic algorithms, stochastic algorithms, and hybrid algorithms, which combine deterministic and stochastic algorithms. According to the nature of the algorithm, the optimization algorithms can be categorized into three categories: deterministic algorithms, stochastic algorithms and hybrid algorithms which is a mixture of deterministic and stochastic algorithms. **Figure 3-1** illustrates the categories of this classification [47].

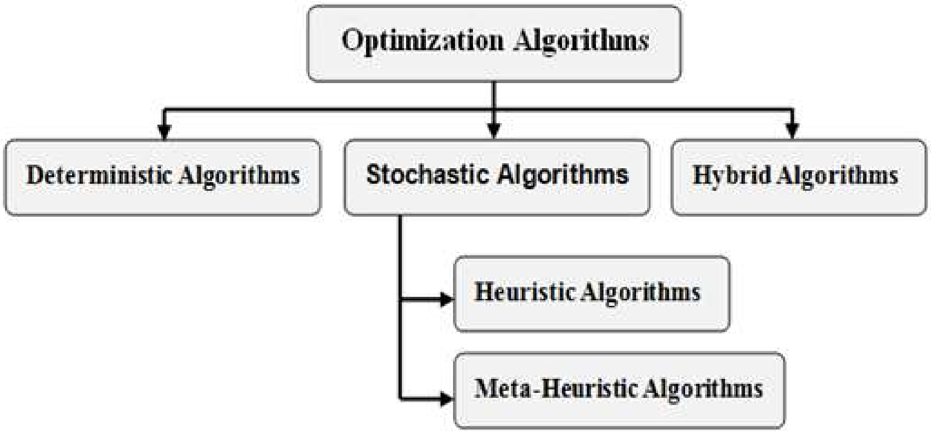

Figure 3-1 The general classification of the optimization algorithms.

3.3.1. Deterministic algorithms

Several optimization algorithms have been developed in recent years. Many of these algorithms fall under deterministic algorithms. Deterministic algorithms use the problem's analytical features to create a series of points that eventually converge on a global optimum solution. Although heuristic techniques have been demonstrated to be more flexible and efficient than deterministic approaches, the quality of the answer achieved cannot be guaranteed.

3.3.2. Stochastic Algorithms

In the past 50 years, since the development of digital computers, many investigators have studied the problem of numerically optimizing an objective function. One approach is stochastic optimization, in which the search for the optimal solution involves randomness in some constructive way. Different communities in stochastic optimization differ in both how they approach modeling, and most approach the problem of searching over policies by working within one or two classes of policies.

3.3.3. Hybrid Algorithms

Hybrid algorithms are a combination of the aforementioned algorithms. These algorithms combine the advantages of deterministic algorithms and stochastic algorithms to overcome the disadvantages of both of these algorithms.

3.4. Meta-heuristic algorithms

Meta-heuristic algorithms are described as a "master strategy that guides and alters other heuristics to obtain answers that go beyond those that are ordinarily generated in a search for local optimality" [4]. These algorithms employ a combination of randomization and local search to achieve their results. A good solution for difficult optimization problems can be found in a reasonable time.

3.4.1. Classification of meta-heuristic algorithms

The main objective of meta-heuristic algorithms is to find solutions that are optimal as possible. Most of these algorithms are inspired by nature, but few have drawn motivation from other processes such as physics/chemistry, social sciences, sports-based, etc [48].

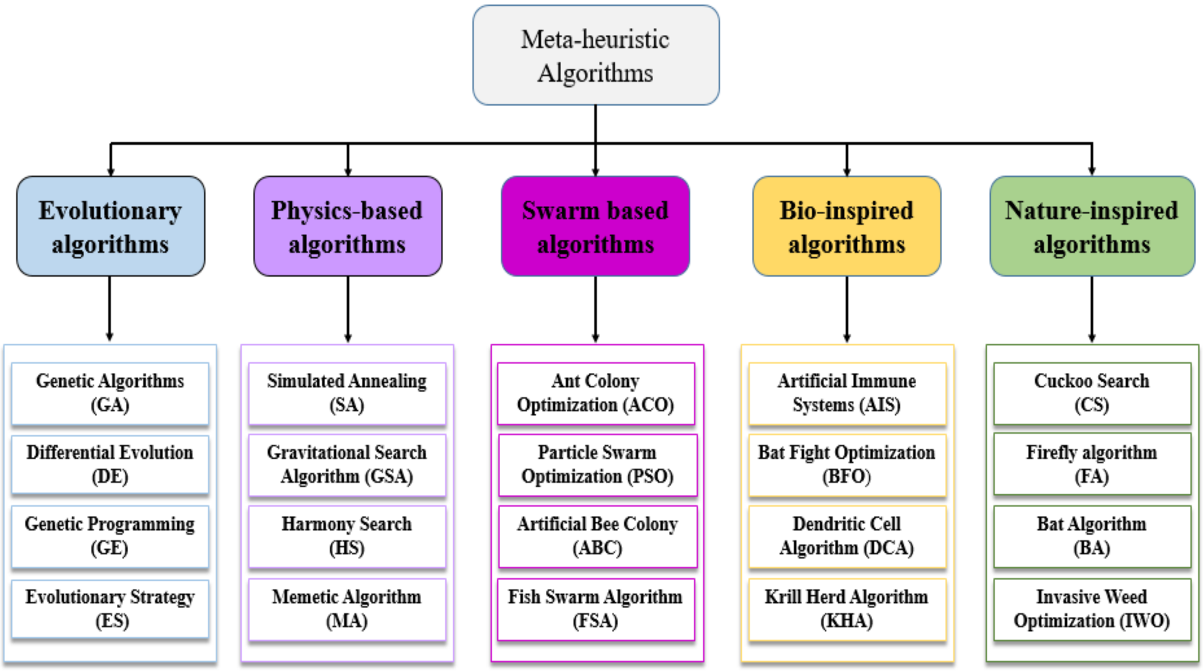

Figure 3-2 Classification of meta-heuristic algorithms.

3.4.1.1. Evolutionary algorithms

In evolutionary algorithms, a population (i.e. a set of solutions) attempts to survive based on an assessment of fitness in a given environment because it is primarily inspired by the theory of natural selection. This type of algorithm performs well near optimal solutions for all types of problems because these methods ideally do not make any assumptions about the underlying fitness or the adaptive landscape [49]. The most famous algorithms belonging to this category : Genetic Algorithms (GA) [50], differential evolution (DE) [51], Genetic Programming (GP) [52] and Evolutionary Strategy (ES) [53].

3.4.1.2. Physics-based algorithms

The main source of Physics based algorithms is physical phenomena. The most well-known algorithm based on physics is the gravitational search algorithm (GSA) [54]. This algorithm is based upon gravity and motion which are the basic laws of physics. The physics-based algorithms also include other types of algorithms such as Simulated Annealing (SA) [55], Harmony Search (HS) [56], Memetic Algorithm (MA) [57].

3.4.1.3. Swarm based algorithms

Swarm-based algorithms are algorithms inspired by the behavior of a group (swarm) of organisms found in nature and are called swarm optimization algorithms. These algorithms fall under what is known as swarm intelligence (SI), inspired by the collective intelligent behavior of animals. SI is based on behavior teamwork among agents in a given environment to achieve their goals. This behavior is different organizational format aiming to solve problem which includes: distributed, self-organizing and de centralization within the environment [48]. This class of algorithms includes: Ant Colony Optimization (ACO) [58], Particle Swarm optimization (PSO) [59], Artificial Bee Colony (ABC) [60], Fish Swarm algorithm (FSA) [61].

3.4.1.4. Bio-inspired algorithms

Biology-inspired meta-heuristic algorithms are the most algorithms common and widely used in optimization. In addition, these algorithms generally rely on a metaphor of a typical biological process or interaction. These algorithms include many algorithms, including but not limited: Artificial Immune Systems [62], Bat Fight Optimization (BFO) [63], Dendritic Cell Algorithm (DCA) [64], Krill Herd Algorithm (KHA) [65].

3.4.1.5. Nature-inspired algorithms

Nature-inspired algorithms are algorithms extracted from the system of nature. These algorithms are stochastic, far from the design of deterministic heuristics [66]. Among the algorithms that belong to this class: Cuckoo Search (CS) [67], Firefly algorithm (FA) [68], Bat Algorithm (BA) [69], Invasive Weed Optimization (IWO) [70]

3.4.2. Meta-heuristic algorithm for image registration

3.4.2.1. Particle swarm optimization

Particle swarm optimization (PSO) is a population-based meta-heuristic optimization method. Was proposed by Eberhart and Kennedy in 1995, which is a stochastic optimization technique that simulates the animal's social behavior when searching for food, including insects, herds, birds and fishes, and is therefore dependent mainly on swarm [71]. The algorithm configuration is related to a group of particles, where each of the particles represents a candidate solution to a problem and has the following three main attributes: the position in the search space $X_i(t)$, the current velocity $V_i(t)$ and the best position ever found by the particle during the search process $X_i^*(t)$ [72]. The velocity of each particle is adjusted by the following equations:

$$V_i(t+1) = wV_i(t) + C_1R_1\left[X_i^*(t) - X_i(t)\right] + C_2R_2\left[X_g^*(t) - X_i(t)\right] \tag{3-1}$$

Here

$$w = \left(w_{max} - w_{min}\right)\left(\frac{T_{max} - 1}{T_{max}}\right) \tag{3-2}$$

Where $X_i^*(t)$ is the best position of each particle which represents the private best objective (fitness) value so far obtained, and $X_g^*(t)$ is the global best particle which denotes the best position among all particles in the population. ω represents the inertia weight which is used to maintain the particle, C_1 and C_2 represent cognition learning and social learning factor, respectively, and R_1, R_2 are the uniformly generated random numbers in the range of [0, 1]. The process of moved each particle by adding speed to the current position is as follows:

$$X_i(t+1) = X_i(t) + V_i(t+1) \tag{3-3}$$

Where $X_i(t+1)$ is the new position, and $V_i(t+1)$ indicates the new velocity.

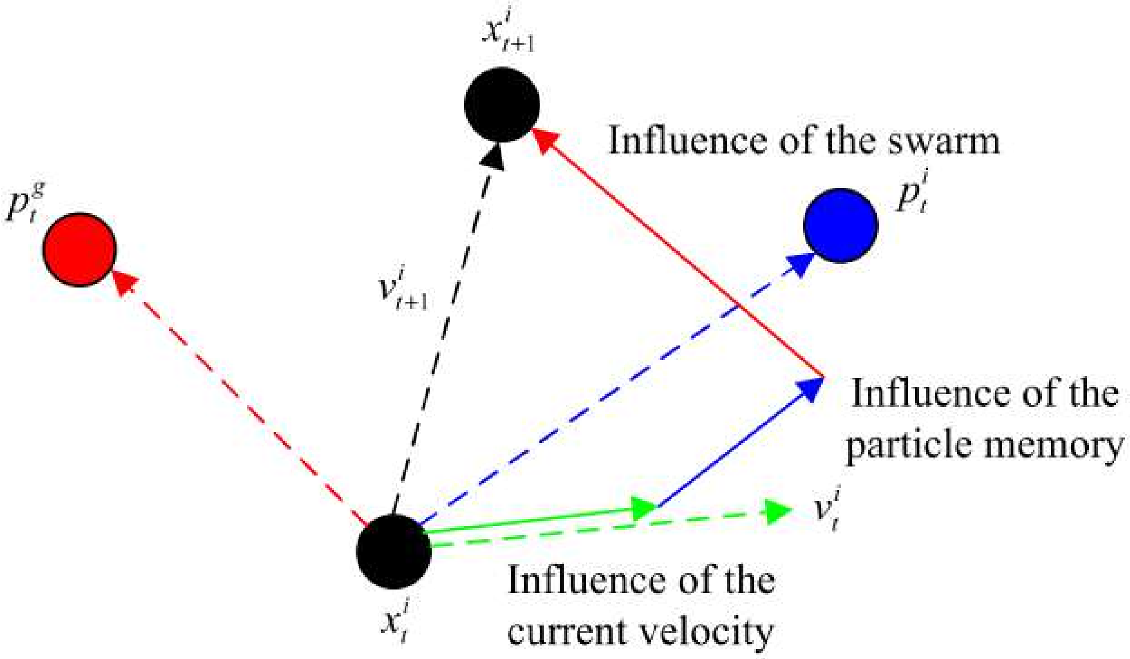

Figure 3-3 The three forces acting on a PSO particle [47].

3.4.2.2. Grey wolf optimizer

The gray wolf algorithm is an algorithm inspired by the gray wolves' living system in the wild, which belong to a canadian family. These wolves prefer to live in groups, the group size is each averaging between 5 and 15, and follow a strict dominant social hierarchy [73]. Gray wolves are divided into three groups, each of which has a different role to play. Among the set of possible solutions, the best solution appears in alpha wolves.

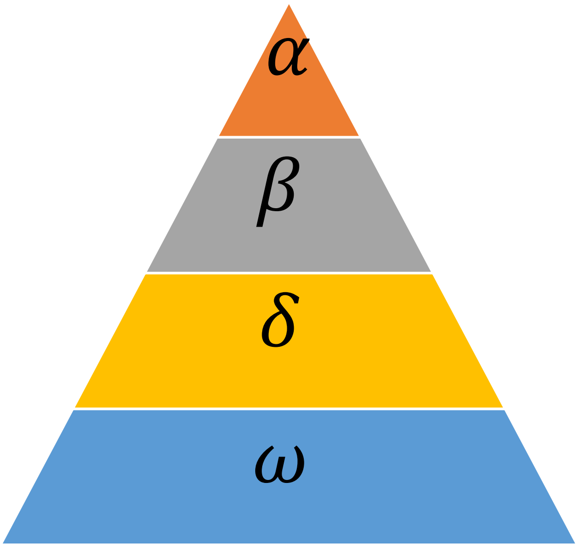

Figure 3-4 Hierarchy of grey wolf (dominance decreases from top down).

This type of wolves depends on encircling the prey from several directions as a basic stage for hunting it, In order to mathematically model encircling behavior the following equations are proposed:

$$\vec{X}(t+1)=\vec{X}_p(t)-\vec{A}.\vec{D} \tag{3-4}$$

Where $\vec{X}$ and $\vec{X}_p$ the grey wolf and target position, respectively, t is the number of iteration and $\vec{D}$ is distance vector calculated as:

$$\vec{D}=\left|\vec{C}.\,\vec{X}_p-\vec{X}(t)\right| \tag{3-5}$$

Here, $\vec{A}$ and $\vec{C}$ are the coefficient vectors. These coefficient vectors are shown in equations 3-6 and 3-7, respectively.

$$\vec{A}=2.k.\vec{p}_1-k \tag{3-6}$$

$$\vec{C}=2.\vec{p}_2 \tag{3-7}$$

Where $K=2-t\left(\frac{t}{T_{max}}\right)$ is decreased from 2 to 0 linearly through the number of iterations, T_{max} is total number of iterations and $\vec{p}_1$, $\vec{p}_2$ are two random vectors between [0, 1]. The alpha is responsible for directed the fishing pattern of the wolves. Beta and Delta are also involved in fishing. Thus, the first three best solutions are chosen to be the hunting wolves, and their current positions can update all wolves' positions. The formulas in this regard are as follows:

$$\begin{cases}\vec{D}_\alpha=\left|\vec{C}_1.\vec{X}_\alpha-\vec{X}\right|\\ \vec{D}_\beta=\left|\vec{C}_2.\vec{X}_\beta-\vec{X}\right|\\ \vec{D}_\delta=\left|\vec{C}_3.\vec{X}_\delta-\vec{X}\right|\end{cases} \tag{3-8}$$

After computing the difference vectors $\vec{D}_\alpha$, $\vec{D}_\beta$, and $\vec{D}_\delta$, as well as the updated states for (t+1), the iteration can be computed as follows:

$$\begin{cases}\vec{X}_1=\vec{X}_\alpha-\vec{A}_1\vec{D}_\alpha\\ \vec{X}_2=\vec{X}_\beta-\vec{A}_2\vec{D}_\beta\\ \vec{X}_2=\vec{X}_\delta-\vec{A}_3\vec{D}_\delta\end{cases} \tag{3-9}$$

$$\vec{X}(t+1)=\frac{\vec{X}_1+\vec{X}_2+\vec{X}_3}{3} \tag{3-10}$$

Where $\vec{A}_1$, $\vec{A}_2$, and $\vec{A}_3$ are the random vectors.

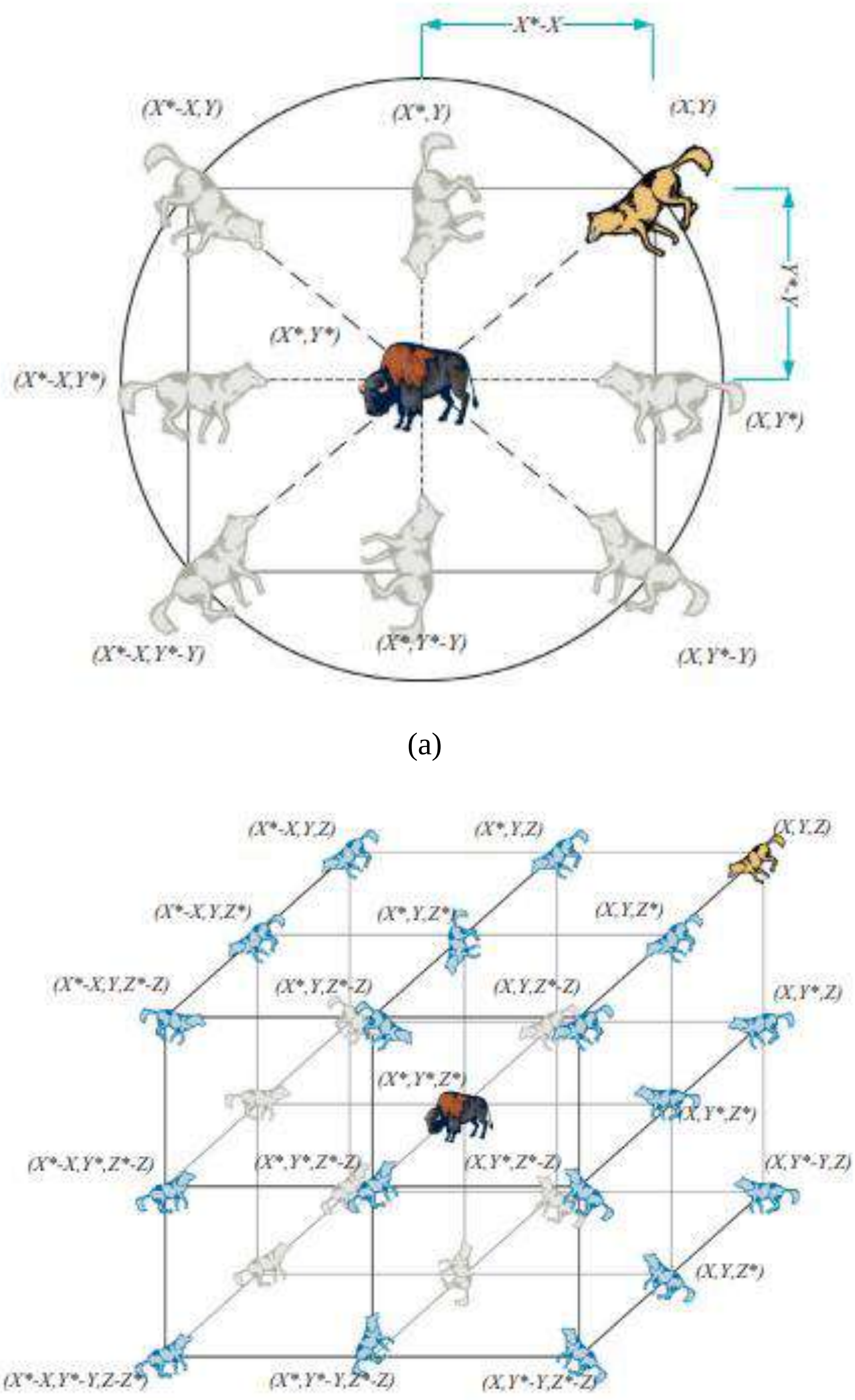

(a)

(b)

Figure 3-5 The possible next locations of 2D and 3D position vectors [74].

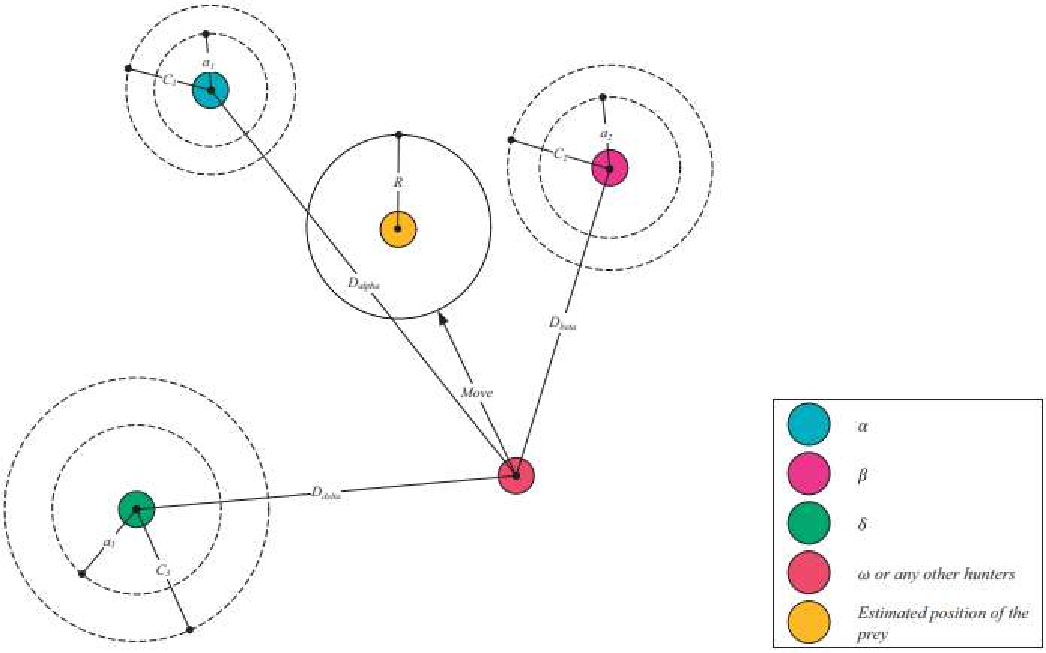

Figure 3-6 Diagram showing how to update the position in GWO algorithm.

3.4.2.3. Firefly algorithm

Firefly Algorithm (FA) is a randomization-based optimization algorithm to find solutions inspired by the nature of fireflies and their ability to glow [75]. This algorithm is described by the rhythmic flashes that fireflies send in order to warn of the possibility and the presence of prey or to bring in other fireflies easily. Least brighter fireflies move in the direction of the other brighter fireflies, that is, the greater the distance between the fireflies, the attractiveness decreased between the fireflies, which leads to random movement of the fireflies [76]. Equation 3-11 illustrates the variation of the firefly's light attractive coefficient β with the distance r between the heifers [77].

$$\beta = \beta_0 e^{-\gamma r^2} \tag{3-11}$$

Where β_0 is the attractiveness at zero distance ($r = 0$) and normally set to 1. Moreover, γ is the light absorption coefficient.

Like many meta-heuristic algorithms, the firefly algorithm is population-based, as shown in **Figure 3-7**, which illustrates the general concept of this algorithm.

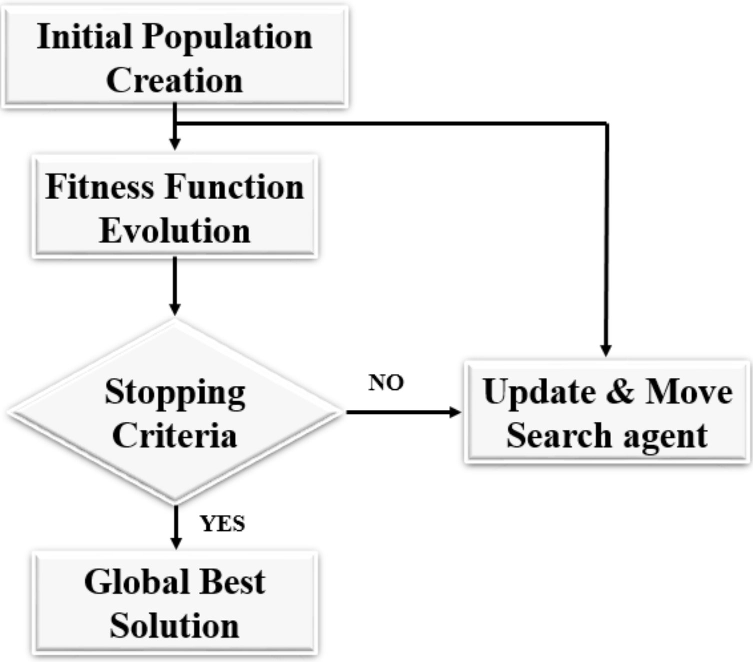

Figure 3-7 The general framework of the Firefly algorithm.

3.4.2.4. Crow searchal algorithm

The CSA algorithm was inspired from crows behavior in obtaining their food. Crows depend on stealing to obtain their food, as they follow other birds and take food after those birds leave their hiding place [78]. The behavior of the crows prompted researchers to create an algorithm that mimics this behavior, called it crow search algorithm. Equation 3-12 illustrates the formula in which crows change their position while observing the awareness of other birds [79]:

$$X_i^{t+1} = \begin{cases} X_i^t + r_i \times fl_i^t \times \left| m_i^t - X_i^t \right| & r_i \geq AP_i^t \\ \textit{a random position} & \textit{otherwise} \end{cases} \tag{3-12}$$

Where AP_i^t represents the awareness of the crow j. If the victim bird knows that the crow is following it, he will try to take the crow to a random location. For each crow j, a crow j is selected randomly to update the position of crow i [79].

3.4.2.5. Sine Cosine algorithm (SCA)

Generally, the principle of starting from a set of random solutions to the optimization process is the basic concept of population-based optimization techniques. This random set is evaluated iteratively handled by an objective function and then optimized based on a set of rules representing the optimization kernel. The sine cosine algorithm proposed by Mirjalili [80] is a population-based optimization technique. It begins by generating a set of random solutions, and then, these solutions are updated based on the sine or cosine function as in equation 3-13.

$$X_i^{t+1} = \begin{cases} X_i^t + r_1.\sin\left(r_2\right).\left|r_3 P_i^t - X_i^t\right|, & r_4 < 0.5 \\ X_i^t + r_1.\cos\left(r_2\right).\left|r_3 P_i^t - X_i^t\right|, & r_4 < 0.5 \end{cases} \tag{3-13}$$

Where P_i^t is the position of the destination point in i-th dimension at iteration t, X_i^t is the position of current solution in i-th dimension. r_1, r_2, r_3 and r_4 are random variables and are uniformly distributed between 0 and 2π, 0 and 2, and between 0 and 1 respectively as shown in **Figure 3-8**.

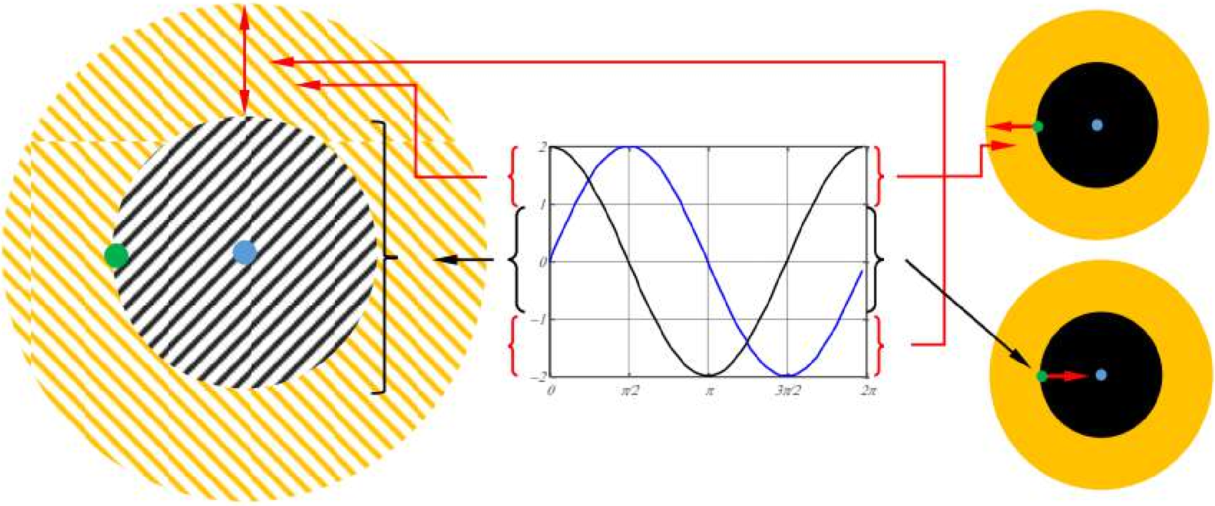

Figure 3-8 In the range [-2, 2] the sine and cosine allow a solution to go around (inside the space between them) or beyond (outside the space between them) the destination [80].

The random variable r_1 is responsible for the area of the next solution, which can be either in the space between the solution and the destination or outside it. The variable r_1 is updated as:

$$r_1 = a\left(1 - \frac{t}{T_{max}}\right) \tag{3-14}$$

Where a is a constant, T_{max} is the maximum iterations. The process of decreasing the range of sine and cosine functions over the iterations explained by equation 3-14 is clearly shown in **Figure 3-9** [80].

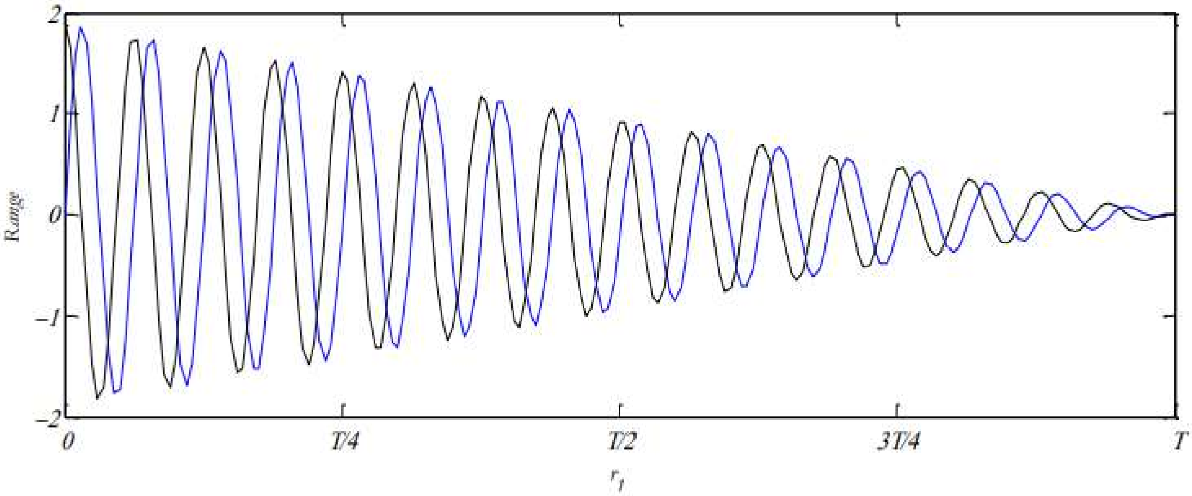

Figure 3-9 Decreasing pattern for range of sine and cosins.

3.5. Applications of meta-heuristics algorithms

Meta-heuristics algorithms have been applied in many fields according to the target problem. Among the applications in which these algorithms are used, we mention the following:

- Problem solving in the medical field (medical image processing)
- Optimization in the electronic field such as image processing of printed circuits
- In the electric field (maximizing the electric power output)
- In the field of telecommunications
- Robotics

3.6. Conclusion

Meta-heuristic algorithms have been widely used in recent years in various journals. Moreover, new algorithms have been developed that combine the advantages of other algorithms. To this day, the production of these algorithms is still connected. In this chapter, indicative algorithms, their types, some famous algorithms, and finally the applications of these algorithms were introduced. The remaining chapters present contributions resulting from the application of proposed methods for registration and fusion of images. These contributions included the medical and electronic field.

CHAPTER 4 IMAGE REGISTRATION BASED ON META-HUEURISTIC ALGORITHMS

4.1. Introduction

This chapter is dedicated to presenting the results of the registration of medical images based on meta-heuristic algorithms. Firstly, an algorithm was applied for the grey wolf optimizer (GWO), sine cosine algorithm (SCA), and particle swarm optimization (PSO) to register the MRI and CT images. Second, with the emergence of Covid-19 disease and the radiologist's need in the world for an image that facilitates the process of diagnosing this dangerous disease, an improved sine cosine algorithm (ISCA) and HPSGWO algorithm are developed to register CT images of lung infected with COVID-19.

This chapter is divided into three main sections: The first section contains a definition of the databases used in this study. The second section shows the registration results obtained in the three cases: MRI and CT image registration based on the GWO algorithm, and then the application of the two developed algorithms (HPSGWO and ISCA) to register CT images of lungs infected with COVID-19.

4.2. Grey wolf Optimizer for multimodal medical image registration

4.2.1. Description of the proposed method

Firstly, a test image and reference image will be converted into gray image, and then the transformation matrix is calculated to transform the test image into the same orientation and position as the reference image. The floating (test) image is obtained in the experiment by applying a translation $(t_x\ ,\ t_y\ ) = \left(-1,-1\right)$ and a rotation $\theta = 1/2$ of the image of truth to the ground. The GWO, SCA, and PSO algorithms were used to multimodal registration of these two pairs images with a similar population size of 25 and maximum iteration value of 100 iterations.

To demonstrate the accuracy of the recording for our method, we applied the GWO, SCA, and PSO algorithms in a multimodal registration process for two-dimensional (2D) images of a human brain. The algorithms were applied to a pair of images (MRI-1, CT-1) and (MRI2, CT2) in a multimodal fashion.

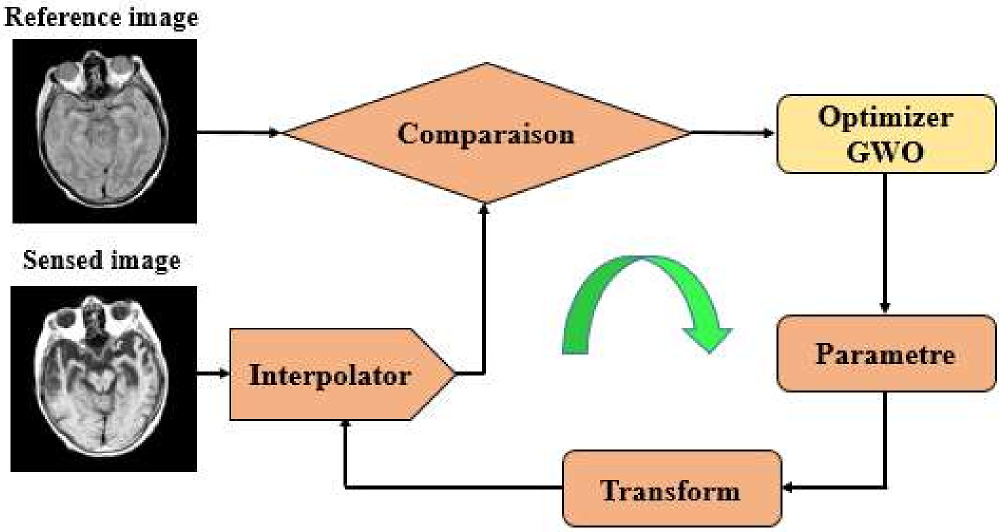

Figure 4-1 Principle of the proposed method.

4.2.2. Experiment setup and results

4.2.2.1. Dataset of MRI and CT images

The test images are collected from the Harvard University Medical School's Entire Brain Atlas Database [81]. Four types of MRI and CT images are considered: (CT-1) Indicates the first CT image, (CT-2) indicates a second CT image, (MRI-1) indicates the first MRI image, and (MRI-2) indicates a second MRI. As shown in **Figure 4-2** respectively: (a) represents the first pair of images (MRI-1, CT-1) and (b) represents the second pair of images (MRI-2, CT-2).

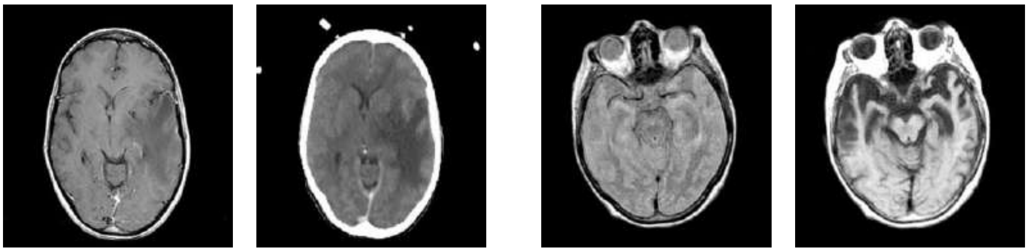
(a) (b)

Figure 4-2 MRI and CT images: (a) dataset1and (b) dataset2.

4.2.2.2. Results

In the first simulation, we recorded two images MRI-1 and CT-1 and in the second simulation, we recorded two images MRI-2 and CT-2. The **Table 4-1** illustrates the registration parameters the SSIM, NMI values and MSE of image pairs. The bold numbers represent the best results obtained. We can see that the proposed algorithm found optimal or best solutions in this test over 25 runs.

Table 4-2 Registration results for multi-modality images of the first image pair.

Modalities	**Algorithms**	$-\theta$	$-t_x$	$-t_y$	**SSIM**	**NMI**	**MSE**	**Tims (S)**
MRI-1/CT-1	**GWO**	**0.0071**	**0.9958**	**1.0034**	**0.9078**	**2.1152**	**0.0417**	**6.3318**
	SCA	0.0152	0.9804	1.0007	0.8934	2.0650	0.0566	6.8300
	PSO	0.0001	1.0000	1.0000	0.9071	2.1452	0.0423	10.9353
MRI-2/CT-2	**GWO**	**0.0015**	**0.9994**	**1.0004**	**0.9184**	**1.9508**	**0.0648**	**7.0710**
	SCA	0.0158	0.9949	0.9976	0.8934	1.8889	0.0775	6.8300
	PSO	0.0001	1.0000	1.0000	0.9071	2.1452	0.0423	11.4208

Figure 4-3 shows the evolution of the three algorithms that were used to register first and second pair, MRI-1, CT-1 and MRI-2, CT-2 respectively. It shows us that the PSO and GWO algorithms converge after the number of iterations 20 and 40, respectively, however, the SCA algorithm needs nearly 85 iterations to converge. The uptime that the GWO algorithm takes is a little compared to SCA and PSO algorithms.

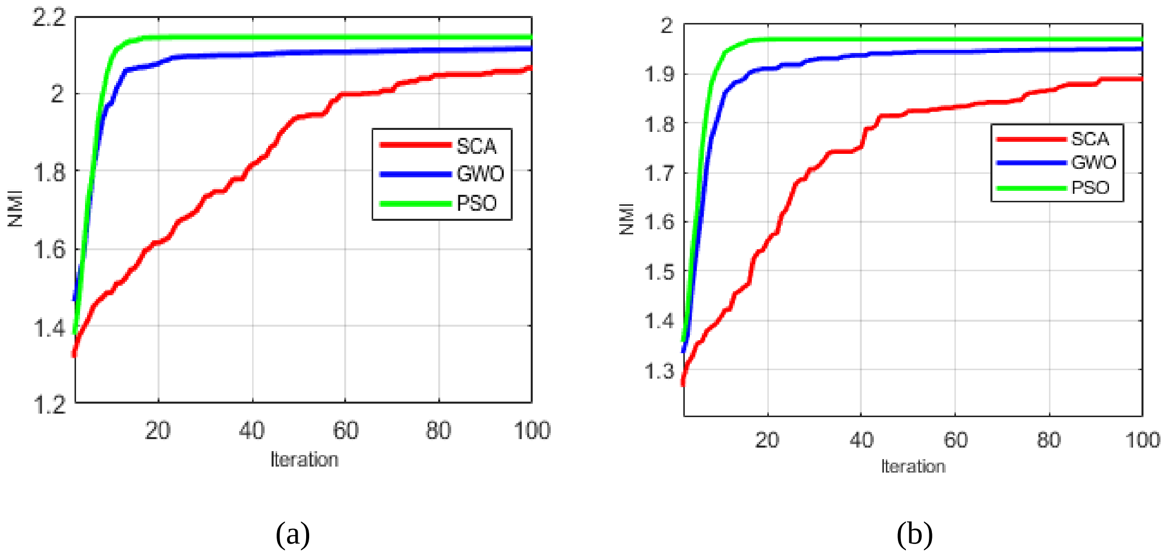

(a) (b)

Figure 4-3 Convergence curves for multimodal image registration of the first image pair (MRI-1, CT-1).

The visual results of the proposed GWO algorithm of pairs MRI-1, CT-1 and MRI-2, CT-2 are shown in **Figure 4-4** and **Figure 4-5** where good performance of our new method is shown because the GWO algorithm has higher INM and SSIM values, which indicate better registration results.

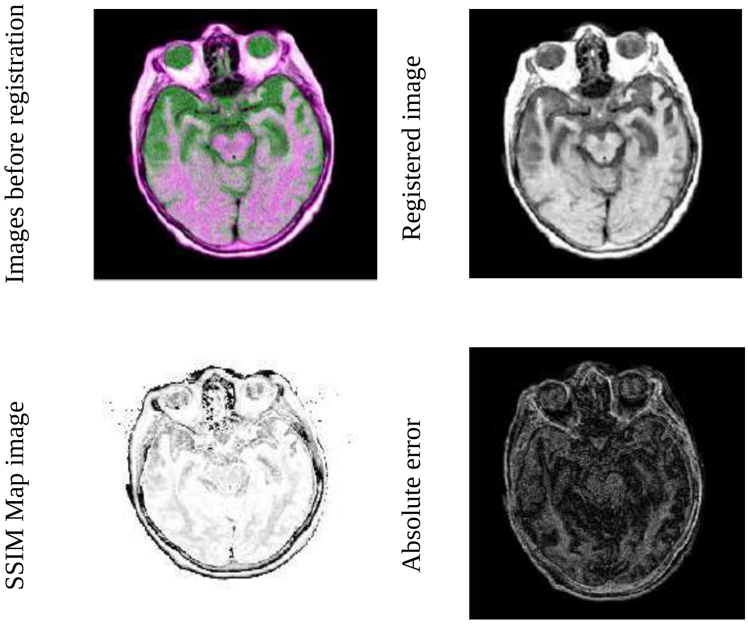

Figure 4-4 Visual results for multimodal image registration using GWO of the first image pair (MRI-1, CT-1).

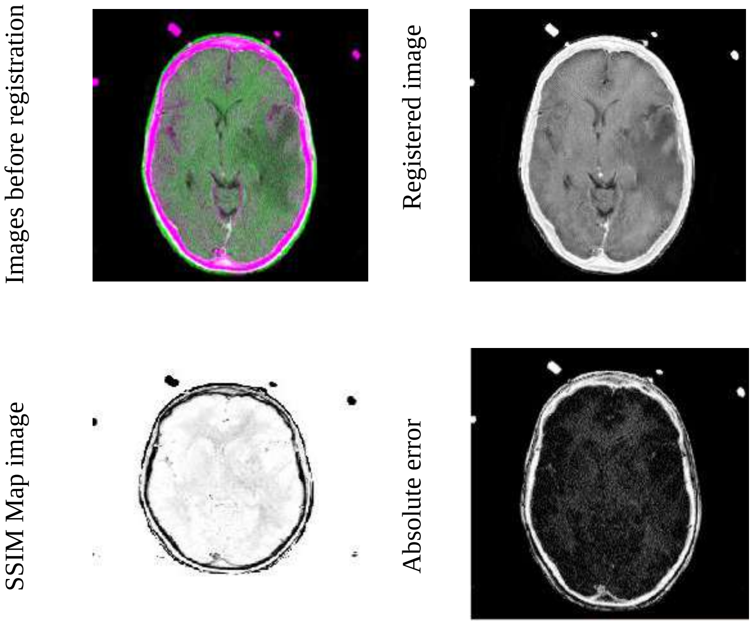

Figure 4-5 Visual results for multimodal image registration using GWO of the second image pair (MRI-2, CT-2).

4.3. Registration of computed tomography images of a lung infected with COVID-19 based in the new meta-heuristic algorithm HPSGWO

4.3.1. A review for covid-19 image registration

Computed tomography (CT) helps the radiologist in the rapid and correct detection of a person infected with the coronavirus disease 2019 (COVID-19), and this by showing the presence of the ground-glass opacity in the lung of with the virus. Tracking the evolution of the spread of the ground-glass opacity (GGO) in the lung of the person infected with the virus needs to study more than one image in different times. The various CT images must be registration to identify the evolution of the ground glass in the lung and to facilitate the study and identification of the virus. Due to the process of registration images is essentially an improvement problem, we present in this paper a new HPSGWO algorithm for registration CT images of a lung infected with the COVID-19. This algorithm is a hybridization of the two algorithms Particle swarm optimization (PSO) and Grey wolf optimizer (GWO). The simulation results obtained after applying the algorithm to the test images show that the proposed approach achieved high-precision and robust registration compared to other methods such as GWO, PSO, Firefly Algorithm (FA), and Crow Searcha Algorithms (CSA).

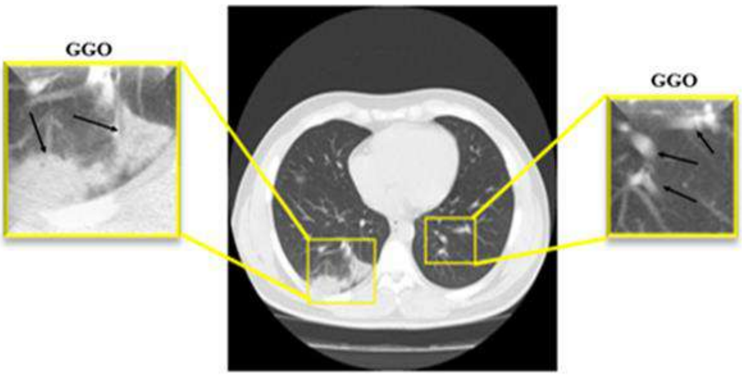

Figure 4-6 CT scan results of a virus-infected lung showing the presence of GGO on both sides of the lung.

4.3.2. Related work

The field of image analysis is wide and varies according to the method used in image processing, as most of them aim to reduce noise, provide a clearer image, and contains the required amount of information. Several methods have been adopted in the field of image processing, some of which are based on the convolution network [82], including those based on iterative Structure-adaptive Fuzzy Estimation [83], as well as based on an artifact suppressed dictionary learning [84]. This work is about medical image registration especially the CT images of the lung of a person with COVID-19. The main of this work is to obtain a more detailed image with an acceptable amount of information to facilitate the diagnosis of infection with this virus.

4.3.3. Proposed method

Our proposed method is based on the use of PSO and GWO meta-heuristic algorithms (called HPSGWO) to register the CT images of the lungs of a COVID-19 patient that were taken at different times **Figure 4-2**.

4.3.3.1. Hybrid PSO-GWO algorithm

Grey wolf optimizer (GWO) and Particle swarm optimization (PSO) algorithms each have features that determine their importance in overcoming various optimization problems [85], [86]. While each of the aforementioned algorithms has flaws in the way it searches for solutions to a problem.

- **PSO algorithm**

Despite the advantages of the PSO algorithm, such as the robustness in solving many optimization problems, not to mention the simplicity and ease of implementation, it often falls into the minimum solutions when it is subjected to severe restrictions [85].

- **GWO algorithm**

The gray wolf algorithm maintains a balance between exploration and exploitation and often avoids being trapped locally. It is also characterized by speed and accuracy of results. Despite all this, it remains limited compared to PSO in overcoming many problems.

This approach was inferred by GWO using wolves ‘positions α, β, and δ in determining the solution as shown in equation 4-1 with wolves’ position updated on the one hand, and by PSO using gbest, pbest, and inertia (w) as shown in equation 4-2, as it provides him with information about tracking and discovering the best location of particles from another side. The hybrid approach used the orientation characteristic used by GWO with the prior knowledge provided by PSO by gbest, pbest and inertia (w) to obtain an algorithm that has broad ability to overcome the problems of image registration, accuracy in results and speed in performance [85]. This hybrid approach can be described by increasing the GWO performance. Equation 4-3 Q_{CB} shows the positions customized to the wolf:

$$\vec{X}_{wolf}\left(t+1\right)=\frac{\vec{X}_1+\vec{X}_2+\vec{X}_3}{3} \tag{4-1}$$

Here the mean of the best three can be calculated and it represents the the gbest of the proposed algorithm. The pbest and inertia (w) are predicted in the same way as the traditional PSO algorithm. The estimation of the positions of the new GWO algorithm related to the PSO algorithm is shown in the following equation:

$$\vec{X}_i^{t+1}=w\vec{X}_i+C_1.R_1\left(\overrightarrow{pbest_i}\right)+C_2\left(1-R_2\right)\left(\overrightarrow{gbest}\right) \tag{4-2}$$

Here:

$$gbest=\frac{\vec{X}_1+\vec{X}_2+\vec{X}_3}{3} \tag{4-3}$$

Here, R_1 and R_2 are the random variables are bound between [−1, 1] unlike in PSO, it is limited between [0, 1].

The proposed algorithm initially relies on the features of PSO to define the search area as well as on GWO to provide the best convergence. The HPSGWO algorithm finds the perfect solution with a suitability account for each search agent, updating the current search agent for each search agent. The coefficient vectors and inertia particles will then continue to be updated until the global optimum solution is obtained. Algorithm 1 shows the proposed algorithm:

Algorithm 1 : HPSGWO

```
Initialize the GW population $X_i\left(i=1, 2,….., N\right)$
Initialize A, and D
Calculate the fitness of each search agent
$\vec{X}_\alpha$ = the best search agent
$\vec{X}_\beta$ = the best search agent
$\vec{X}_\delta$ = the best search agent
while (t < $T_{max}$ )
    For each candidate solution
        Update the position of the current  search agent by equations 3-1, 3-4, and 4-2
```

```
        end for
        Update A, and D using equation 3-1 and 4-3
        Calculate the fitness of all search agents.
    Update $\vec{X}_{\alpha}$, $\vec{X}_{\beta}$, and $\vec{X}_{\delta}$
    t = t+1
    end while
Return the best solution obtained so far as the  global optimum
```

4.3.4. Experiments and results

In this section, we will perform a series of mono-modal and multi-modal images registrations process to demonstrate the effectiveness of the new algorithm HPSGWO. The first stage of this section describes the image dataset we used in the registrations process. In the second stage, the results of the registration processes obtained after applying the proposed algorithm are presented and compared with the results of the PSO, GWO, FA, and CSA algorithms. All results of registration are obtained using the MATLAB R2020, on a computer having an Intel (R) Xeon (R) Silver 4108 GPU @1.80 GHz.

4.3.4.1. Datasets of COVID-19 images

The COVID-19 test images used in the first approach (HPSGWO) were obtained from the famous database “Radiopaedia” https://radiopaedia.org/articles/covid-19-4, which provides modern CT images of the lungs of people infected with COVID-19 of all ages. Four types of computed tomography images are taken which are considered: The first CT image is denoted to as (CT-I1), the second image is CT-I2, the third image is (CT-I3), and the fourth image is (CT-I4) as shown in **Figure 4-7**.

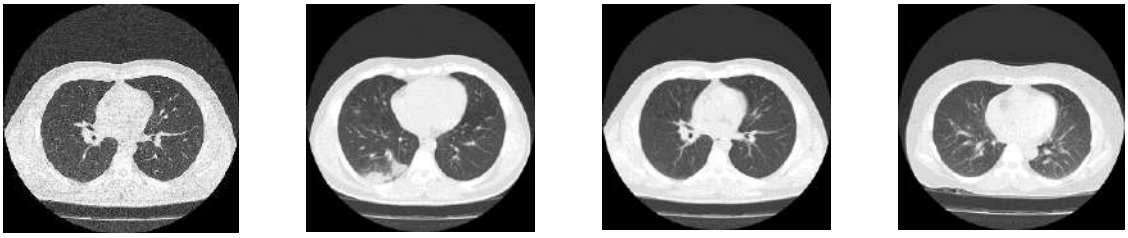

(a) CT-I1 (b) CT-I2 (c) CT-I3 (d) CT-I4

Figure 4-7 Real 2D images of the lungs infected with COVID-19.

4.3.4.2. Accuracy of the registration process

In the experiments, the obtained of floating images by applying the following: translation $\left(t_x, t_y\right)=(7,7)$ rotation of θ = 5° to the ground truth image, and similar population size of 25 and a maximum iteration value of 100 iterations to registred each pair of images.

To confirm the effectiveness of the proposed algorithm and to clarify its performance in the image registration process and demonstrate the superiority of the proposed algorithm over the source algorithms, we applied the algorithms PSO and GWO separately on real 2D CT image pairs CT-I1, CT-I2, CT-I3, and CT-I4. These two algorithms have shown good results in registering pairs of magnetic resonance imaging (MRI) and computed tomography (CT) images in a previous study in [5]. On the other hand, due to the good results achieved by the FA and CSA algorithms in many optimization problems such as [87], [88], [89], [90] and [91] respectively, these two algorithms were applied and the results obtained were compared with the results of the proposed algorithm. The algorithms were applied to a pair of “CT-I1” and “CTI2” images of a lung infected to COVID-19 as a mono-modal, and the two pairs of “CT-I1 and CT-I2”, “CT-I3 and CT-I4” as multi-modal.

In the first stage of this experiment we considered the two pairs of CT images as mono-modal ((CT-I1, CT-I1) and (CT-I2, CT-I2)). The simulation results showed that the proposed algorithm HPSGWO is faster and more accurate in mono-modal registration of the two images pairs compared to the PSO, GWO, FA, and CSA algorithms. Tables 4-2 shows the registration parameters for the SSIM, NMI, and Q_{CB}, values for each pair of images. It clearly shows that the proposed algorithm has found the optimal solutions to the registration process and within a short period on all tests over 20 runs. The maximum SSIM, INM, and Q_{CB} values in the proposed algorithm appear in both registration. **Figure 4-11** shows the percentages of the algorithms used based on SSIM, which further illustrate the superiority of the proposed algorithm for mono-modal registration of the two image pairs.

Table 4-3 Results for mono-modality registration.

Dataset 1					
Moda-lities	**CT-I1/CT-I1**				
Algorithms	**HPSGWO**	**PSO**	**GWO**	**FA**	**CSA**
$-\mathbf{t_x}$	**7.000412**	7.001985	7.019123	6.993805	6.960549
moy	**0,000412**	0,001985	0,019123	0,006195	0,039451
$-\mathbf{t_y}$	6.999678	6.999129	7.006428	**7.000042**	7.013669
moy	0,000322	0,000871	0,006428	**0,000042**	0,013669
$-\boldsymbol{\theta}$	**5.000352**	4.99884	4.999178	4.997836	4.993334
moy	**0,000352**	0,00116	0,000822	0,002164	0,006666
SSIM	**0.999997**	0.999965	0.999966	0.999992	0.999929
NMI	**1.292493**	1.292471	1.292492	1.291718	1.278372
$\boldsymbol{Q_{CB}}$	**0.695892**	0.6782924	0.677178	0.678692	0.677873
Time (S)	**42.94527**	78.36011	48.23693	568.5125	49.00174
Moda-lities	**CT-I3/CT-I3**				
Algorithms	**HPSGWO**	**PSO**	**GWO**	**FA**	**CSA**
$-\mathbf{t_x}$	**6,997868**	7.002332	7.024026	6.996462	7.003539
moy	**0.002132**	0,002332	0,024026	0,003538	0,003539
$-\mathbf{t_y}$	**7,000189**	6.999760	6.967417	7.004477	6.999533
moy	**0,000189**	0,00024	0,032583	0,004477	0,000467
$-\boldsymbol{\theta}$	**5,000348**	4.999471	4.994060	4.997552	4.999305
moy	**0,000348**	0,000529	0,00594	0,002448	0,000695
SSIM	**0.999991**	0.999963	0.999961	0.999992	0.999926
NMI	**1.29421**	1.294632	1.294999	1.295024	1.294632
$\boldsymbol{Q_{CB}}$	**0.680009**	0.666567	0.6632807	0.670559	0.666090
Time (S)	**38.21095**	68.75508	45.64086	506.8556	46.98393

Through **Figure 4-8** showing the evolution of the algorithms used in this experiment (for mono-modal registration), it can be seen that the proposed algorithm HPSGWO and the FA algorithm converge after 45 and 5 iterations, respectively, for the image pairs ((CT-I1, CT-I1) and (CT-I3, CT-I3)). While other algorithms need more than 60 iterations to converge. Despite the high evaluation values of the proposed method compared to other methods, which indicate better registration results, they converge after a large number of iterations compared to FA, which converge after a very small number of iterations. This is due to the reduction in the search area and to get closer to the optimal solution to obtain the best results of registration.

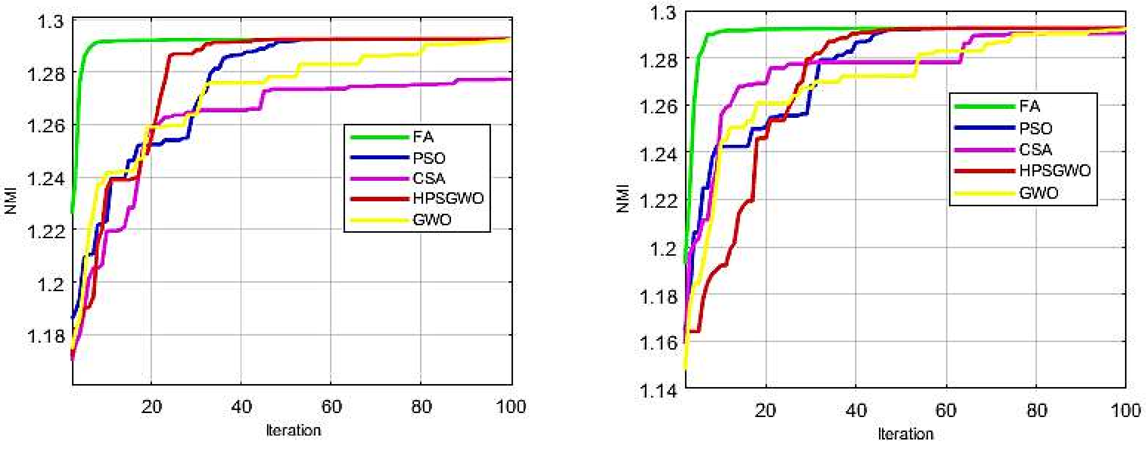

(a) (b)

Figure 4-8 Convergence curves for the algorithms used resulting from mono-modal registration of CT images: (a) CT-I1/CT-I1 and (b) CT-I3/CT-I3.

The visual quality of different mono-modal image registration methods (HPSGWO, PSO, FA, CSA, and GWO) is presented in two **Figure 4-9** and **Figure 4-10**. These results confirm the good performance of the proposed HPSGWO algorithm, as it contains higher SSIM, INM, and Q_{CB} values, that indicating better mono-modal registration results. The green and magenta color distribution show the information of the source image and sensed image, respectively. The difference between images before registration and Registered image confirms the recording effectiveness of the algorithms in general and the proposed algorithm in particular.

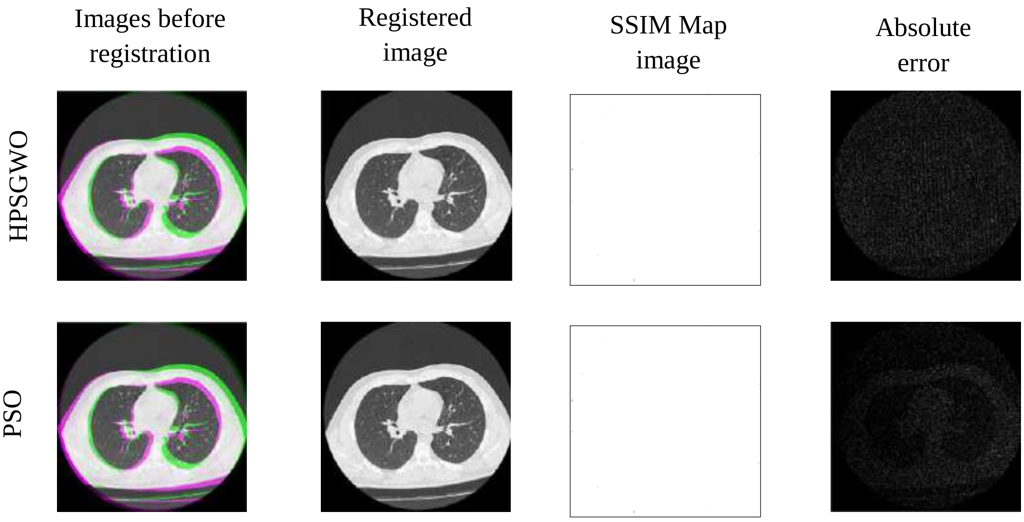

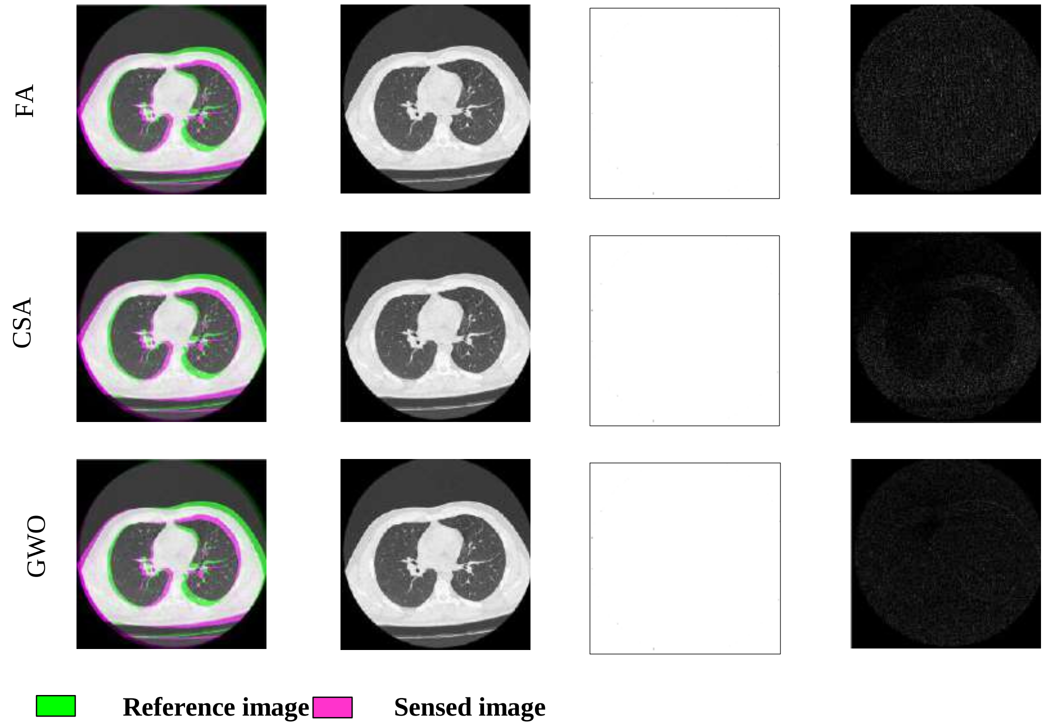

Figure 4-9 Visual results obtained from mono-modal image registration of pair (CT-I1/CT-I1) using the HPSGWO algorithm: (a) Images before registration, (b) Registered image, (c) SSIM Map image, and (d) Absolute error.

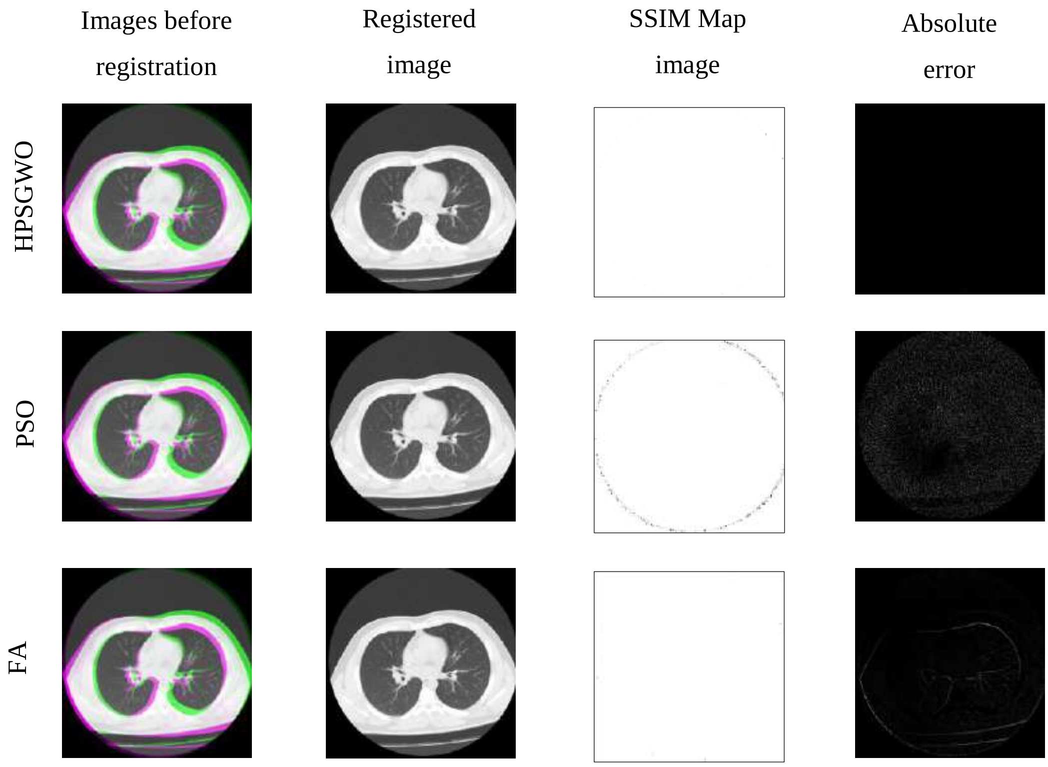

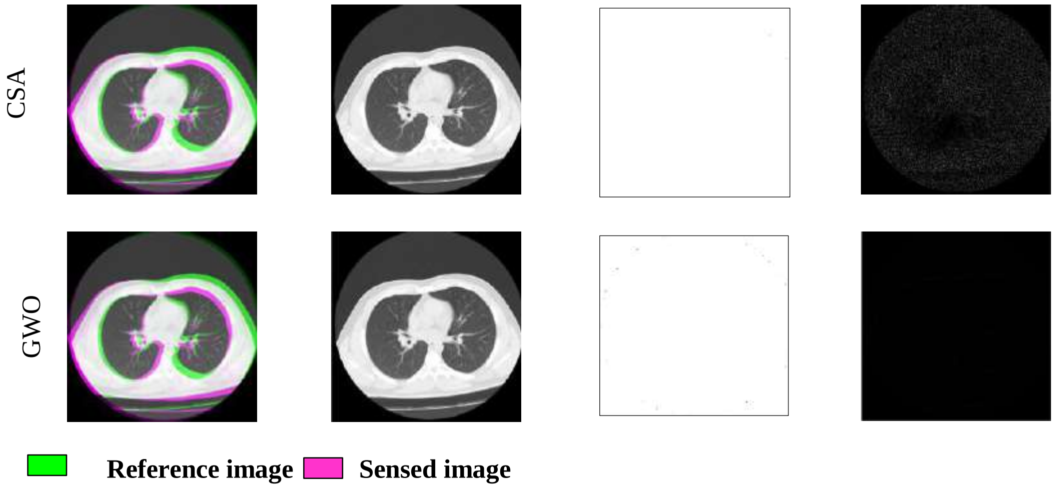

Figure 4-10 Visual results obtained from mono-modal image registration of pair (CT-I3/CT-I3) using the HPSGWO algorithm: (a) Images before registration, (b) Registered image, (c) SSIM Map image, and (d) Absolute error.

- A-frame has been added to the SSIM Map images to show their borders only, this frame does not belong to the resulting images.

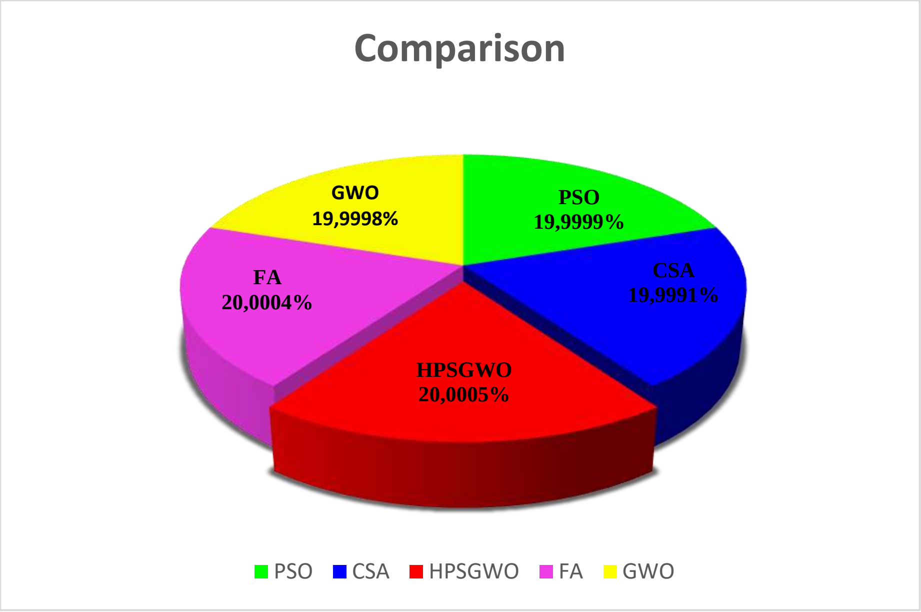

Figure 4-11 Mono-modal images Registration accuracy comparison of HPSGWO, PSO, GWO, FA, and CSA algorithms based on SSIM.

In the second stage of this experiment, we considered the two pairs of CT images as multi-modal ((CT-I1, CT-I2) and (CT-I3, CT-I4)). The simulation results showed that the proposed algorithm HPSGWO is faster and more accurate in multi-modal registration of the two images pairs compared to the PSO, GWO, FA, and CSA algorithms. Tables 4-3 shows the registration parameters for the SSIM, INM, and Q_{CB} values for each pair of images. It clearly shows that the proposed algorithm has found the optimal solutions to the registration process and within a short period on all tests over 20 runs as it happened in mono-modal registration in the first stage. **Figure 4-15** shows the relative percentages of the algorithms used based on SSIM, which further illustrate the superiority of the proposed algorithm for the two multi-modal image pairs registration.

Table 4-4 Results for multi-modality registration.

Dataset 1					
Moda-lities	**CT-I1/CT-I2**				
Algorithms	**HPSGWO**	**PSO**	**GWO**	**FA**	**CSA**
$-\mathbf{t}_{\mathbf{x}}$	**6.998905**	7.002326	6.994191	6.995947	7.001162
moy	**0,001095**	0,002326	0,005809	0,004053	0,001162
$-\mathbf{t}_{\mathbf{y}}$	**6,999758**	6.999748	6.993237	7.005332	6.999105
moy	**0,000242**	0,000252	0,006763	0,005332	0,000895
$-\boldsymbol{\theta}$	4,988744	**4.999480**	5.002055	4.998162	4.999316
moy	0,011256	**0,00052**	0,002055	0,001838	0,000684
SSIM	**0.999996**	0.999963	0.999975	0.999994	0.999919
NMI	**1.285034**	1.284839	1.285023	1.283494	1.285007
$\boldsymbol{Q_{CB}}$	**0.679505**	0.664896	0.674893	0.6646126	0.645959
Time (S)	**32.77379**	46.52661	42.42466	514.6154	73.65165
Moda-lities	**CT-I3/CT-I4**				
Algorithms	**HPSGWO**	**PSO**	**GWO**	**FA**	**CSA**
$-\mathbf{t}_{\mathbf{x}}$	**7,0001231**	7.007505	7.031315	7.009575	7.007565
moy	**0,000123**	0,007505	0,031315	0,009575	0,007565
$-\mathbf{t}_{\mathbf{y}}$	**6,983549**	7.026365	7.032691	7.024802	7.027856
moy	**0,016451**	0,026365	0,032691	0,024802	0,027856
$-\boldsymbol{\theta}$	4.974629	4.997856	4.995340	4.996741	**4.998678**
moy	0,025371	0,002144	0,004660	0,003259	**0,001322**
SSIM	**0.999967**	0.999960	0.999964	0.999961	0.999930
NMI	**1.164344**	1.163759	1.163757	1.163760	1.163728
$\boldsymbol{Q_{CB}}$	**0.681419**	0.670957	0.670544	0.671555	0.651017
Time (S)	**41.21114**	43.84314	41.81606	556.78873	64.29531

Through **Figure 4-12** showing the evolution of the algorithms used in this experiment, it can be seen that the proposed algorithm HPSGWO and the FA algorithm converge after 45 and 5 iterations, respectively, for the image pairs ((CT-I1,CT-I2) and (CT-I3,CT-I4)) as it happened in mono-modal registration in the first stage. While other algorithms need more than 60 iterations to converge. As is the case in mono-modal registration, despite the high SSIM, INM, and Q_{CB} values shown in the proposed method, they converge after a very large number of iterations compared to the FA algorithm. This is due to the reduction in the search area, and to get closer to the optimal solution to obtain the best results of registration.

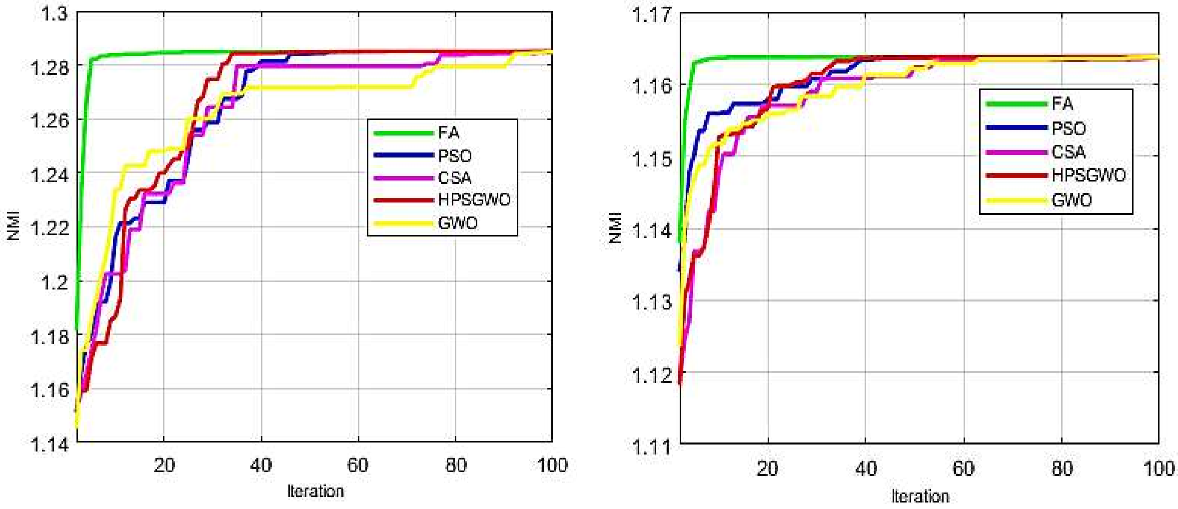

(a) (b)

Figure 4-12 Convergence curves for the algorithms used resulting from multi-modal registration of CT images: (a) CT-I3/CT-I4 and (b) CT-I1/CT-I2.

The visual quality of different multi-modal image registration methods (HPSGWO, PSO, FA, CSA, and GWO) is presented in two **Figure 4-13** and **Figure 4-14**. These results confirm the good performance of the proposed HPSGWO algorithm, as it contains higher SSIM, INM, and Q_{CB} values, that indicating better multi-modal registration results. The green and magenta color distribution show the information of the source image and sensed image, respectively. The difference between images before registration and Registered image confirms the recording effectiveness of the algorithms in general and the proposed algorithm in particular.

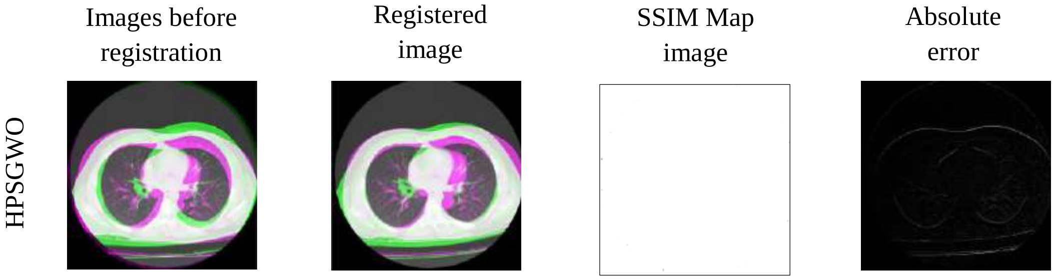

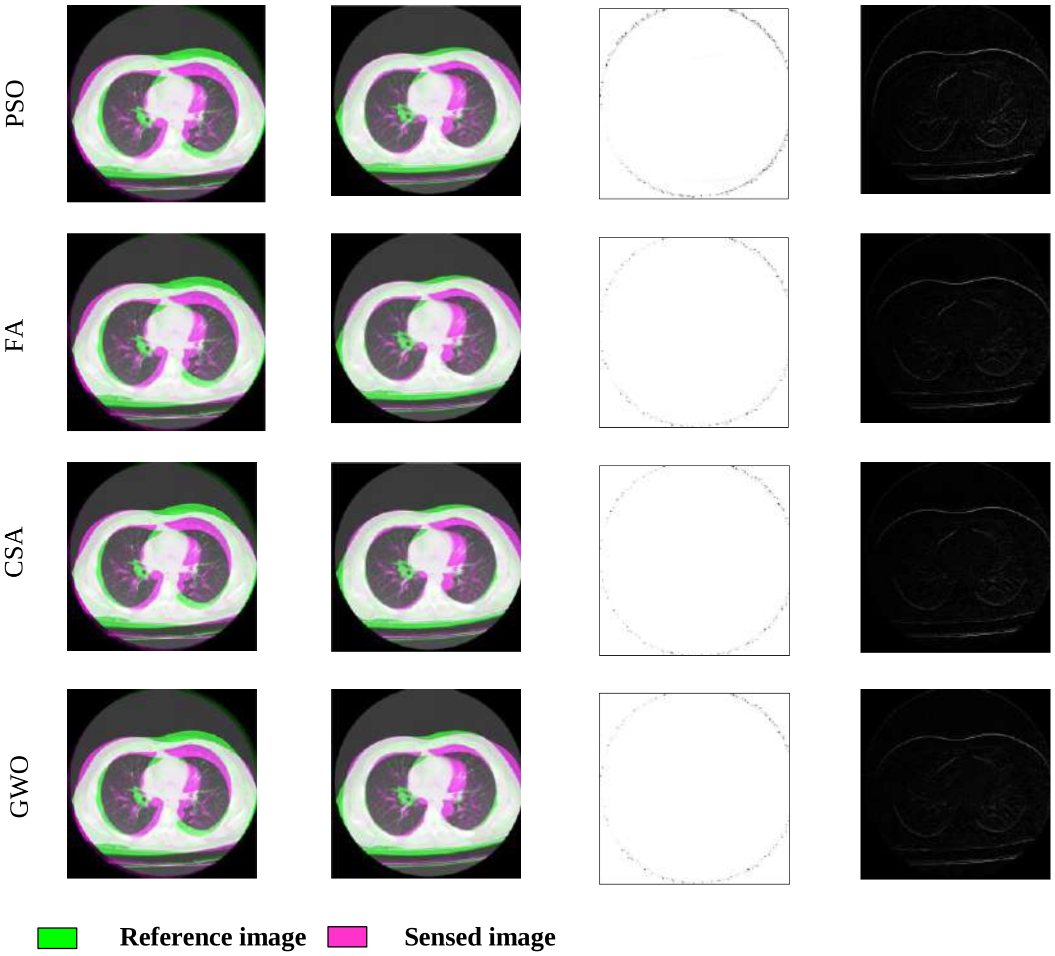

Figure 4-13 Visual results obtained from multi-modal image registration of pair (CT-I3/CT-I4) using the HPSGWO algorithm: (a) Images before registration, (b) Registered image, (c) SSIM Map image, and (d) Absolute error.

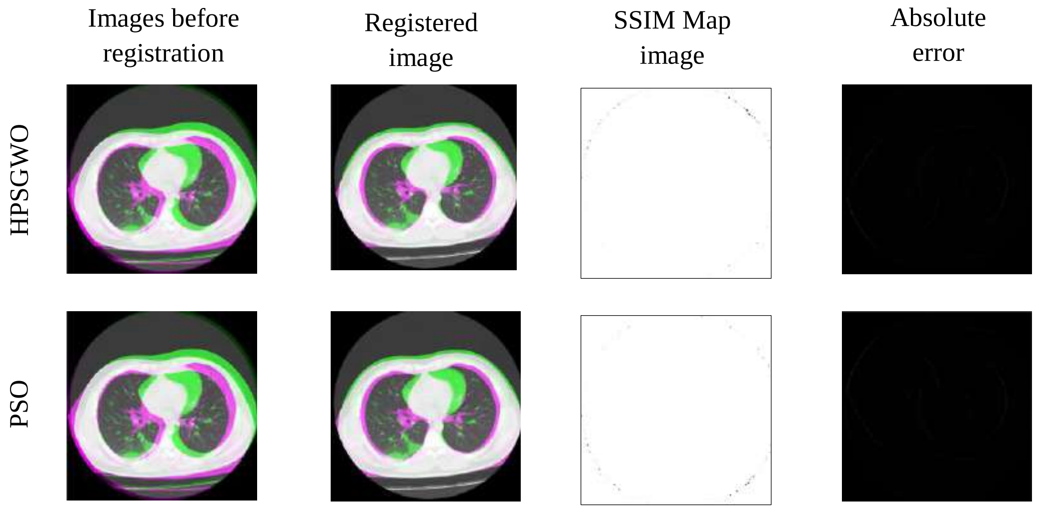

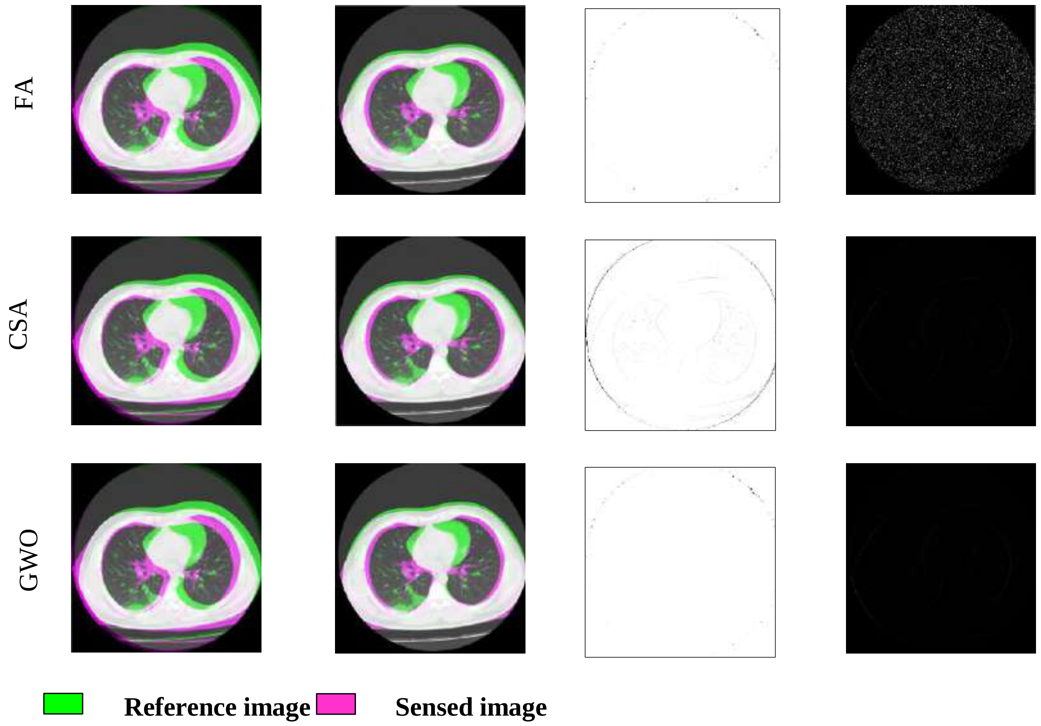

Figure 4-14 Visual results obtained from multi-modal image registration of pair (CT-I1/CT-I2) using the HPSGWO algorithm: (a) Images before registration, (b) Registered image, (c) SSIM Map image, and (d) Absolute error.

- A-frame has been added to the SSIM Map images to show their borders only, this frame does not belong to the resulting images.

Figure 4-15 shows the percentages of the algorithms used based on SSIM, which further illustrate the superiority of the proposed algorithm for multi-modal registration of the two image pairs.

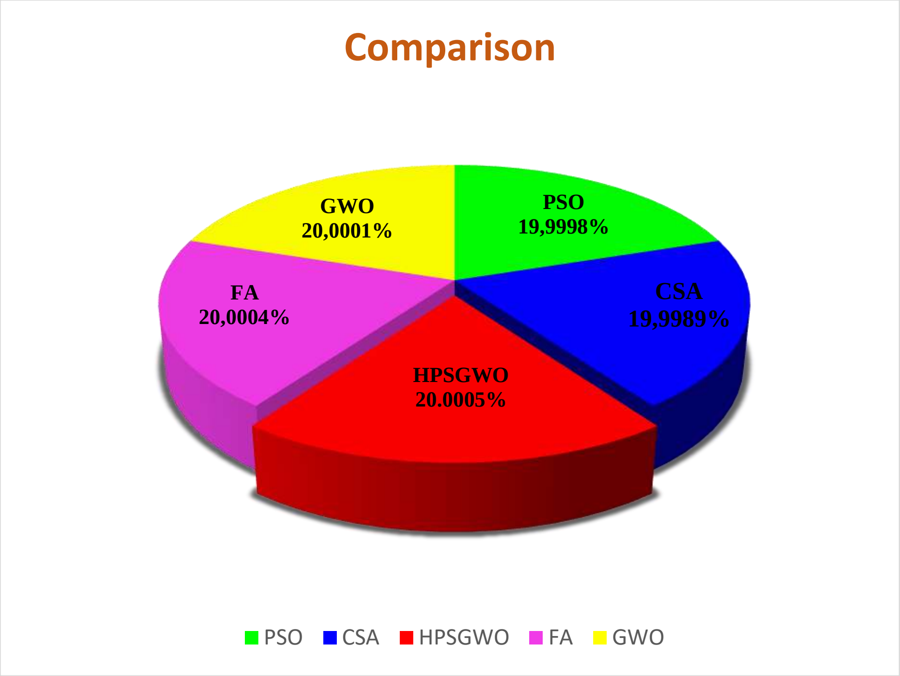

Figure 4-15 Multi-modal images Registration accuracy comparison of HPSGWO, PSO, GWO, FA, and CSA algorithms based on SSIM.

- **Comparisons with the latest deep learning methods**

To confirm the good performance of the proposed method for rigid registration of CT images of people infected with COVID-19 and to generalize their use, we compared them on the basis of the structural similarity metric (SSIM), Normalized Mutual Information (NMI), Human perception-based metric Q_{CB} and with the available method of registration based in deep learning. The same database used for deep learning-based registration was implemented in [92]. The following table shows the results obtained, to show the good performance of the proposed method. The following table shows the results obtained, that shows the superiority of the proposed method in the registration process.

Table 5-4 A comparative study of the proposed method with an existing method based on deep learning (deep convolutional inverse graphics network).

Dataset2						
Evaluaion	**PSO**	**GWO**	**FA**	**CSA**	**DCIGN**	**Proposed method**
SSIM	0.9997	0.9409	0.9996	0.9991	0.9700	**0.9998**
NMI	1.1843	1.1841	1.1843	1.1672	0.7400	**1.1844**

Q_{CB}	0.6689	0.6508	0.6508	0.6208	-	**0.6699**

4.4. Image registration of Computed Tomography of lung infected with COVID-19 using an improved sine cosine algorithm

4.4.1. Description of the Proposed Method

Generally, image registration is a process of aligning a pair of input images where a parametric transformation $\hat{T}$ is applied to the input image I_m to maximize its similarity with the reference image I_r [82]. After that, the similarity metric S is chosen to measure the similarity between these two pictures. Finally, an optimization technique is used to find the optimal transformation parameters minimizing the similarity measure [93].

In this section, we describe the proposed algorithm to register a pair of images. In the registration process, we define a spatial $\hat{T}$ which maximizes the structural similarity metric SSIM of the reference I_r and floating I_m images as:

$$\hat{T} = \mathrm{argmaxSSIM}\left[I_r(x,y), I_m(T(x,y))\right] \tag{4-4}$$

In this equation (x, y) is the coordinates of the image. The flowchart of our method is given in **Figure 4-16**.

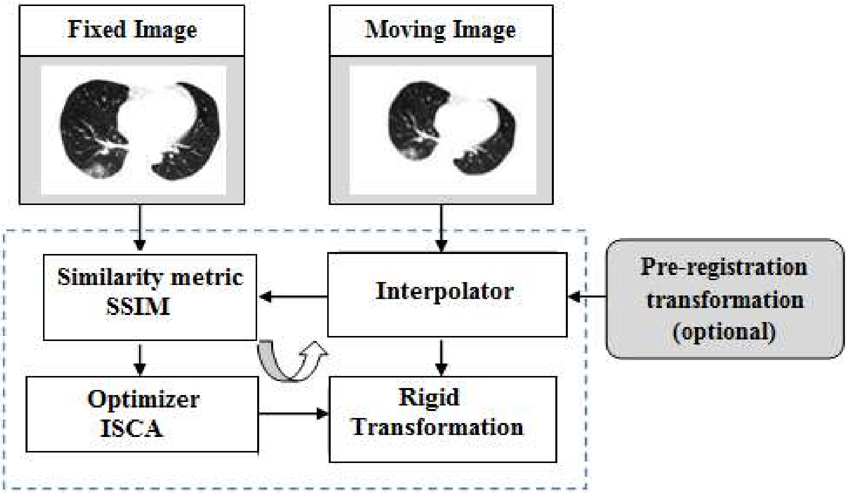

Figure 4-16 Block diagram of image registration process based on ISCA.

4.4.1.1. Transformation

The transformation model determines which geometrical transformation to apply for the registration. Our study is limited to the rigid transformation, which contains a translation along X and y axes t_x, t_y, and rotation θ, and it can be defined as [93]:

$$\hat{T} = \operatorname{argmax} SSIM\left[I_r(x,y), I_m(T(x,y))\right] \tag{4-5}$$

4.4.1.2. Similarity measure

In this paper, we use the Structural Similarity Index Metric (SSIM) to evaluate the similarity between the reference image and floating source image instead of the Normalized Mutual Information (NMI) criterion [94]. The structural similarity metric (SSIM) is given by [26]:

$$SSIM\left(I_r,\ I_{m_{reg}}\right) = \frac{\left(2\mu_r\mu_{m_{reg}} + (k_1L)^2\right)\left(2\sigma_{r,m_{reg}} + (k_2L)^2\right)}{\left(\mu_r{}^2 + \mu_{m_{reg}}^2 + (k_1L)^2\right)\left(\sigma_r{}^2 + \sigma_{m_{reg}}^2 + (k_2L)^2\right)} \tag{4-6}$$

Where μ_r and σ_r denote the local mean and standard deviation of reference image I_r, μ_{m_reg} and σ_{m_reg} denote the local mean and standard deviation of registered image I_{m_reg}, σ_{m_reg} is cross-covariance for the reference image I_r and registered image I_{m_reg}. k_1, k_2 are parameters with small values and L is the maximum pixel value. SSIM values have the range of $[0,1]$.

4.4.1.3. Optimization algorithm

Optimization is the most important stage in the image recording process as optimization techniques are used to find the optimum transformation parameters needed to align the images. Optimization algorithms are the primary source that influences the convergence speed of a similarity measure [95] [96].

- **Sine Cosine algorithm (SCA)**

The sine cosine algorithm proposed by Mirjalili [80] is a population-based optimization technique. It begins by generating a set of random solutions, and then, these solutions are updated based on the sine or cosine function as in equation 4-7.

$$X_i^{t+1} = \begin{cases} X_i^t + r_1.\sin(r_2).\left|r_3 P_i^t - X_i^t\right|, & r_4 < 0.5 \\ X_i^t + r_1.\cos(r_2).\left|r_3 P_i^t - X_i^t\right|, & r_4 < 0.5 \end{cases} \tag{4-7}$$

Where P_i^t is the position of the destination point in i-th dimension at iteration t, X_i^t is the position of current solution in i-th dimension. r_1, r_2, r_3 and r_4 are random variables and are uniformly distributed between 0 and 2π, 0 and 2, and between 0 and 1 respectively. The random variable r_1 is responsible for the area of the next solution, which can be either in the space between the solution and the destination or outside it. The variable r_1 is updated as:

$$r_1 = a\left(1 - \frac{t}{T_{max}}\right) \tag{4-8}$$

Where a is a constant, T_{max} is the maximum iterations. The sine cosine algorithm is summarized as follows [80].

Algorithm 1: Sine Cosine Algorithm

```
Initialize a set of random solutions $X$
Calculate the objective function of each solution.
Select the best solution that optimizes the objective function.
Initialize the parameters $r_i$ where $i = 1:4$ .
Initialize the generation count $t = 0$.
While $t < T_{max}$
    For each candidate solution
     Update the solution using Eq. 4-7
     Calculate the objective function of updated solution
         Update the best solution.
         End for
    Update $r_i$ where $i = 1:4$.
    $t = t + 1$
```

```
End while
Return the best solution obtained so far as the global optimum.
```

- **Improved SCA**

As mentioned above, the SCA does not always converge to the global solution. To overcome this drawback, the SCA should be improved. In this paper, we propose to hybridize the SCA with the PSO algorithm by choosing between SCA and PSO updating procedures. The updating rule of the Improved SCA (ISCA) is as follows:

$$x_i^{t+1} = \begin{cases} x_i^t + r_1 \, . \sin(r_2).\left|r_3 g^t - x_i^t\right|, & r_4 < 0.4 \\ x_i^t + r_1 \, . \cos(r_2).\left|r_3 g^t - x_i^t\right|, 0.4 \geq & r_4 > 0.6 \\ x_i^t + v_i^{t+1}; & r_4 \geq 0.6 \end{cases} \tag{4-9}$$

$$\mathrm{v}_\mathrm{i}^{\mathrm{t}+1} = \mathrm{v}_\mathrm{i}^\mathrm{t} + \mathrm{r}_5\mathrm{c}_1\left(\mathrm{p}_\mathrm{i}^\mathrm{t} - \mathrm{x}_\mathrm{i}^\mathrm{t}\right) + \mathrm{r}_6\mathrm{c}_2\left(\mathrm{g}^\mathrm{t} - \mathrm{x}_\mathrm{i}^\mathrm{t}\right) \tag{4-10}$$

Where $\mathrm{p}_\mathrm{i}^\mathrm{t}$ is the best position of the solution i, and g^t is the global best position found by all solutions [21]. The acceleration constants C_1 and C_2 have real value, usually in the range $0 \leq \mathrm{C}_1$ and $\mathrm{C}_2 \leq 4$. The values r_5 and r_6 are uniformly distributed in the range [0,1]. The Improved SCA is summarized as follows:

Algorithm 2: ISCA Algorithm

```
Initialize $x_i^0 \; \forall i \in 1:N$
Initialize the solutions 's best position to its initial position $p_i^0$.
Calculate the objective function of each solution.
.Select the best solution that optimizes the objective function.
Initialize the parameters $c_1, c_2$ and $r_i$ where $i = 1:6$.
Initialize the generation count $= 0$.
While $t < T_{max}$
    For each candidate solution
        Update the solution using Eqs. (4-9 and 4-10)
```

```
        Calculate the objective function of updated solution.
            Update the best solution $p_i^t$.
            End for
        Update the global best position $g^t$.
    Update $r_i$ where $i = 1:6$.
    $t = t + 1$
    End while
    Return the best solution obtained so far as the global optimum.
```

4.4.2. Computer simulation

Several simulations were performed on images of the lungs of people infected with the COVID-19 using the SCA algorithm and ISCA to obtain good registering of these images.

4.4.2.1. Accuracy

In the experiment three images were randomly chosen from the AJR dataset. A floating image (test) is obtained by applying the translation $\left(t_x^*, t_y^*\right) = (5, -5)$ and, a rotation of $\theta^* = 5°$ to the ground truth image. **Figure 4-17** and **Figure 4-18** show ground truth images and the superposing of the test and the reference images. The grey areas correspond to areas that the two images have similar intensities, while magenta and green areas show regions where one image is brighter than the other.

Bio-inspired algorithms SCA and ISCA have been used to register the images. The used parameters are generated by the trial-and-error method. They are illustrated in table 4-5.

Table 4-6 SCA and ISCA parameters values

Parameter	N	$T_{\max}$	c_1	c_2	a	k_1	k_2	L
value	25	80	2.05	2.05	2	0.03	0.05	255

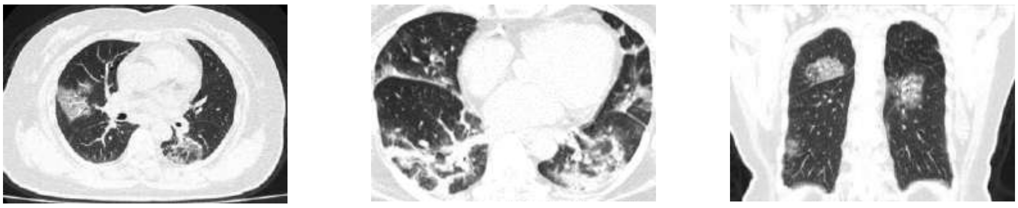

(a). CT image 1 (b). CT image (c). CT image 3

Figure 4-17 CT images of the lungs of a patient infected with the COVID-19.

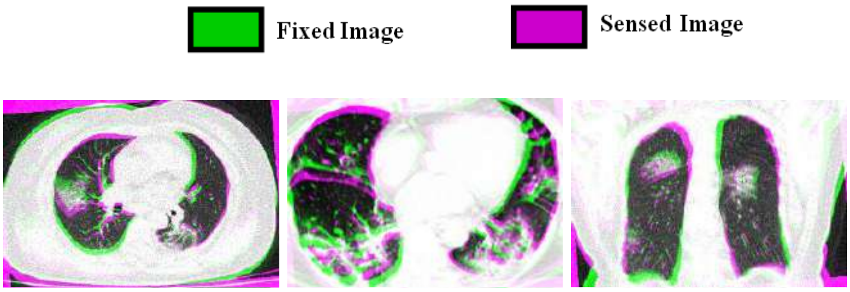

(a). CT image 1 (b). CT image 2 (c). CT image 3

Figure 4-18 Superposing of the test and the reference images.

After applying the SCA and ISCA algorithms, the results were recorded and compared to determine the best algorithm that helps us obtain a helpful image in diagnosing COVID-19. From the results obtained after applying the two algorithms to the images of the lungs with COVID-19 that appear in Table 4-6, we found that the results obtained from the ISCA are more accurate than those obtained by the SCA. The SSIM and DSC values from the ISCA are higher than those obtained with the SCA for the three images, while the MSE values for ISCA are smaller, which proves that the two images are well-aligned using the ISCA.

Table 4-6 Performances of SCA and ISCA for AJR dataset.

Image	Algorithm	t_x	t_y	θ	SSIM	MSE	DSC
CT1	SCA	5.2290	-5.0378	4.9761	0.9475	0.0355	0.9895
	ISCA	4.9951	-4.9934	5.0647	0.9692	0.0350	0.9931
CT2	SCA	5.0862	-4.8011	4.7601	0.9652	0.0015	0.9062
	ISCA	5.0001	-4.9827	5.1427	0.9890	0.0012	0.9606
CT3	SCA	5.2666	-5.0799	5.1909	0.9442	0.0116	0.9513
	ISCA	4.9653	-5.0042	4.9911	0.9885	0.0112	0.9794

From the absolute error shown in **Figure 4-19**, the transformation parameters obtained by the ISCA algorithm are more accurate than those obtained with the SCA. **Figure 4-20** shows the affinity curves after applying the algorithms to the tree target images in this paper. As we can see, the ISCA is faster and more accurate compared to the SCA algorithm. Through these curves, we note that the SCA accuracy never reaches that of the ISCA up to 80 iterations. This confirms the efficiency of the ISCA algorithm for these used images.

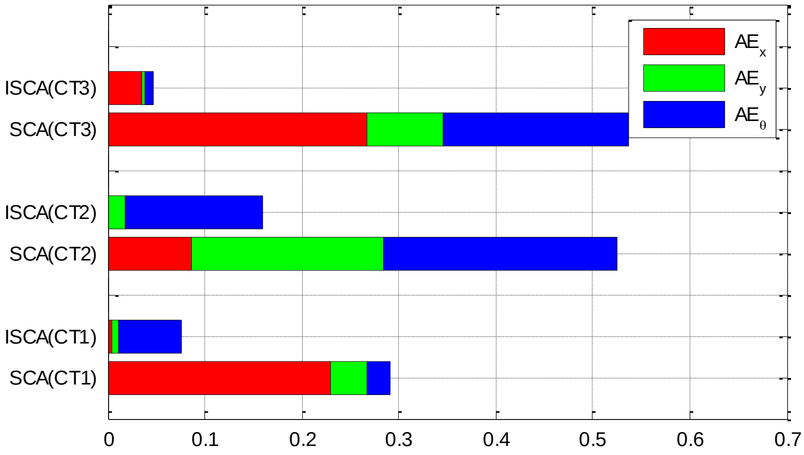

Figure 4-19 Absolute error of the transformation for three CT images from AJR dataset.

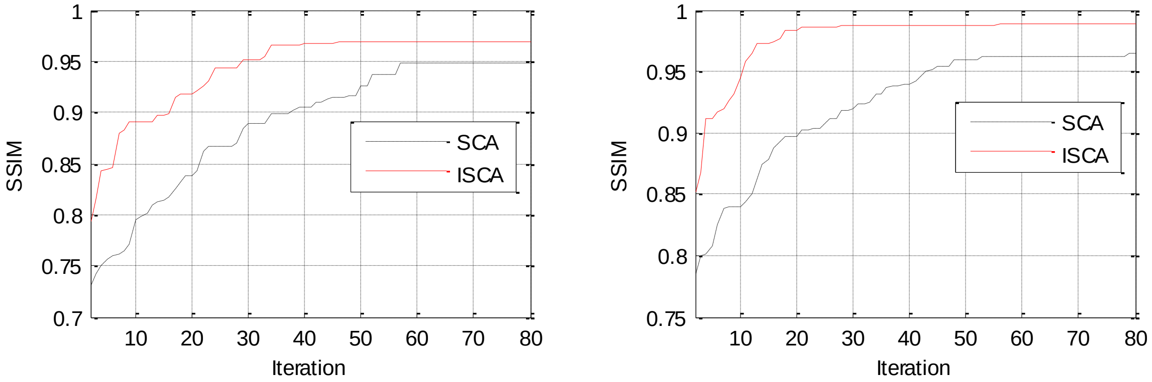

(a). CT image 1 (b). CT image 2

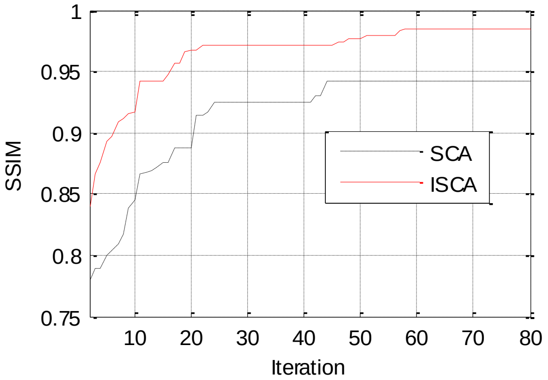

(c).CT image 3

Figure 4-20 Convergence curves for CT images registration using SSIM for AJR dataset.

Figure 4-21 shows the visual results of registering the three images using the ISCA and the SCA. The absolute error map and the SSIM map justify a good alignment of the test and reference images since white regions, which correspond to high values of the SSIM, indicate a good alignment of the two images.

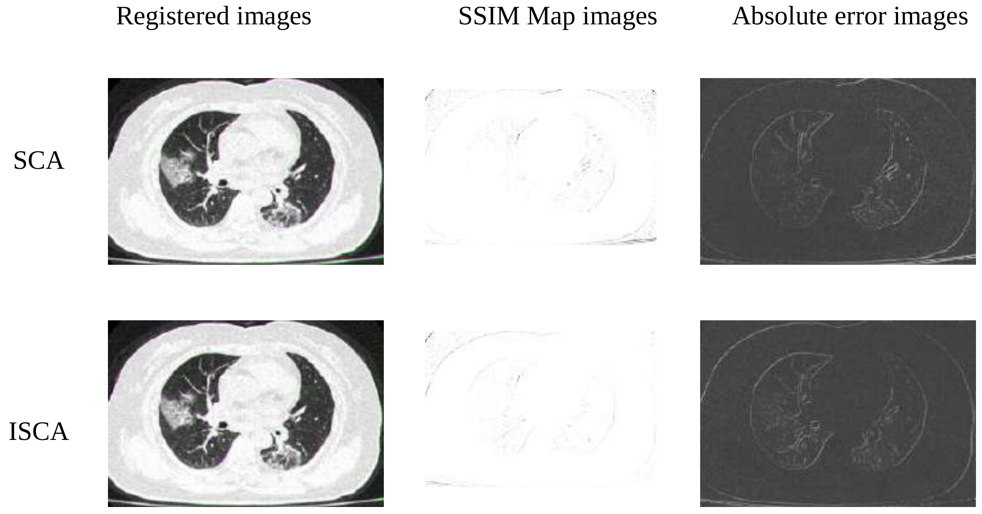

Image 5

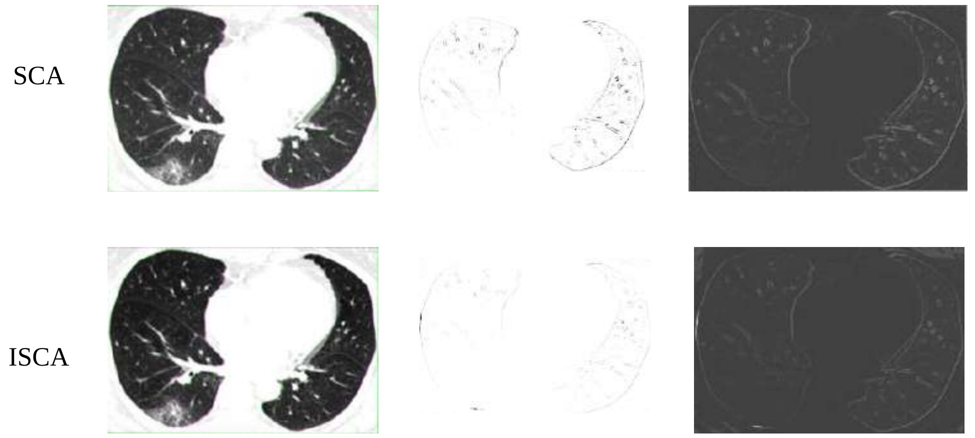

Image 7

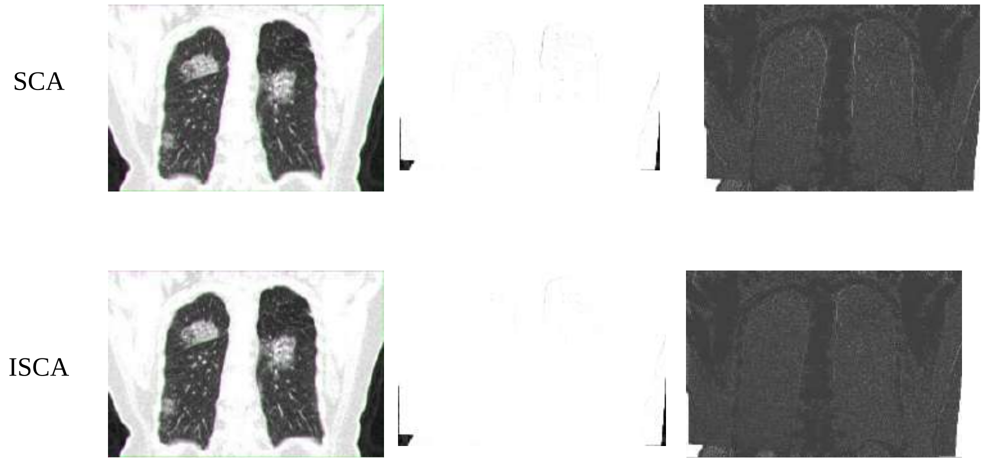

Image 10

Figure 4-21 Visual registration results for three CT images from AJR dataset.

To justify the generalization ability of the proposed method, we carried out experiments using another COVID-19 CT database. The COVID-CT-Dataset consists of 349 CT images from 216 patients with the coronavirus. It is publicly available at [97]. **Figure 4-22** shows some image samples randomly chosen from this dataset. These CT images have different sizes. The minimum, average, and maximum height are 153, 491, and 1853. The minimum, average, and maximum width are 124, 383, and 1485.

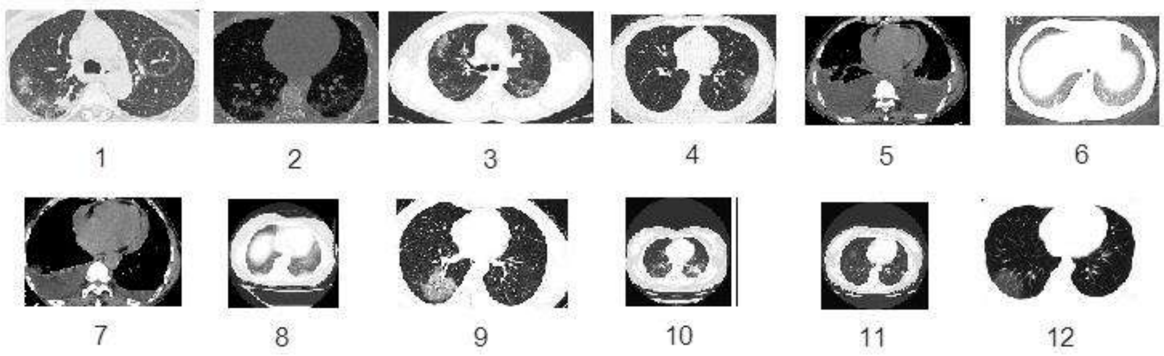

Figure 4-22 Illustration of twelve CT images from the COVID-CT dataset.

In the first simulation, the SCA and ISCA were applied on 12 image samples after having undergone random transformations. **Figure 4-23** shows the absolute error of the transformation parameters, while **Figure 4-24** shows the mean values of the similarity metric, DSC metric and the mean square error. Through the similarity curves of the SSIM and DSC, the ISC algorithm outperformed SCA for all used images. For the absolute error, the ISC algorithm outperformed the SC algorithm in most cases. We can show that the values are close together for the absolute error in the horizontal direction in image 6, the rotation absolute error in image 5. According to these results, we can conclude that the proposed method can perform better.

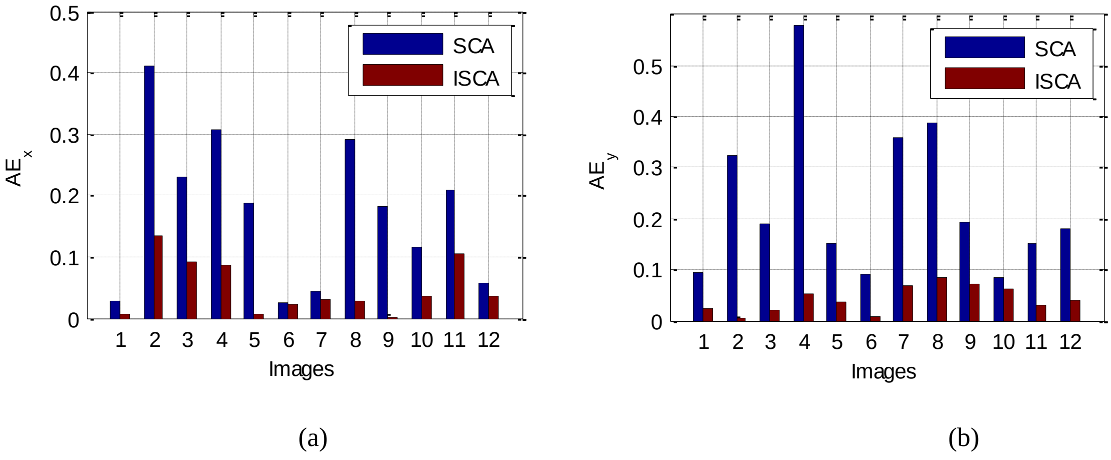

(a) (b)

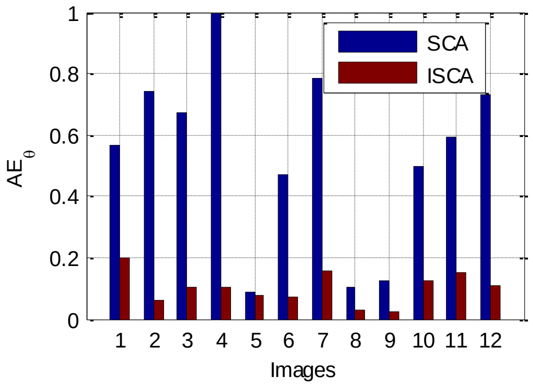

(c)

Figure 4-23 Absolute error in (a) the horizontal direction, (b) the vertical direction, (c) rotation angle for the COVID-CT dataset.

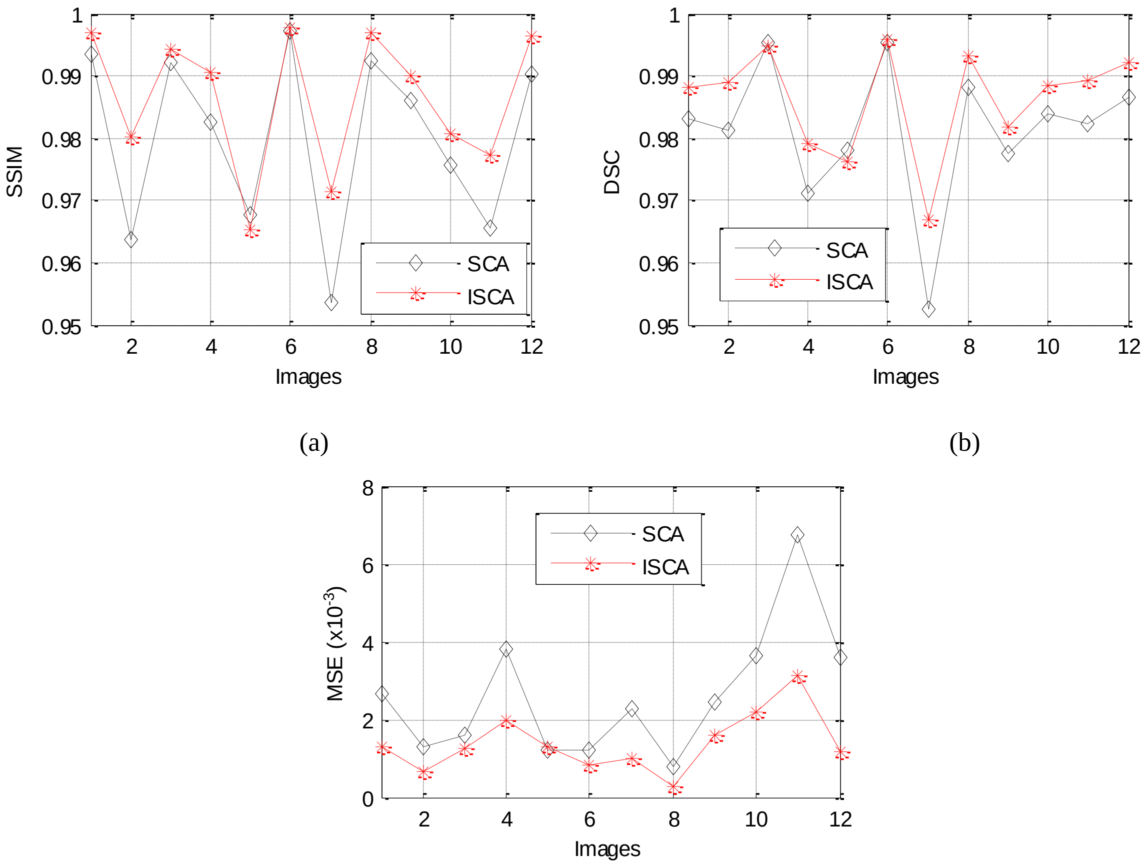

(a) (b)

(c)

Figure 4-24 Registration results for the COVID-CT-Dataset. (a) SSIM curve, (b) MSE curve, (c) DSC curve.

To check the robustness of the proposed algorithm, we have used the whole images of the dataset. As shown in the **Figure 4-25**, the SSIM values after convergence of the ISCA are closer on 1 than the SCA. The mean and the standard deviation (STD) values of the SSIM, DSC, MSE and the absolute error of the transformation parameters AE_x, AE_y and AE_θ were reported in table 4-7. As we can see, the ISCA outperforms the SCA for all metrics.

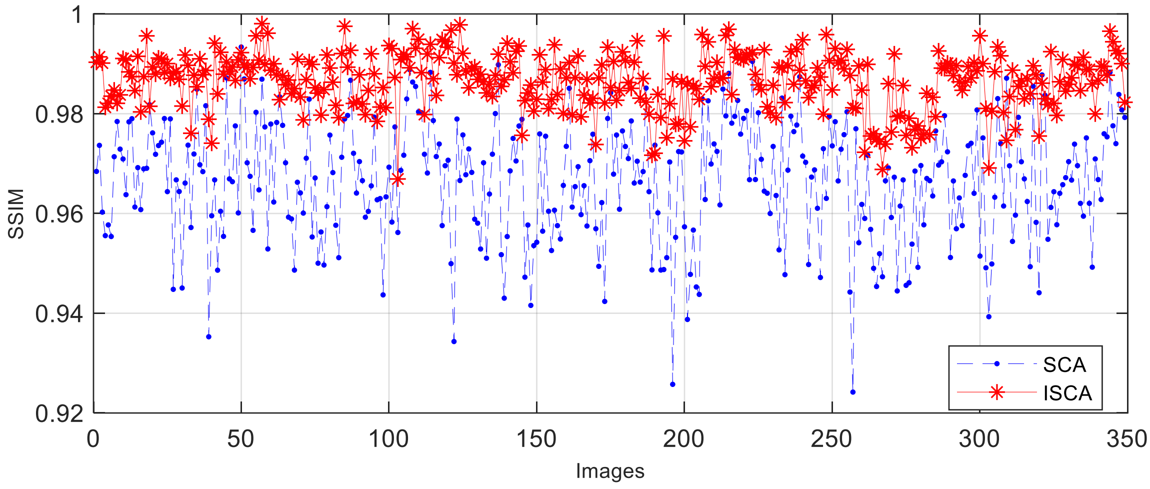

Figure 4-25 SSIM values of SCA and ISCA after convergence for COVID-CT images.

Table 4-7 Statistical analysis of SCA and ISCA for the COVID-CT dataset

	Algorithm	Mean ±STD	Algorithm		Mean ±STD
MSE	SCA	0.0093±0.0043	SCA	AE_x	0.1856±0.1562
	ISCA	**0.0080±0.0025**		AE_y	0.1610± 0.1313
DSC	SCA	0.9575±0.0559		AE_θ	0.3128±0.2411
	ISCA	**0.9600±0.0294**	ISCA	AE_x	**0.0705± 0.0625**
SSIM	SCA	0.9666±0.0121		AE_y	**0.0539±0.0451**
	ISCA	**0.9865±0.0057**		AE_θ	**0.1448±0.1250**

4.4.2.2. Additional simulation on microscopic images

COVID-19 can progress to severe acute respiratory syndrome with pneumonia and acute respiratory distress syndrome. Histologically, this disease causes diffuse alveolar damage corresponding to the phase of the disease. There are three lung injury patterns: epithelial, which are diffuse alveolar damage with varying degrees of organization, denudation, and hyperplasia of pneumocytes, vascular, diffuse intra-alveolar fibrin, microvascular injury, (micro) thrombi, acute fibrinous, and organizing pneumonia and fibrotic which is diffuse alveolar damage, interstitial fibrosis [98]. **Figure 4-26** shows the all images of lung injury patterns.

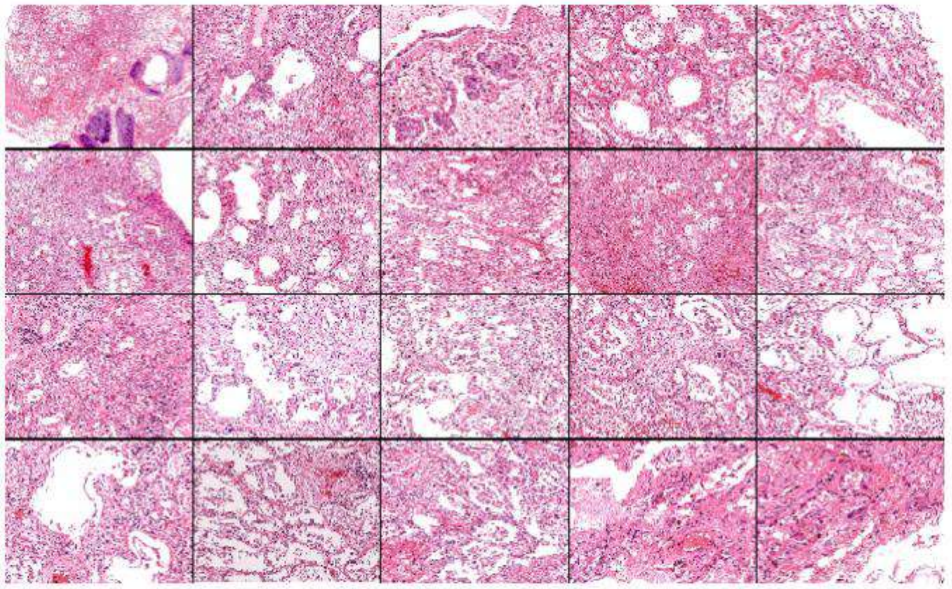

Figure 4-26 Microscopy images of histopathology tissue samples of lung infected by COVID-19.

We will now apply the two methods on the all images after undergoing random rigid geometric transformations as we did for the previous simulations. **Figure 4-27** shows the absolute error between the true and the estimated rigid transformation parameters. We can see that the ISCA has a minimum error for most images. Even if there is an underestimation of one of the three parameters, this does not affect the similarity criteria. We can see in **Figure 4-28** that the ISCA remains better compared to the SCA. The table 4-8 resume the mean and the standard deviation values of the SSIM, DSC, MSE and the absolute error of the transformation parameters AE_x , AE_θ , AE_θ . As we can see, the ISCA outperforms the SCA for all metrics as in the case of CT images.

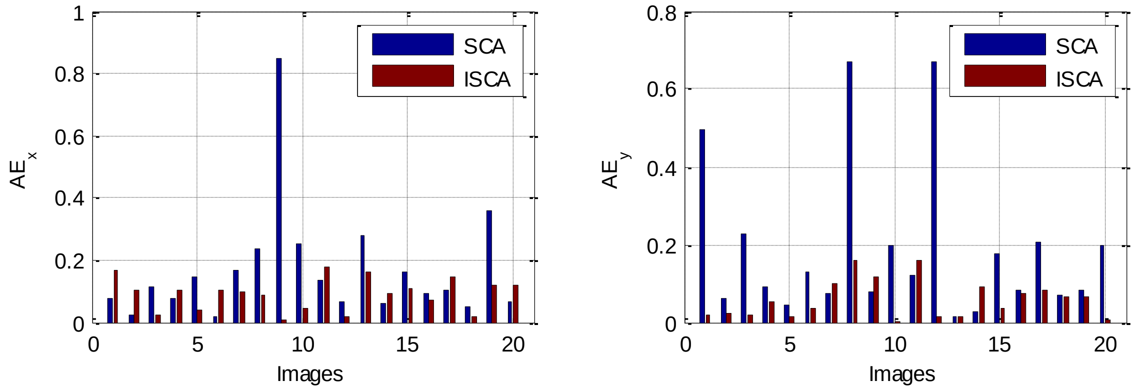

(a) (b)

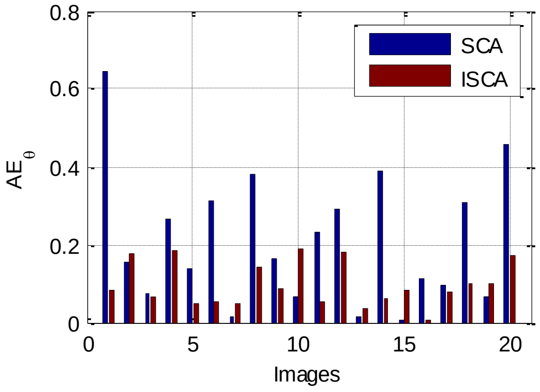

(c)

Figure 4-27 Absolute error for microscopy images (a) the horizontal direction, (b) the vertical direction, (c) rotation angle.

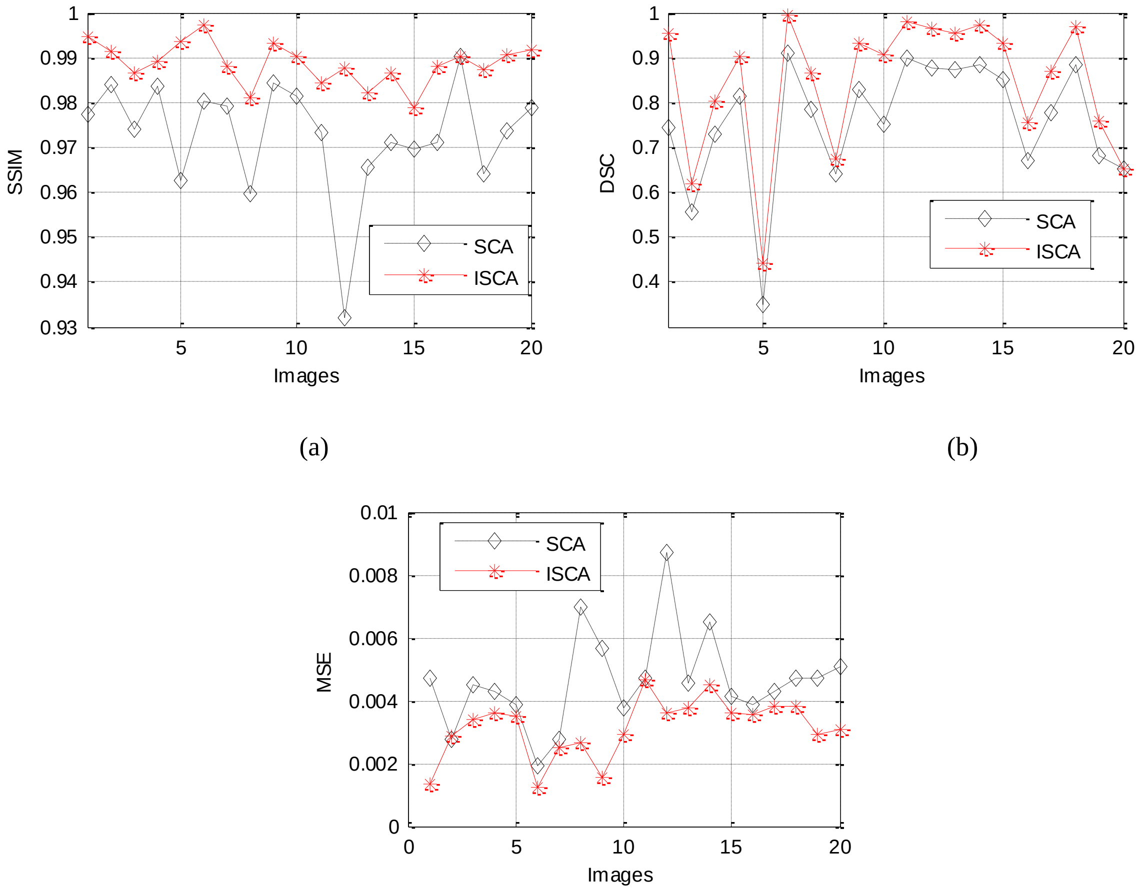

(a) (b)

(c)

Figure 4-28 Quantitative registration results for microscopy images: (a) SSIM curve, (b) DSC curve, (c) MSE curve.

Table 4-8 Statistical analysis of SCA and ISCA for COVID19 microscopy images.

	Algorithm	Mean ±STD	Algorithm		Mean ±STD
MSE	SCA	0.0046±0.0015	SCA	AE_x	0.1664 ±0.1840
	ISCA	**0.0032±0.0009**		AE_y	0.1859 ±0.1967
DSC	SCA	0.8898± 0.0776		AE_θ	0.2095±0.1706
	ISCA	**0.9066± 0.0769**	ISCA	AE_x	**0.0912 ±0.0520**
SSIM	SCA	0.9728 ± 0.0126		AE_y	**0.0577 ±0.0482**
	ISCA	**0.9886± 0.0046**		AE_θ	**0.0976±0.0568**

In the same way, three images with epithelial, vascular and fibrotic lung injury patterns, as shown in **Figure 4-29**, were chosen for the visual investigation. From **Figure 4-30**, we can see almost no effects of misregistration for the ISCA. The SSIM map image is whiter, and the absolute error image is blacker. While for the SCA, some misregistrations are visible in the registered images

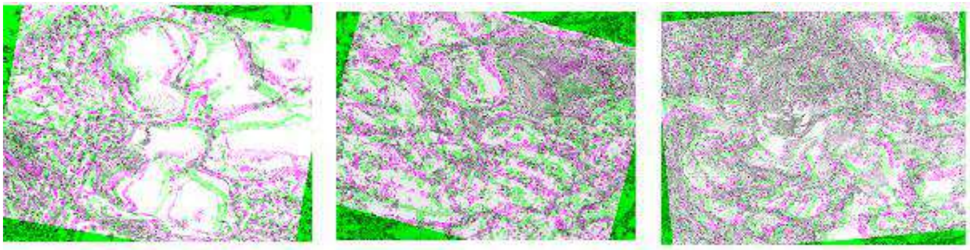

Epithelial Vascular Fibrotic

Figure 4-29 Input microscopy images for registration.

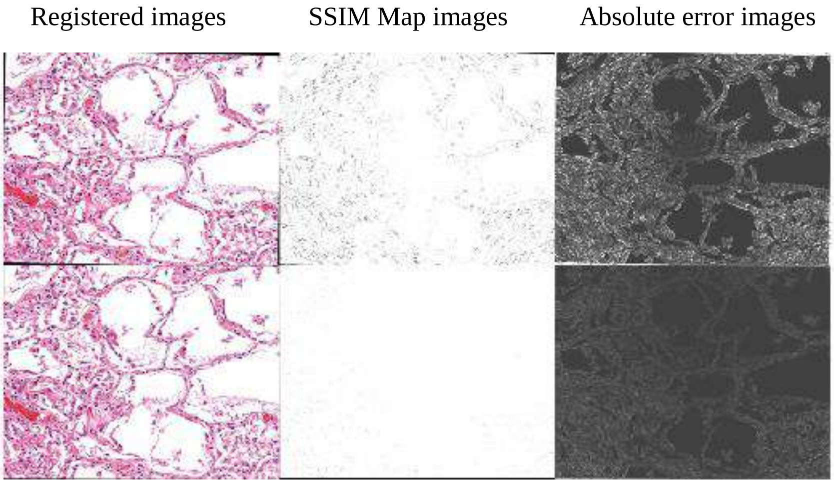

Epithelial lung injury patterns

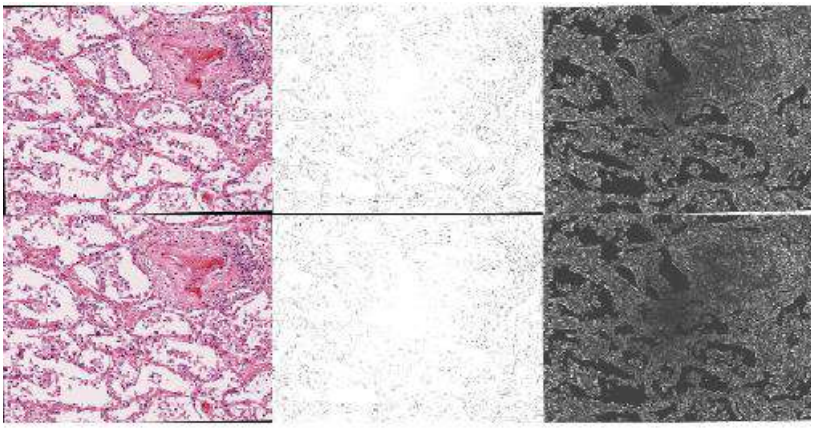

Vascular Epithelial lung injury patterns

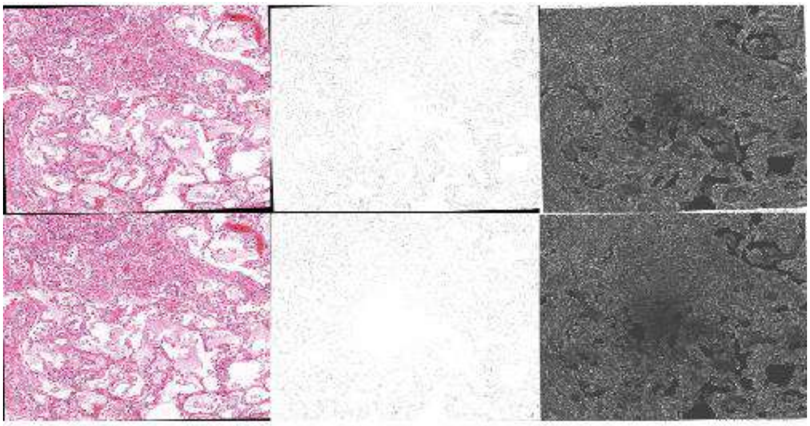

Fibrotic Epithelial lung injury patterns

Figure 4-30 Registration results on COVID19 microscopy images.

4.4.2.3. Comparisons with state-of-the-art algorithms

It is more judicious to compare the proposed method with other methods using the same images test to make a meaningful comparison. To our knowledge, there is no work related to covid-19 images registration, was performed until writing this paper. So, we have compared our method with the other methods based on self-adapting pulse-coupled neural networks (SAPCNN) [99] and mutual information using particle swarm optimization (MI- PSO) [100] [101], which have been applied to register other medical images from the Whole Brain database. It is a popular database in medical images registration. It provides thousands of images from Harvard Medical University that deal with human brain tumors. This database is publicly available at (http://www.med.harvard.edu/AANLIB/). Through Table 4-9, we can see that the proposed method can achieve good accuracy and outperforms the two state-of-the-art methods used in this comparison.

Table 4-9 Comparative analysis between the proposed method against some existing work.

Group	Method	t_x	t_y	θ	AE_x	AE_y	AE_θ
Group 1	Ground truth	0	0	10	-	-	-
	MI-PSO [100]	-0.1752	-0.0208	10.0103	0.1752	0.0208	0.0103
	SAPCNN [99]	-0.1695	0.0209	10.0081	0.1695	0.0209	0.0081
	SCA	-0.1191	-0.0281	9.9885	0.1191	0.0281	0.0115
	ISCA	-0.0103	-0.0012	9.9945	0.0103	0.0012	0.0055
Group 2	Ground truth	5	5	5	-	-	-
	MI-PSO[100]	4.8675	4.9394	5.1008	0.1325	0.0606	0.1008
	SAPCNN[99]	4.8787	4.9503	5.0130	0,1213	0,0497	0.0130
	SCA	5.0590	4.9737	5.0252	0.0590	0.0263	0.0251
	ISCA	4.9577	5.0008	5.0107	0.0423	0.0008	0.0107
Group 3	Ground truth	5	10	10	-	-	-
	MI-PSO[100]	4.8473	10.4260	10.5277	0.1527	0.4260	0.5277
	SAPCNN[99]	4.8317	9.9812	10.0083	0,1683	0,0188	0.0083
	SCA	4.5925	10.2868	9.9614	0.4075	0.2868	0.0386
	ISCA	5.0687	9.9958	10.0309	0.0687	0.0042	0.0309
Group 4	Ground truth	10	10	20	-	-	-
	MI-PSO[100]	9.7456	10.0280	20.1030	0.2544	0.0280	0.1030
	SAPCNN[99]	9.9763	10.0302	19.9891	0.0237	0.0302	0.0109

	SCA	9.9968	10.1192	20.0853	0.0032	0.1192	0.0853
	ISCA	10.0633	9.9723	19.9931	0.0633	0.0277	0.0069

4.5. Conclusion

In this chapter, meta-heuristic algorithms have been successfully applied to medical image registration. We have firstly started by applying GWO, SCA and PSO meta-heuristic algorithms individually for CT and MRI image registration and comparing the results obtained. Then, the HPSGWO and ISCA algorithms were developed and used to register CT images of the lungs infected with COVID-19. This process provides images that facilitate the diagnosis of this disease by showing the spread of ground glass opacity in CT images.

After conducting several experiments and applied the proposed approaches to various databases, the reported results prove several facts. First, the GWO, SCA and PSO algorithms were successfully used in medical image registration and show the superiority of the gray wolves algorithm in recording CT and MRI images over other algorithms on the other hand. Second, the efficiency of the two developed algorithms HPSGWO and ISCA has been clearly shown in the CT image registration of the lung infected with COVID-19. The qualitative and quantitative results of these two new approaches showed high accuracy and speed in the registration process.

CHAPTER 5 MULTI MODAL IMAGE FUSION RESULTS OF: MULTI FOCUS IMAGES AND MEDICAL IMAGES

5.1. Introduction

As we have previously explained, image fusion is an important technique to provide an image that contains sufficient information for the analysis process. This image is used in various fields, especially the medical aspect. A radiologist in the medical field needs an image that contains the information in two or more imaging techniques to facilitate the diagnosis process. Moreover, the image fusion was the perfect solution to overcome the defects caused by the imaging sensors by detecting the focus region and then fusion the images. Despite the great development witnessed by the methods of decomposing images, their results remain unsatisfactory due to the distortions that appear in the fused image.

In the rest of this chapter, we present our methods for multi-focus image fusion and medical images, respectively. The first method relies mainly on multi-focus image fusion based on focus region detection and fast guided filter to provide a clear image free of blurry areas. The proposed method for merging multi focus images is compared with different fusion methods for this type of image. Methods for comparison from different categories were selected in order to confirm the results obtained by the proposed method, where PCA, IFGD, and WSSM were used from the transform domain category, ICA, GIF and MSMFM from the spatial domain category, and CNN from the Deep learning category. Our second proposed method based in multi-scale Alternative approach to cross bilateral filter for multi-modal medical image fusion. To achieve an efficient fusion process based on the proposed method, meta-heuristic algorithms we use to obtain suitable input parameters.

5.2. Multi-focus image fusion based on focus region detection and fast guided filter

5.2.1. Proposed method

The essential concept of the proposed method is to detect focus region for multi-focus image fusion using a fast guided filter named (named FGFDF). It is shown by the diagram in **Figure 5-1** that the proposed method includes six steps.

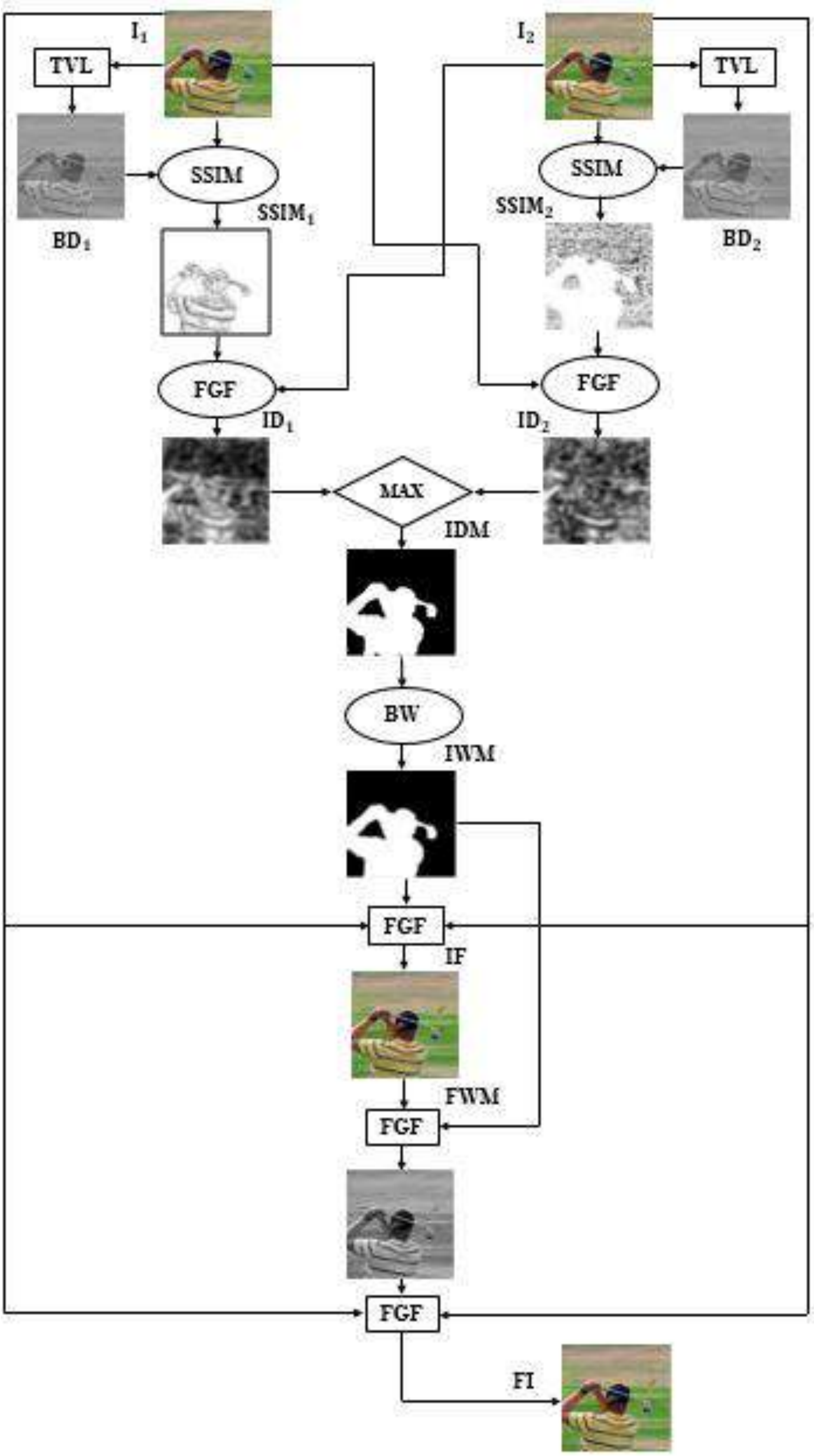

Figure 5-1 Schematic diagram of the proposed multi-focus image fusion method, where: I_1 and I_2, TVL: Total variation regularization, SSIM: Structural Similarity, IDM: Initial Decision Map, IWM: Initial Weights Map, IF: Initial Fusion, FWM: Final Weights Map, FI: Fused Image and BD: Base Layers Detection

Firstly, Total variation regularization (TVL) is relied upon to remove noise and distortion in the source image. This process results in obtaining the base layer as a prelude to the SSIM implementation. Secondly, the contrast image between the source image and base layers detection (BD) is extracted by Structural SIMilarity (SSIM) as a second stage for this method. After that, the Initial Detection (ID) is done using the fast guided filter. Thirdly, the focus scale is determined that show the maximum for best-focused image, as it is inversely proportional to the defocus area. In the field of multi-focus image fusion, it is necessary that the focus areas of the source images produce the maximum of the focus scale, while the regions of defocus produce the minimum of this scale. Depending on the initial detection ID1 and ID2 of the two source images of the focus areas and by taking the maximum base in terms of pixels, the Initial Detection Map (IDM) is obtained as shown in the equation 5-5. Fourth, the BWAREAOPEN instruction is applied to obtain the Initial Weights Map IWM, which is to filter the IDM from noise and interference. Again, depending on the fast guided filter, through the source images and IWM, the initial fusion process is performed to obtain the initial fused image. Carried out and the final fused image FI is obtained.

5.2.1.1. Total variation regularization

As a first step, the total variation regularization (TVL) is applied to the two source images for obtaining base layers B1 and B2. Where TVL works to preserve the edges and restore the image by removing the noise and smaller-scaled noise while preserving the larger features essentially in source images [104] as shown in **Figure 5-2** -(c). The following equation shows the regulation of total variance:

$$B1 = \left\| f_{TV} \right\| = \sqrt{\beta_x^2 \left[D_x f \right]_i^2 + \beta_y^2 \left[D_y f \right]_i^2} \tag{5-1}$$

$$B2 = \left\| f_{TV} \right\| = \sqrt{\beta_x^2 \left[D_x f \right]_i^2 + \beta_y^2 \left[D_y f \right]_i^2} \tag{5-2}$$

Where $\left[f \right]_i$ and D_y are the forward finite difference operators along the horizontal and vertical, respectively. Here, (β_x, β_y) are constants, and $\left[f \right]_i$ represent i-th component of the vector f.

5.2.1.2. Structural similarity

SSIM shows the degree of similarity between two source images A and B by modeling any image distortion as a combination of three factors that are loss of correlation, luminance distortion and contrast distortion [105]. This step helps to the initial detection of focus to source images based on the fast guided filter. The structural similarity can be defined as:

$$\mathrm{SSIM}(\mathrm{A},\mathrm{B}) = \mathrm{l}(\mathrm{A},\ \mathrm{B})\mathrm{c}(\mathrm{A},\mathrm{B})\mathrm{s}(\mathrm{A},\mathrm{B}) \tag{5-3}$$

Where:

$$\begin{cases} l\left(\mathrm{x},\ \mathrm{y}\right) = \dfrac{2\mu_{\mathrm{x}} 2\mu_{\mathrm{y}} + \mathrm{C}_1}{\mu_{\mathrm{x}}^2 + \mu_{\mathrm{y}}^2 + \mathrm{C}_1} \\ c\left(\mathrm{x},\ \mathrm{y}\right) = \dfrac{2\sigma_{\mathrm{x}} 2\sigma_{\mathrm{y}} + \mathrm{C}_2}{\sigma_{\mathrm{x}}^2 + \sigma_{\mathrm{y}}^2 + \mathrm{C}_2} \\ s\left(\mathrm{x},\ \mathrm{y}\right) = \dfrac{\sigma_{\mathrm{xy}} + \mathrm{C}_3}{\sigma_{\mathrm{x}}\sigma_{\mathrm{y}} + \mathrm{C}_3} \end{cases} \tag{5-4}$$

Here σ_{A} and σ_{B} are the cross-covariance for images A and B or mean luminance. μ_{A} and μ_{B} represent the standard deviations between the two image A and B**.**

5.2.1.3. Initial decision map

After the images are fused by the fast guided filter, an initial decision map is produced by taking the maximum pixel base of the filtered images. Equation 5-5 shows how to obtain IDM:

$$\mathrm{IDM}(\mathrm{x},\mathrm{y}) = \begin{cases} 1,\ \ if\ \ ID1(x\,,y\,) > ID\,(x\,,y\,) \\ 0,\ \ Otherwise \end{cases} \tag{5-5}$$

5.2.1.4. Initial weights map

It is necessary that the focus areas of the IDM contain the maximum focus scale to show the area well, while the defocus areas must have the minimum focus. This process helps eliminate confusion in the two focus and defocus areas, respectively. To get the initial weights map IWM that contain the focus areas mentioned earlier, we use the BWAREAOPEN instruction that removes all connected components (objects) that contain fewer than P pixels from the binary image BW, producing another binary image BW2. **Figure 5-2** -(g) shows the initial weights map of IDM.

$$\mathrm{IWM} = \mathrm{BW2}(\mathrm{BW},\mathrm{P}) = \mathrm{BW2}(\mathrm{IDM},\mathrm{P}) \tag{5-6}$$

5.2.1.5. Initial Fusion

The fast guided filter is used again to obtain the initial fused image based on the two source images as shown by the following equation:

$$\mathrm{IF}(x,y)=\mathrm{FGF}_{r,\varepsilon}\left(\mathrm{IWM}(x,y)I_1(x,y)+\left(1-\mathrm{IWM}(x,y)\right)I_2(x,y)\right) \qquad (5\text{-}7)$$

5.2.1.6. Final weights map

Depending on the initial weights map and the initial fusion image, and using the fast guided filter, the final weights map FWM is extracted in preparation for the final fusion process. FWM contains minimal noise and distortion of IWM on the one hand, and focus of IF image on the other hand.

$$\mathrm{FWM}=\mathrm{FGF}_{r,\varepsilon}\left(\mathrm{IF}(x,y),\ \mathrm{IWM}(x,y)\right) \qquad (5\text{-}8)$$

5.2.1.7. Fused Image

Finally, based on the final weights map, source images, and using the fast guided filter, the two source images are fused and the final fused image FI is obtained, as exemplified by equation 5-9. The final fused result of source images is given in **Figure 5-2** -(J).

$$\mathrm{FI}(x,y)=\mathrm{FGF}_{r,\varepsilon}\left(\mathrm{FWM}(x,y)I_1(x,y)+\left(1-\mathrm{FWM}(x,y)\right)I_2(x,y)\right) \qquad (5\text{-}9)$$

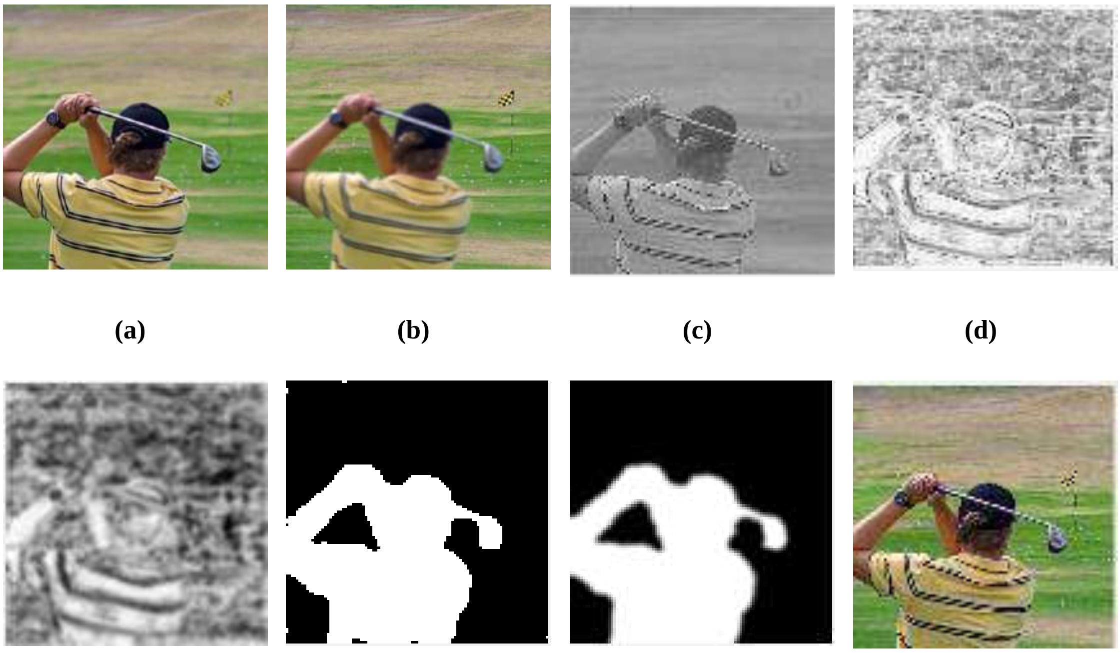

(a) **(b)** **(c)** **(d)**

(e) **(f)** **(g)** **(h)**

(I) (J)

Figure 5-2 Fused results and spatial consistency processing. (a) and (b) sources images, (c) Base layers detection, (d) Structural similarity, (e) Initial detection, (f) Initial detection map, (g) Initial weights map, (h) Initial fusion, (I) final weights map, (J) Fused image.

5.2.2. Results and analysis

In general, the goal of fusion methods is to combine the required complementary information from two input images (source images) into an output image (merged image). It is not enough the visual visibility or to measure the fusion metrics exclusively to judge the fused image as a high-resolution image. It should be judged qualitatively using visual visibility and quantitatively based on fusion metrics. In this section, visual quality and quantitative analysis of different methods are presented.

5.2.2.1. Databases

The proposed method and other methods apply to the image databases shown in **Figure 5-3** and **Figure 5-4** respectively. They are referred to as Database 1 and database 2. Database 1 represents color multi-focus images while database 2 represents non-color multi-focus images. The two datasets used are taken from [103] and [104].

Figure 5-3 Sample of multi-focus test images from the Color dataset.

Figure 5-4 Sample of multi-focus test images from grayscale dataset.

5.2.2.2. Analysis of parameters

The proposed method is based on two main input parameters that directly affect the proposed multi focus image fusion method. First, the blur degree e is entered, followed by the filter size r. These parameters affect the amount of low-pass filtering. First, the blur degree e is entered, followed by the filter size, r. These parameters affect the amount of low-pass filtering. Two multi focus image databases are used, the first in color and the second in grayscale. In this process, the blur degree e was set to 0.3 while the filter size r was set to 5 to get good multi-focus fusion results. The obtained results are presented in tables 5-1 and 5-2, respectively.

5.2.2.3. Qualitative analysis

The visual results of the different multi-focus fusion methods for color images are shown in **Figure 5-5**, while **Figure 5-6** shows the visual results for non-color images. As we discussed in section 1, images can contain some blur, which represents the absence of any information in these images, while the same Images were taken at a different time and contain blurring as well, but in a different place than the first Image. In order to obtain an image with sufficient information, it is necessary to combine two images using the fusion process.

(a) Source-1 (b) Source-2 (c) CNN (d) ICA

(e) GIF (f) MSMFM (g) PCA (h) IFGD

(i) WSSIM (j) FGFDF

Figure 5-5 (Infant) Source images and fused color images of various methods.

(a) Source-1 (b) Source-2 (c) CNN (d) ICA

(e) GIF (f) MSMFM (g) PCA (h) IFGD

(i) WSSIM (j) FGFDF

Figure 5-6 (Woman) Source images and fused color images of various methods.

The fused of some images of database 1 for CNN, ICA, GIF, MSMFM, PCA, IFGD, WSSM and FGFDF methods are shown in **Figure 5-5** and **Figure 5-6**, respectively. Fused image of database 1 for the proposed method is displayed in **Figure 5-5-**j and **Figure 5-6**-j. Through the fused images obtained, it is clear to human vision that the proposed method is superior to other methods in multi focus fusion process, where provides a clearer color images compared to other methods. The difference in visual quality between the different methods and the proposed method is shown in the blurry part of the source of color images, which is displayed, for example, in **Figure 5-5** (a-b), blurred background of human vision, while absence this blur in the part show the child. The same for **Figure 5-6** (a-b). This fog expresses the absence of some information in this part. Where the proposed method succeeded in providing this information from the source images in one image (fused image).

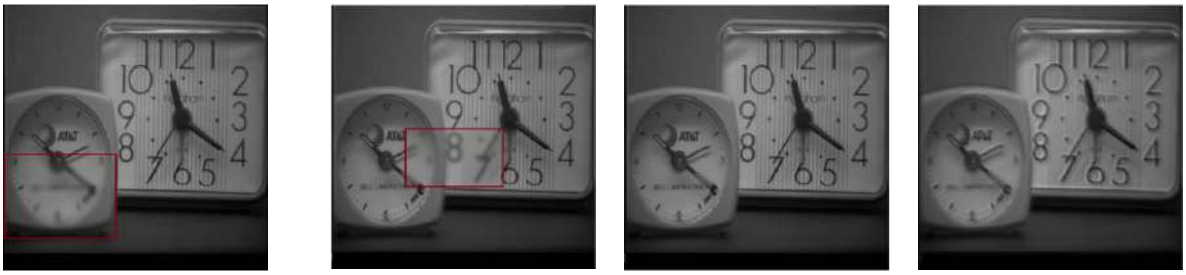

(a) Source-1 (b) Source-2 (c) CNN (d) ICA

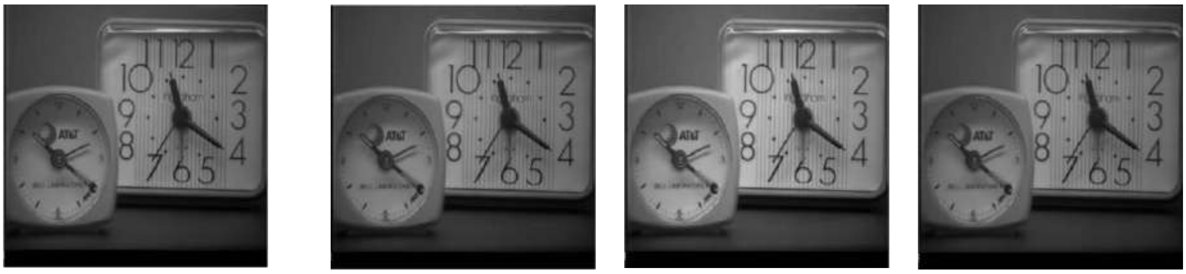

(e) GIF (f) MSMFM (g) PCA (h) IFGD

(i) WSSIM (j) FGFDF

Figure 5-7 (Clock) Source images and fused Grayscale images of various methods.

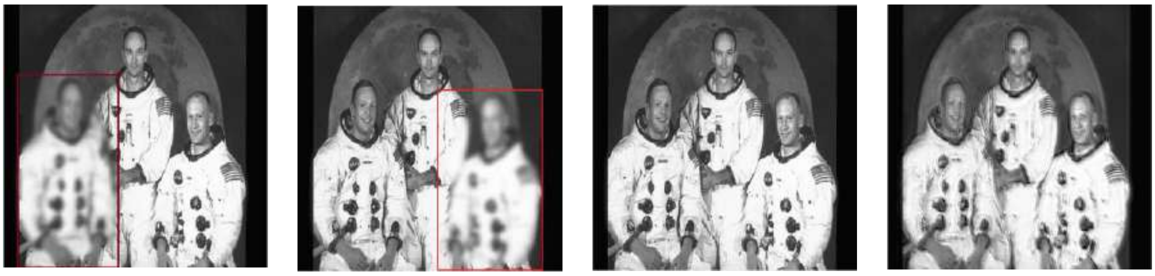

(a) Source-1 (b) Source-2 (c) CNN (d) ICA

(e) GIF (f) MSMFM (g) PCA (h) IFGD

(i) WSSIM (j) FGFDF

Figure 5-8 (Astronauts) Source images and fused Grayscale images of various methods.

Figure 5-7 and **Figure 5-8** represent some fused non-color images of database 2 for CNN, ICA, GIF, MSMFM, PCA, IFGD, WSSM and FGFDF methods. Fused image of database 2 for the proposed method is displayed in **Figure 5-7-j** and **Figure 5-8-j**. The obtained fused images showed the superiority of the proposed method in fusing non-colored images compared to the previously mentioned fused methods. For example, in **Figure 5-7** (a-b), which represents the clock, the first source image (**Figure 5-7**-a) shows a blurred part of human vision, while the second source image shows a blurred portion that differs from the first image. The proposed method provides us with a single image that combines the two source images, which are clear for human vision and of high quality. The same is true for the source images that represent the three astronauts in **Figure 5-8** (a-b), where the proposed method provided one image resulting from fused two images containing blur in two different regions.

5.2.2.4. Quantitative analysis

In this part, a quantitative analysis of the proposed method is performed and it is compared with the different multi focus fusion methods based on the fusion metrics Q_{CB}, Q_y, Q_G, Q_P, $Q^{AB/F}$, and $N^{AB/F}$. Q_{CB} and Q_y measure the contrast and similarity ratio between the source image and the fused image, respectively. While Q_G, Q_P and $Q^{AB/F}$ measure the value of information transmitted from the edges of the source image to the merged image. As for $N^{AB/F}$, it measures the value of unnecessary visual information that has nothing to do with the source image and is present in the resulting image. High values of Q_{CB}, Q_y, Q_G, Q_P and $Q^{AB/F}$ indicate good performance of the methods, and vice versa for $N^{AB/F}$, where low values of $N^{AB/F}$ indicate good performance. Using the above-mentioned metrics, the proposed method is compared to the popular multi-focus fusion methods.

In table 5-1, the performance evaluation of different methods of multi focus color image fusion is presented along with the proposed method. The proposed method achieved through the results in the table 5-1 a clear superiority over the other methods. The proposed method showed good results in each of the metrics of Q_{CB}, Q_y, Q_G and Q_P, compared to CNN, ICA, GIF, MSMFM, PCA, IFGD and WSSM methods. While the other two metrics $Q^{AB/F}$ and $N^{AB/F}$ show the superiority of both ICA and CNN methods. The superiority of the proposed method in most of the measures shows its effectiveness of in multi focus fusion of color images. Table 5-2 shows the results obtained after applying the proposed method to the database of grayscale images. The obtained evaluation metrics results show the superiority of the proposed method in multi-focus grayscale image fusion as in the color images.

Table 5-1 Average values of the evaluation metrics used in multi focus fusion of 20 pairs of color images of different methods.

Dataset 1 color images								
Methods	CNN	ICA	GIF	MSMFM	PCA	IFGD	WSSM	Proposed
Q_{CB}	0.8083 (04)	0.7085 (0)	0.8060 (01)	0.8066 (03)	0.6257 (0)	0.6159 (0)	0.7856 (0)	**0.8093** **(07)**
Q_y	0.9875 (0)	0.9506 (0)	0.7896 (03)	0.9872 (06)	0.8451 (0)	0.8554 (0)	0.9562 (0)	**0.9888** (09)
Q_G	0.7250 (02)	0.6731 (0)	0.7192 (01)	0.7238 (07)	0.5248 (0)	0.6202 (0)	0.6712 (0)	**0.7263** (10)
Q_P	0.8506 (05)	0.8200 (0)	0.8483 (01)	0.8473 (07)	0.7480 (0)	0.7531 (0)	0.8210 (0)	**0.8807** **(13)**
$Q^{AB/F}$	0.9081 (0)	**0.9190** **(06)**	0.8928 (0)	0.9016 (0)	0.8340 (0)	09176 (03)	0.9064 (0)	0.9073 (06)
$N^{AB/F}$ x 10^{-4}	**1.1472** **(0)**	57.0 (0)	0.8737 (02)	2.7688 (0)	**0.0129** (12)	238 (0)	122 (04)	0.6364 (5)

Notes: The decimal numbers inside the parentheses in the table represent the number of pairs that the method has the good metric's value among the 20 pairs color images.

Table 5-2 Average values of the evaluation metrics used in a multi focus fusion of 20 pairs of grayscale images of different methods.

Dataset 2 grayscale images								
Methods	CNN	ICA	GIF	MSMFM	PCA	IFGD	WSSM	Proposed
Q_{CB}	0.9238 (08)	0.8532 (0)	0.9200 (02)	0.9233 (01)	0.8201 (0)	0.6633 (0)	0.8716 (0)	**0.9239** **(11)**
Q_y	0.9976 (03)	0.9655 (0)	0.9963 (05)	0.9975 (01)	0.9404 (0)	0.8647 (0)	0.9685 (0)	**0.9977** **(11)**
Q_G	**0.8905** **(04)**	0.8580 (0)	0.8884 (06)	0.8901 (0)	0.8103 (0)	0.6955 (0)	0.8119 (0)	**0.8905** **(10)**

Q_P	**0.9453** **(08)**	0.9289 (0)	0.9417 (03)	0.9444 (02)	0.8970 (0)	0.8678 (0)	0.9136 (0)	**0.9453** **(12)**
$Q^{AB/F}$	0.9736 (0)	**0.9750** **(10)**	0.9724 (01)	0.9734 (0)	0.9468 (0)	0.9638 (3)	0.9723 (1)	0.9736 (03)
$N^{AB/F}$ x 10^{-4}	0.0928 (0)	82 (0)	0.2973 (03)	0.1875 (0)	**0.0142** **(13)**	264 (0)	49 (0)	0.0803 (05)

Notes: The decimal numbers inside the parentheses in the table represent the number of pairs that the method has the good metric's value among the 20 pairs grayscale images.

Figure 5-9 and **Figure 5-10** provide a further illustration of the in-place performance of the different fusion methods in the two databases. The curve shows the evaluation metric values for each image out of two databases of color and grayscale images, respectively. The curve is attached to the average values of the metrics to show the performance of the proposed method and the different methods for multi-focus image fusion.

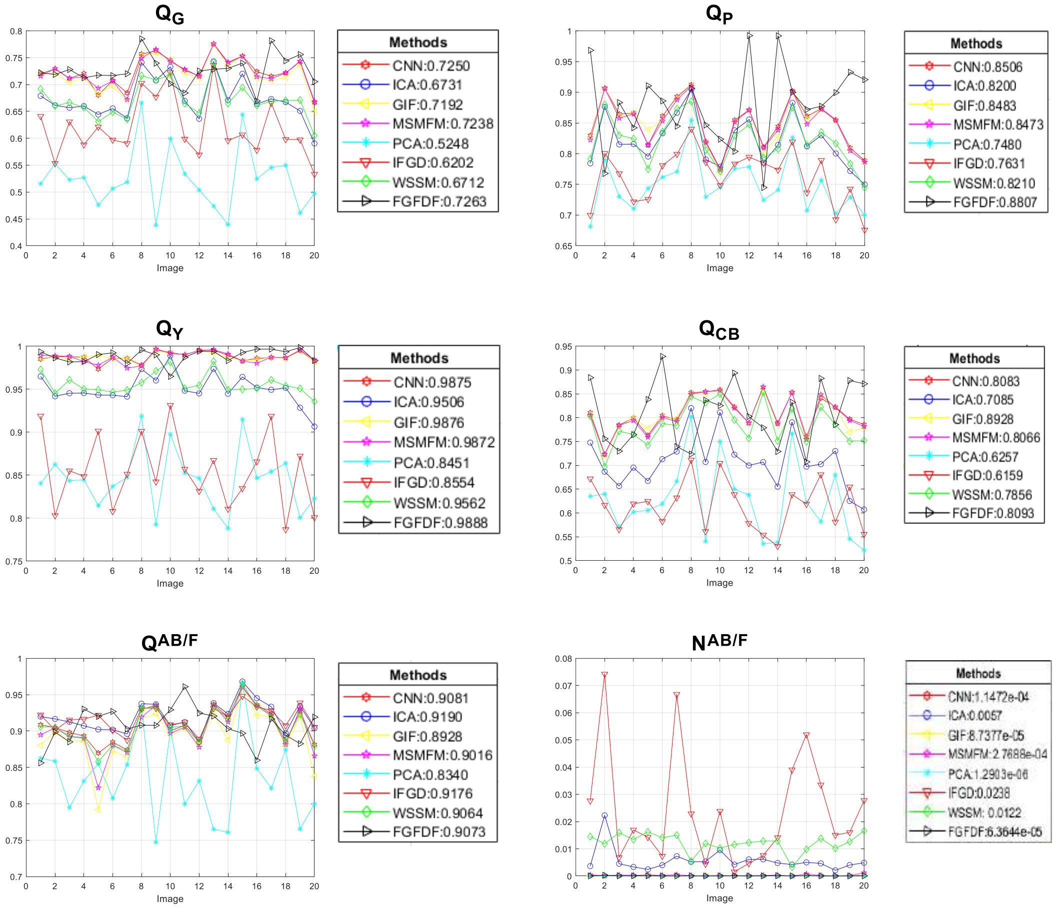

Figure 5-9 The performance of different multi focus fusion methods on a dataset of 20 color images.

Figure 5-10 The performance of different multi focus fusion methods on a dataset of 20 grayscale images.

5.3. Multi-modal medical image fusion based in multiscale alternative approach to cross bilateral filter

5.3.1. Decomposition and reconstruction by the CBF

The multi-scale decomposition allows the representation of edge information at different resolutions. Simultaneous use of CBF can help transfer edge structures at different scales. The main requirement of a merge algorithm is to transfer information from one image to another. Therefore, multiscale CBF operating in structure transfer mode can support this at different resolutions, thus improving performance [106].

5.3.1.1. Cross bilateral filter

The cross bilateral filter (CBF) performs the smoothing by considering the statistical properties of the neighborhood of a pixel [103]. It calculates the output as a linear time invariant (LTI) filter. However, it uses another image for guidance purposes. This additional image can be the entry or its translated version. You can also choose a completely different image for this purpose. Like other edge-preserving filters, CBF can also preserve edge information during the decomposition process, which helps to avoid artifacts [103]. Besides the edge preservation property, CBF also has another property called structure transfer property. If the guide image is the same as the input, then an edge preserving smoothing will be performed, while the structural behavior remains the same. On the other hand, when the guide image differs from the input, the smoothing process is regulated by the guide image structures. So when we apply CBF on images, the edge structures can be transferred.

Suppose that A and B are two different images, $G_{\sigma s}(K-I)$ is the kernel space of A and $G_{\sigma_S}(B_K-B_I)$ is the kernel range calculated on the image B then the mathematical equation of the CBF is given by [106]:

$$A_{CBF}[B,A]_K=\frac{1}{W_K}\sum_{I\in S}G_{\sigma_S}(K-I)G_{\sigma_r}(B_K-B_I)A_I \tag{5-10}$$

Where:

$$W_K=\sum_{I\in S}G_{\sigma_S}(K-I)G_{\sigma_S}(B_K-B_I) \tag{5-11}$$

$$G_\sigma(K-I)=\frac{1}{2\pi\sigma^2}\exp\left(\frac{K-I^2}{2\sigma^2}\right) \tag{5-12}$$

G_{σ_S} is the Gaussian spatial kernel and G_{σ_r} is the Gaussian kernel of the scale. The parameters σ_S and σ_r are spatial and range parameters, which control the smoothing respectively.

The multiscale decomposition of the image I can be performed using CBF. Suppose that b^{n-1}, G^{n-1} are the base layer and the guide images at level (n - 1), σ_s and σ_r are the spatial and range parameters and r is the filter window size, then the base layer b^n can be calculated by performing a CBF of the image b^{n-1} considering G^{n-1} as the guide image. The d^ndetail images can be calculated by taking the difference between the previous base layer b^{n-1} and the current base layer b^n. These expressions are given by [107]:

$$b^n = CBF\left(b^{n-1}, G^{n-1}, \sigma_S, \sigma_r, r\right) \tag{5-13}$$

$$d^n = b^{n-1} - b^n \tag{5-14}$$

Where:

$$b^0 = I \tag{5-15}$$

The input image I can be reconstructed from base layer b^n and detail layers détails d^k, $k = (1, \ldots, n)$ as follows [106]:

$$I = \sum_{k=1}^{n} d^k + b^n \tag{5-16}$$

This multiscale decomposition and reconstruction process is illustrated by algorithm 1 and **Figure 5-11**.

Algorithm 1: Decomposition and reconstruction of an image by the CBF.

```
Inputs: Image to filter I, guidance image $G^0$, $\sigma_s$, $\sigma_r$, $r$ and the number of levels $n$

Outputs: Reconstructed image $I$ and base layers and details $(b^k, d^k)$

    1. $b^0 = I$
    2. For $k = 1, 2, 3, \ldots, n$ do
           $b^k = CBF\left(b^{k-1}, G^{k-1}, \sigma_s, \sigma_r, r\right)$
           $d^k = b^{k-1} - b^k$
       End for
    3. $I = \sum_{k=1}^{n} d^k + b^n$
```

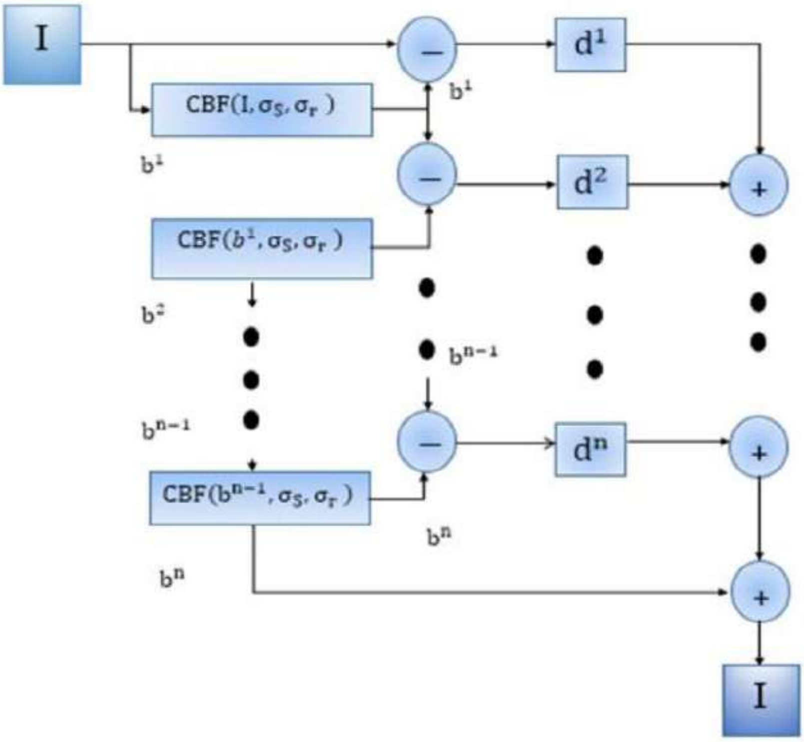

Figure 5-11 Functional diagram of the multi-scale image decomposition and reconstruction of an I image by the CBF.

5.3.2. Proposed image fusion method

The proposed method MACBFF requires the following steps to perform the merge:

Multi-scale decomposition of source images using CBF.

- Generation of visual saliencies of each input image at different levels.
- Calculation of weight maps corresponding to detail layers.
- Combine detail layers using weight maps
- Generation of the final fused image.

5.3.2.1. Multi-scale image decomposition

Consider two source images I_1 and I_2 of the same size. These two images are decomposed by CBF to a base layer B containing large scale variations and detail layer D containing small scale variations as follows [108]:

$$B_1^k = \begin{cases} I_1 & si\ k = 0 \\ CBF\left(B_1^{k-1}, B_2^{k-1}, \sigma_S, \sigma_r, r\right) si\ k = 1,\ldots,n \end{cases} \tag{5-17}$$

$$B_2^k = \begin{cases} I_2 & si\ k = 0 \\ CBF\left(B_2^{k-1}, B_1^{k-1}, \sigma_S, \sigma_r, r\right) si & k = 1, \ldots, n \end{cases} \quad (5\text{-}18)$$

Where B_1^k and B_2^k are base layers of two source images at k level which depend on their previous level base layers B_1^{k-1} and B_2^{k-1} respectively. The detail layers D_1^k and D_2^k are obtained by finding the difference between the previous and current level base layers:

$$D_1^k = B_1^{k-1} - B_1^k,\ k = 1, \ldots, n \quad (5\text{-}19)$$

$$D_2^k = B_1^{k-1} - B_2^k, k = 1, \ldots, n \quad (5\text{-}20)$$

5.3.2.2. Generation of visual salience maps

Visually salience maps of source images are calculated by taking the absolute value of the detail layers D_1^k, D_2^k as follows:

$$S_1^k = \left|D_1^k\right| \quad (5\text{-}21)$$

$$S_2^k = \left|D_2^k\right| \quad (5\text{-}22)$$

5.3.2.3. Calculation of the weight map:

We need to integrate all the targeted regions into a single fused image. Weight maps representing complementary information based on salience information can automatically integrate detail layer. The weight maps W_1^k and W_2^k are calculated by normalizing the extracted saliency maps as follows:

$$W_1^k = \frac{S_1^k}{\sum_{i=1}^{2} S_i^K},\ k = 1, 2, \ldots, n \quad (5\text{-}23)$$

$$W_2^k = \frac{S_2^k}{\sum_{i=1}^{2} S_i^k},\ k = 1, 2, \ldots, n \quad (5\text{-}24)$$

5.3.2.4. Detail layer fusion

The detail layers are built into each k scale using the W_1^k and W_2^k weight maps using a linear combination:

$$D_F^k = W_1^k D_1^k + W_2^k D_2^k \quad (5\text{-}25)$$

The final detail layer D_F is obtained by combining fused detail layers obtained at each scale. This fused detail image D_F provides most of the visual information of the fused image:

$$D_F = \sum_{k=1}^{n} D_F^k \tag{5-26}$$

5.3.2.5. Reconstruction of the fused image

The fused image is obtained by combining the base layer B_F and the detail layer D_F :

$$F = B_F + D_F \tag{5-27}$$

Figure 5-12 presents and summarizes the functional diagram of the MACBFF method and Algorithm II.3 summarizes the necessary steps of image fusion by the MACBFF method.

Algorithm 2: Image fusion using the MACBFF method

```
Inputs: source images $I_1$ & $I_2$ ,$\sigma_S, \sigma_r, r$ and $n$
Outputs: Fused image $F$
1. $B_1^0 = I_1, B_2^0 = I_2$
2. For $k = 1, 2, 3, \ldots, n$ do
        $B_1^k = CBF\left(B_1^{k-1}, B_2^{k-1}, \sigma_S, \sigma_r, r\right)$
        $B_2^k = CBF\left(B_2^{k-1}, B_1^{k-1}, \sigma_S, \sigma_r, r\right)$
        $D_1^k = B_1^{k-1} - B_1^k$
        $D_2^k = B_1^{k-1} - B_2^k$
        $S_1^k = \left|D_1^k\right|$
        $S_2^k = \left|D_2^k\right|$
        $W_1^k = \frac{S_1^k}{\sum_{i=1}^{2} S_i^k}$
        $W_2^k = \frac{S_2^k}{\sum_{i=1}^{2} S_i^k}$
        $D_F^k = W_1^k D_1^k + W_2^k D_2^k$
   End for
3. $D_F = \sum_{k=1}^{n} D_F^k$
```

4. $B_F = \frac{1}{2}\left(B_1^n + B_2^n\right)$

5. $F = B_F + D_F$

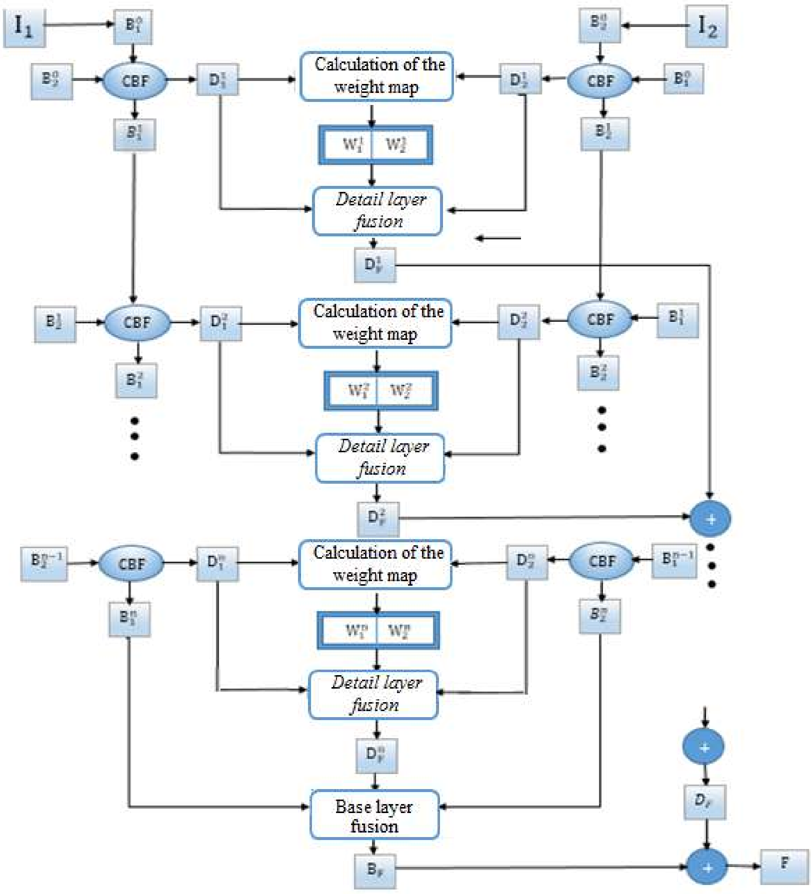

Figure 5-12 Functional diagram of the ACBFF method.

5.3.2.6. Extension of the CBFF method to color medical images

For medical images, there are two types of images; MRI and CT images are grayscale images while PET and SPECT images are color images. The principle of the proposed MACBFF is presented in **Figure 5-13**, and have the following steps:

- Convert the three bands of the RGB space of the medical image to the YUV space.

  Where Y is the luminance, U and V are the blue and red complements.

- Apply the CBFF method between the Y intensity component of the color medical image (PET or SPECT) and the intensity of the grayscale image (MRI or CT) to obtain the fused Y intensity component.
- Switching from YUV color space to RGB color space to obtain a color fused image.

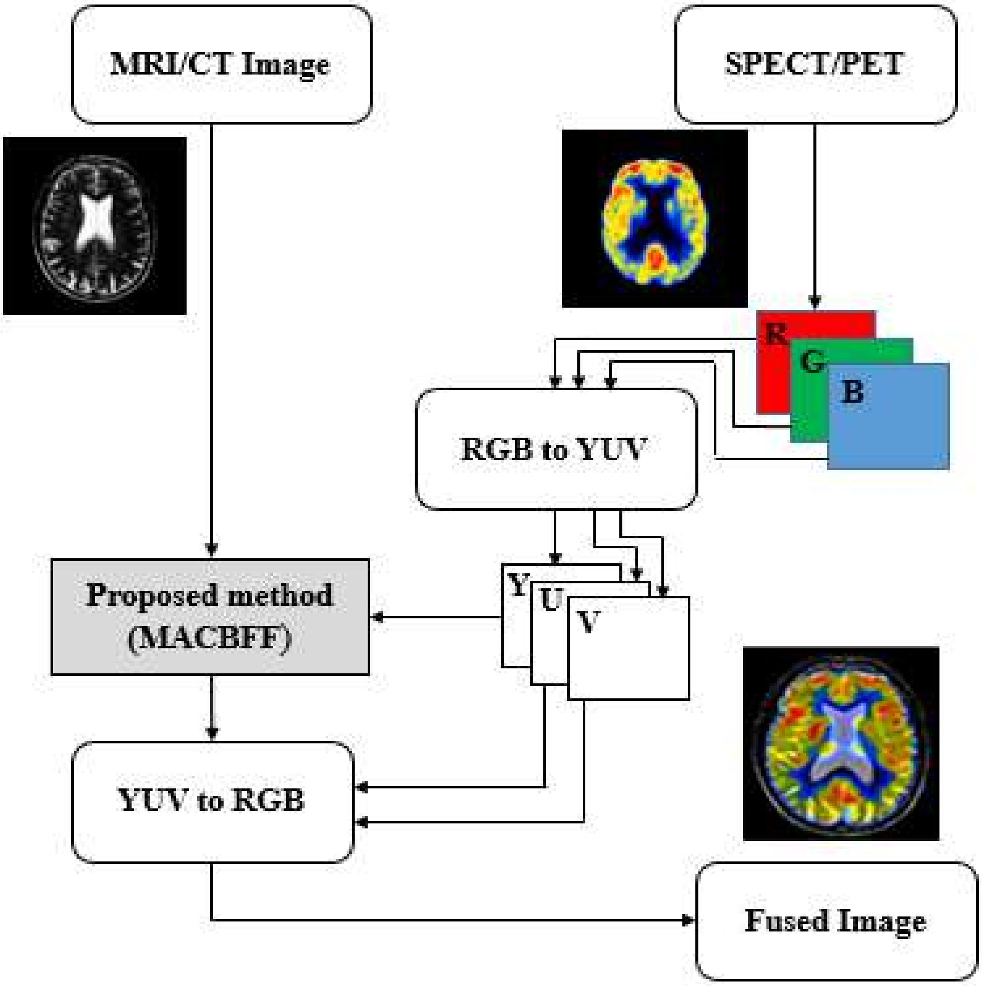

Figure 5-13 Methodology used to fuse MRI/CT and SPECT/PET medical images.

5.3.3. Experiments and analysis

5.3.3.1. Database

In medical image fusion, we have chosen two pairs of medical images in gray level (CT / MRI) which are represented in **Figure 5-14**, and three pairs of medical images in color / gray level (CT/SPECT), (MRI/SPECT and (MRI/PET) which are shown in **Figure 5-15**, and which are available at the web http://www.med.harvard.edu/AANLIB/home.html.

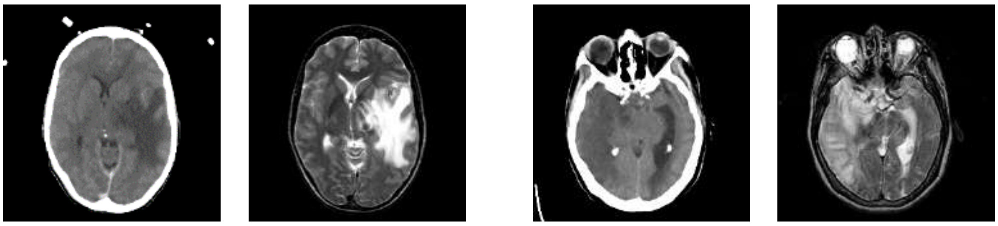

(a) CT/ MRI-1 Image pair (b) CT/MRI-2 Image pair

Figure 5-14 Image pairs used for the MACBFF in gray level.

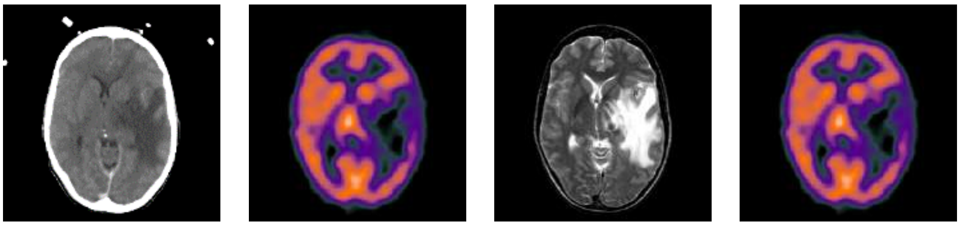

(a) CT/ SPECT Image pair (b) MRI/ SPECT Image pair

(c) MRI/ PET Image pair

Figure 5-15 Image pairs used for the MACBFF in in gray/ color level.

5.3.3.2. Quantitative analysis

In this study, we will combine five pairs of medical images of a human brain, these images were obtained from different imaging methods, as shown in Figures 5-3 and 5-4. Image pairs are (CT/ MRI_1) and (CT/ MRI_2), (CT/ SPECT), (MRI/ SPECT), and (MRI/ PET), respectively. The results obtained are analyzed with the nine validation parameters, and quantitative analysis of various image pairs used are shown in tables 5-3, 5-4, 5-5, 5-6 and 5-7. Where the best values are highlighted in bold.

Table 5-3 Quantitative analysis of various fusion algorithms for CT/MRI-1 image pair.

Methods	**MACBFF**	**TIF**	**ACBFF**
API	**60.246**	56.342	51.054
SD	**77.324**	73.504	66.290
E	**4.369**	4.262	4.341
MI	**3.199**	2.941	2.996
FS	**1.999**	1.979	1.952
CC	0.971	0.965	**0.971**

$Q^{AB/F}$	0.784	0.764	**0.814**
$L^{AB/F}$	0.208	0.223	**0.170**
$N^{AB/F}$	**0.006**	0.011	0.015

Table 5-4 Quantitative analysis of various fusion algorithms for CT/ MRI-2 image pair.

Method	**MACBFF**	**TIF**	**ACBFF**
API	**45.094**	44.726	44.93
SD	**56.130**	55.732	54.929
E	5.091	5.191	**5.352**
MI	3.503	3.544	**4.377**
FS	**1.962**	1.961	1.89
CC	**0.982**	0.981	0.98
$Q^{AB/F}$	**0.806**	0.791	0.802
$L^{AB/F}$	**0.171**	**0**.176	0.183
$N^{AB/F}$	0.022	0.031	**0.014**

Table 5-5 Quantitative analysis of various fusion algorithms for CT/ SPECT image pair.

Method	**MACBFF**	**TIF**	**ACBFF**
API	**53.386**	51.525	52.335
SD	**70.6**	70	70.45
E	4.094	**4.212**	4.198
MI	**3.907**	3.141	3.259
FS	**1.993**	1.992	1.941
CC	**0.996**	0.978	0.993
$Q^{AB/F}$	0.874	0.879	**0.901**
$L^{AB/F}$	0.120	0.106	**0.083**

$N^{AB/F}$	**0.005**	0.014	0.015

Table 5-6 Quantitative analysis of various fusion algorithms for MRI/ SPECT image pair.

Method	**MACBFF**	**TIF**	**ACBFF**
API	**46.322**	40.774	41.192
SD	**64.902**	57.102	58.886
E	4.27	4.2	**4.29**
MI	**3.718**	2.674	3.265
FS	**1.986**	1.971	1.878
CC	**0.986**	0.974	0.983
$Q^{AB/F}$	0.793	0.793	**0.862**
$L^{AB/F}$	0.199	0.185	**0.118**
$N^{AB/F}$	**0.007**	0.021	0.018

Table 5-7 Quantitative analysis of various fusion algorithms for MRI/ PET image pair.

Method	**MACBFF**	**TIF**	**ACBFF**
API	**55.666**	45.23	38.39
SD	**79.22**	67.4	63.121
E	4.364	4.325	**4.547**
MI	3.466	2.887	**3.839**
FS	1.958	**1.99**	1.834
CC	**0.842**	0.836	0.837
$Q^{AB/F}$	0.703	0.711	**0.841**
$L^{AB/F}$	0.282	0.263	**0.142**
$N^{AB/F}$	**0.013**	0.025	0.016

Through the obtained results, the proposed algorithm showed a good ability to achieve fusion of medical images with high accuracy compared to other methods. Tables 5-5, 5-4,5-3, and 5-6 of the 2 and 3 pairs respectively show that MACBFF gives good results in most validation parameters, while Table 5-3 shows an equivalent performance between the proposed method and the other methods.

5.3.3.3. Qualitative analysis

Consider the pairs of medical images taken from the different imaging methods (CT, MRI, PET, SPECT) as shown in Figure 5-3 and 5-4. As explained in Section 1, each imaging method can show some information about the disease to be diagnosed, but it does not show some information that could be in the other imaging method, as is the case with CT and MRI. Therefore, it is necessary to combine two images from two different imaging methods into one image using the fusion process in order to properly diagnose and treat the disease

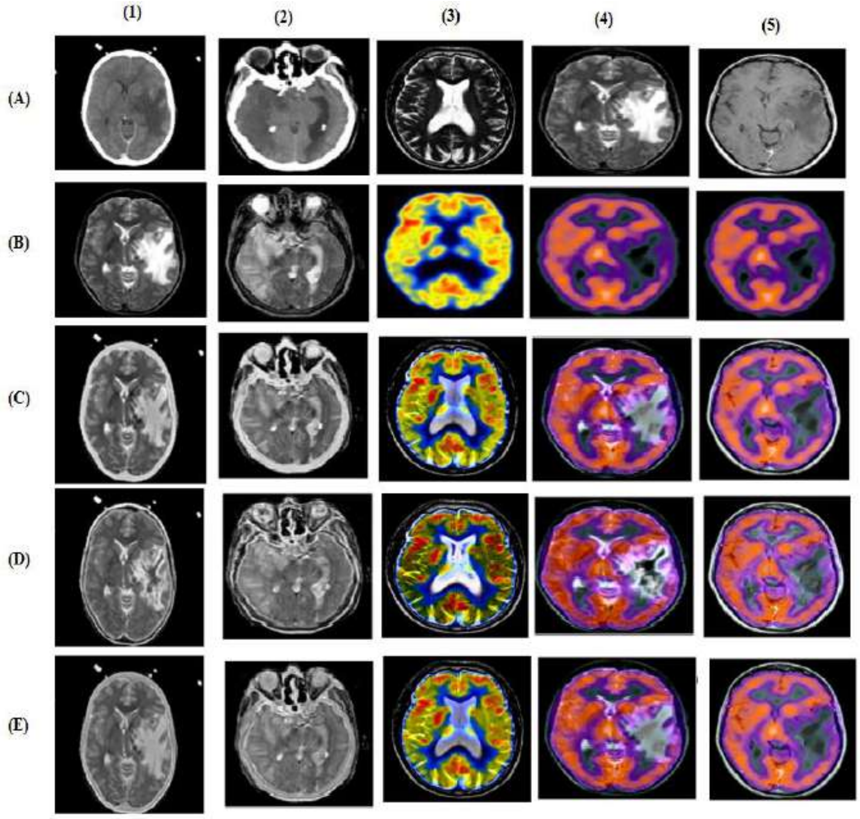

Figure 5-16 Multimodal fusion results of medical images (a) Source image 1 (B) Source image 2, fused images obtained by the (C) TIF (D) ACBFF (E) Proposed method MACBFF.

Visual quality analysis of different fusion methods for images are presented in figure 5-15. Figure 6a and b show the source images for the different imaging methods that have been combined, while Figure. 5-16-C, D, and E show the visual results of the recording process using the TIF, ACBFF, and MACBFF methods, respectively. From the visual results, it appears that the proposed method gives a picture free of distortions and is clearer for the diagnosis of the disease compared to the TIF and ACBFF methods, which show some distortions in the fused image.

5.4. Conclusion

In this chapter, we have tested the effectiveness of the proposed approach and we have reported the experimental results. First, the proposed methods were explained, then the database on which these methods were applied, whether for medical images or multi-focus images, was shown. Then, we have reported our qualitative analysis and quantitative analysis findings for multi-focus image fusion and multi-modal medical image fusion. After performing the fusion process, the results obtained revealed several facts. First, it shows the efficiency of the proposed approach and its superiority over the modern approach. Second, the proposed approach showed high-quality visual results. Third, the proposed approach achieved high accuracy fusion. Fourth, the success of meta-heuristic algorithms in providing good input parameters.

GENERAL CONCLUSION

The main objective of image registration and fusion is to provide an image that contains sufficient complementary information and is more useful in the analysis process. However, these methods result in some undesirable distortions. This thesis aims to register images based on meta-heuristic algorithms and image fusion using new and effective methods.

In this thesis, we have done an in-depth study of medical images, including but not limited to CT images and MRI images. Due to the emergence of the COVID-19 epidemic during the research period, attention was paid to CT images of the lungs of patients with this disease. Initially, we applied the meta-heuristic GWO, SCA, FA, ABC, CSA and PSO algorithms to registered CT and MRI images. Taking advantage of the algorithms used, we developed a new HPSGWO algorithm resulting from the hybridization of the two algorithms GWO and PSO. The COVID-19 images were combined using the new HPSGWO algorithm that provides an image with complementary information that facilitates the work of the radiologist to diagnose COVID-19. On the other hand, we also developed the new ISCA algorithm and used it to register CT images of the lungs infected with COVID-19 patients with the aim of improving the diagnosis of this critical disease.

In the image fusion section, many medical images of different databases and different imaging techniques were fused, including CT, MRI images, PET and SPECT. In addition, the multi-focus images are fused after the detection of the focus area caused by defects in the sensors, which explains the lack of some information in that part of the image. For multi-focus image fusion, we relied on the fast-guided filter, while in medical image fusion, a multi-scale Alternative approach to cross-bilateral filter was used.

The main contributions of the proposed approach to image registration mainly lie in providing a registered image containing the complementary information required to facilitate the diagnostic process in the medical field based on meta-heuristic algorithms. In addition, it reduces the distortions that appear in other registration methods. As well as developing new algorithms and using them to registered the CT images of the lungs of people infected with COVID-19 to provide an image that facilitates the diagnosis of this disease. The same for image fusion, the main contributions of the proposed approach are fused of multi-focus images after the detection of focus areas based on the fast-guided filter. On the other hand multi-modal medical image fusion based on a multi-scale alternative approach to cross-bilateral filter.

To confirm the superiority and effectiveness of the proposed methods for image registration and fusion we have conducted extensive experiments. By viewing the experimental results, we can make the following observations:

- The proposed approaches have successfully treated the problem of registration and fusion of images.
- The proposed approach to image registration has resulted in providing an image that facilitates the treatment process in the medical and electronic fields.
- The proposed methods achieved great speed and high accuracy in image registration and fusion
- The proposed approach has proven its strength against several state-of-the-art methods.
- The proposed approach has contributed to the fight against the Covid-19 epidemic by providing a picture that facilitates the process of diagnosing infection with this disease

Further studies can be conducted to develop the proposed approach by benefit wwwxof the advantages of each algorithm separately. Due to the multiplicity of advantages between the various methods, an algorithm can be created that combines the advantages of each method, such as speed and accuracy. Furthermore, it is possible to rely on meta-heuristic algorithms in image registration on the one hand, while using another effective method for the fusion process on the other hand.

SCIENTIFIC PRODUCTION

Publications

- Dida, Hedifa, Fella Charif, and Abderrazak Benchabane. "Registration of computed tomography images of a lung infected with COVID-19 based in the new meta-heuristic algorithm HPSGWO." *Multimedia Tools and Applications* 81.13 (2022): 18955-18976.
- Dida, H., Charif, F., & Benchabane, A. (2022). Image registration of computed tomography of lung infected with COVID-19 using an improved sine cosine algorithm. *Medical & Biological Engineering & Computing*, *60*(9), 2521-2535.

International Communication

- Dida, Hedifa, Fella Charif, and Abderrazak Benchabane. "Grey Wolf Optimizer for Multimodal Medical Image Registration." 2020 Fourth International Conference On Intelligent Computing in Data Sciences (ICDS). IEEE, 2020.
- Dida, Hedifa, Fella Charif, and Abderrazak Benchabane. "A comparative study of two meta-heuristic algorithms for MRI and CT images registration." 2020 3rd International Conference on Information and Communications Technology (ICOIACT). IEEE, 2020.

National Communication

- Dida, Hedifa, Fella Charif, and Abderrazak Benchabane. “A comparative study of two meta-heuristic approaches for image registration of printed circuit boards” At the first National Conference on Artificial Intelligence and Information Technologies (CNAT’21).
- Dida, Hedifa, Fella Charif, and Abderrazak Benchabane. “Multi-modal medical image fusion based in Multiscale Alternative approach to cross bilateral filter” At the first National Conference on Artificial Intelligence and Information Technologies

REFERENCES

[1] H. Kaur, D. Koundal, and V. Kadyan, “Image Fusion Techniques: A Survey,” *Arch. Comput. Methods Eng.*, vol. 28, no. 7, pp. 4425–4447, 2021, doi: 10.1007/s11831-021-09540-7.

[2] Borovec, J., Kybic, J., Arganda-Carreras, I., Sorokin, D. V., Bueno, G., Khvostikov, A. V., ... & Muñoz-Barrutia, A. (2020). ANHIR: automatic non-rigid histological image registration challenge. *IEEE transactions on medical imaging*, *39*(10), 3042-3052.

[3] B. Meher, S. Agrawal, R. Panda, and A. Abraham, “A survey on region based image fusion methods,” *Inf. Fusion*, vol. 48, pp. 119–132, 2019, doi: 10.1016/j.inffus.2018.07.010.

[4] Du, K. L., & Swamy, M. N. S. (2016). Search and optimization by metaheuristics. *Techniques and Algorithms Inspired by Nature*, 1-10.

[5] H. Dida, F. Charif, and A. Benchabane, “Grey Wolf Optimizer for Multimodal Medical Image Registration,” *4th Int. Conf. Intell. Comput. Data Sci. ICDS 2020*, no. 1, pp. 0–4, 2020, doi: 10.1109/ICDS50568.2020.9268771.

[6] Bhataria, K. C., & Shah, B. K. (2018, February). A review of image fusion techniques. In *2018 Second International Conference on Computing Methodologies and Communication (ICCMC)* (pp. 114-123). IEEE.

[7] Kulkarni, S. C., & Rege, P. P. (2020). Pixel level fusion techniques for SAR and optical images: A review. *Information Fusion*, *59*, 13-29.

[8] W. Li, L. Jia, and J. Du, “Multi-Modal Sensor Medical Image Fusion Based on Multiple Salient Features with Guided Image Filter,” *IEEE Access*, vol. 7, pp. 173019–173033, 2019, doi: 10.1109/ACCESS.2019.2953786.

[9] Sahu, D. K., & Parsai, M. P. (2012). Different image fusion techniques–a critical review. *International Journal of Modern Engineering Research (IJMER)*, *2*(5), 4298-4301.

[10] H. Peng, B. Li, Q. Yang, and J. Wang, “Multi-focus image fusion approach based on CNP systems in NSCT domain,” *Comput. Vis. Image Underst.*, vol. 210, no. May, 2021, doi: 10.1016/j.cviu.2021.103228.

[11] K. Kalaivani and Y. A. V. Phamila, “Analysis of image fusion techniques based on quality assessment metrics,” *Indian J. Sci. Technol.*, vol. 9, no. 31, 2016, doi: 10.17485/ijst/2016/v9i31/92553.

[12] Liu, Y., Wang, L., Cheng, J., Li, C., & Chen, X. (2020). Multi-focus image fusion: A survey of the state of the art. Information Fusion, 64, 71-91.

[13] N. Mitianoudis and T. Stathaki, “Pixel-based and region-based image fusion schemes using ICA bases,” vol. 8, pp. 131–142, 2007, doi: 10.1016/j.inffus.2005.09.001.

[14] K. C. Bhataria and B. K. Shah, “A Review of Image Fusion Techniques,” *Proc. 2nd Int. Conf. Comput. Methodol. Commun. ICCMC 2018*, no. Iccmc, pp. 114–123, 2018, doi: 10.1109/ICCMC.2018.8487686.

[15] Y. Liu, X. Chen, H. Peng, and Z. Wang, “Multi-focus image fusion with a deep convolutional neural network,” *Inf. Fusion*, vol. 36, pp. 191–207, 2017, doi: 10.1016/j.inffus.2016.12.001.

[16] S. Bhat and D. Koundal, *Multi-focus image fusion techniques: a survey,* vol. 54, no. 8. Springer Netherlands, 2021.

[17] W. Zhao, D. Wang, and H. Lu, “Multi-focus image fusion with a natural enhancement via a joint multi-level deeply supervised convolutional neural network,” *IEEE Trans. Circuits Syst. Video Technol.*, vol. 29, no. 4, pp. 1102–1115, 2019, doi: 10.1109/TCSVT.2018.2821177.

[18] M. A. Rahman, S. Liu, C. Y. Wong, S. C. F. Lin, S. C. Liu, and N. M. Kwok, “Multi-focal image fusion using degree of focus and fuzzy logic,” *Digit. Signal Process. A Rev. J.*, vol. 60, pp. 1–19, 2017, doi: 10.1016/j.dsp.2016.08.004.

[19] Z. Lu, B. Long, K. Li, and F. Lu, “Contrast Enhancement,” *IEEE Signal Process. Lett.*, vol. 25, no. 10, pp. 1585–1589, 2018, doi: 10.1109/LSP.2018.2867896.

[20] Y. Chen and R. S. Blum, “A new automated quality assessment algorithm for image fusion,” *Image Vis. Comput.*, vol. 27, no. 10, pp. 1421–1432, 2009, doi: 10.1016/j.imavis.2007.12.002.

[21] H. Zeng and X. Ben Wu, “Utilities of edge-based metrics for studying landscape fragmentation,” vol. 29, pp. 159–178, 2005, doi: 10.1016/j.compenvurbsys.2003.09.002.

[22] P. M. Favi, C. Stephens, N. Neilsen, R. Hammonds, R. Benson, and M. Dhar, “Proliferation, osteogenic and chrondrogenic differentiation of equine-derived bone marrow mesenchymal stem cells on bacterial cellulose scaffolds,” *FASEB J.*, vol. 26, no. S1, pp. 137–154, 2012, doi: 10.1096/fasebj.26.1_supplement.917.3.

[23] B. Zitová and J. Flusser, “Image registration methods: A survey,” *Image Vis. Comput.*, vol. 21, no. 11, pp. 977–1000, 2003, doi: 10.1016/S0262-8856(03)00137-9.

[24] P. Taylor, Z. Xiong, and Y. Zhang, “International Journal of Image and Data Fusion A critical review of image registration methods,” no. September 2013, pp. 37–41, 2010, doi: 10.1080/19479831003802790.

[25] M. IZhou W, Bovik AC, Sheikh HR, Simoncelli EP (2004) Image quality assessment: from error measurement to structural similarity. IEEE Transactions on Image Processing 48: 600-642.

[26] Z. Wang, A. C. Bovik, H. R. Sheikh, and E. P. Simoncelli, “Image quality assessment: From error visibility to structural similarity,” *IEEE Trans. Image Process.*, vol. 13, no. 4, pp. 600–612, 2004, doi: 10.1109/TIP.2003.819861.

[27] G. Song, J. Han, Y. Zhao, Z. Wang, and H. Du, “A Review on Medical Image Registration as an Optimization Problem,” *Curr. Med. Imaging Rev.*, vol. 13, no. 3, pp. 274–283, 2017, doi: 10.2174/1573405612666160920123955.

[28] J. Antoine Maintz, “A survey of medical image registration,” *Med. Image Anal.*, vol. 2, no. 1, pp. 1–36, 1998, doi: 10.1016/s1361-8415(98)80001-7.

[29] F. E. Z. A. El-Gamal, M. Elmogy, and A. Atwan, “Current trends in medical image registration and fusion,” *Egypt. Informatics J.*, vol. 17, no. 1, pp. 99–124, 2016, doi: 10.1016/j.eij.2015.09.002.

[30] Hajnal, J. V., & Hill, D. L. (2001). Medical image registration. CRC press.

[31] H. B. Mitchell, *Data fusion: Concepts and ideas*. 2012.

[32] D. A. Simon, R. V. O. Toole, M. Blackwell, F. Morgan, A. M. Digioia, and T. Kanade, “Accuracy Validation in Image-Guided Orthopaedic Surgery,” 1995.

[33] Goshtasby, A. A. (2005). 2-D and 3-D image registration: for medical, remote sensing, and industrial applications. John Wiley & Sons.

[34] C. R. Meyer, R. L. Wahl, J. A. Brunberg, and L. E. Quint, “Simultaneous Usage of Homologous Points, Lines, and Planes for Optimal, 3-D, Linear Registration of Multimodality Imaging Data,” *IEEE Trans. Med. Imaging*, vol. 14, no. 1, pp. 1–11, 1995, doi: 10.1109/42.370397.

[35] G. P. Penney, P. J. Edwards, J. H. Hipwell, M. Slomczykowski, I. Revie, and D. J. Hawkes, “Postoperative calculation of acetabular cup position using 2-D-3-D registration,” *IEEE Trans. Biomed. Eng.*, vol. 54, no. 7, pp. 1342–1348, 2007, doi: 10.1109/TBME.2007.890737.

[36] H. Sundar, A. Khamene, C. Xu, F. Sauer, and C. Davatzikos, “A novel 2D-3D registration algorithm for aligning fluoro images with 3D pre-op CT/MR images,” *Med. Imaging 2006 Vis. Image-Guided Proced. Disp.*, vol. 6141, p. 61412K, 2006, doi: 10.1117/12.654251.

[37] A. Horé, “Image quality metrics : PSNR vs . SSIM,” 2010, doi: 10.1109/ICPR.2010.579.

[38] X. Luo, Z. Zhang, C. Zhang, and X. Wu, “Multi-focus Image Fusion Using HOSVD and Edge Intensity,” *J. Vis. Commun. Image Represent.*, no. February, 2017, doi: 10.1016/j.jvcir.2017.02.006.

[39] D. P. Bavirisetti, V. Kollu, X. Gang, and R. Dhuli, “Fusion of MRI and CT images using guided image filter and image statistics,” *Int. J. Imaging Syst. Technol.*, vol. 27, no. 3, pp. 227–237, 2017, doi: 10.1002/ima.22228.

[40] V. Petrović and C. Xydeas, “Objective image fusion performance characterisation,” *Proc. IEEE Int. Conf. Comput. Vis.*, vol. II, pp. 1866–1871, 2005, doi: 10.1109/ICCV.2005.175.

[41] J. Jose *et al.*, “An image quality enhancement scheme employing adolescent identity search algorithm in the NSST domain for multimodal medical image fusion,” *Biomed. Signal Process. Control*, vol. 66, no. August 2020, p. 102480, 2021, doi: 10.1016/j.bspc.2021.102480.

[42] C. T. Kavitha and C. Chellamuthu, “Multimodal medical image fusion based on integer wavelet transform and neuro-fuzzy,” *Proc. 2010 Int. Conf. Signal Image Process. ICSIP 2010*, pp. 296–300, 2010, doi: 10.1109/ICSIP.2010.5697486.

[43] S. Wu, P. He, S. Yu, S. Zhou, J. Xia, and Y. Xie, “To Align Multimodal Lumbar Spine

Images via Bending Energy Constrained Normalized Mutual Information," vol. 2020, 2020.

[44] M. Zhou, G. Wang, J. Wang, C. Hui, and W. Yang, "Defect Detection of Printing Images on Cans Based on SSIM and Chromatism," pp. 1–5, 2017.

[45] K. Shima *et al.*, "Analysis of Post-exposure Density Growth in Radiochromic Film with Respect to the Radiation Dose," vol. 305, pp. 301–305, 2012, doi: 10.1269/jrr.11091.

[46] A. Kaveh and A. Dadras, "A novel meta-heuristic optimization algorithm: Thermal exchange optimization," *Adv. Eng. Softw.*, vol. 110, pp. 69–84, 2017, doi: 10.1016/j.advengsoft.2017.03.014.

[47] G. Ozdemir and N. Karaboga, "A review on the cosine modulated filter bank studies using meta-heuristic optimization algorithms," *Artif. Intell. Rev.*, vol. 52, no. 3, pp. 1629–1653, 2019, doi: 10.1007/s10462-017-9595-x.

[48] A. E. Ezugwu *et al.*, *Metaheuristics: a comprehensive overview and classification along with bibliometric analysis*, vol. 54, no. 6. Springer Netherlands, 2021.

[49] G. Dhiman and V. Kumar, "Spotted hyena optimizer: A novel bio-inspired based metaheuristic technique for engineering applications," *Adv. Eng. Softw.*, vol. 114, pp. 48–70, 2017, doi: 10.1016/j.advengsoft.2017.05.014.

[50] S. Katoch, S. S. Chauhan, and V. Kumar, *A review on genetic algorithm: past, present, and future*, vol. 80, no. 5. Multimedia Tools and Applications, 2021.

[51] S. V. Razavi-Termeh, K. Khosravi, A. Sadeghi-Niaraki, S. M. Choi, and V. P. Singh, "Improving groundwater potential mapping using metaheuristic approaches," *Hydrol. Sci. J.*, vol. 65, no. 16, pp. 2729–2749, 2020, doi: 10.1080/02626667.2020.1828589.

[52] N. Anđelić, S. B. Šegota, I. Lorencin, V. Mrzljak, and Z. Car, *Estimation of covid-19 epidemic curves using genetic programming algorithm*, vol. 27, no. 1. 2021.

[53] C. H. da Silva-Santos, P. R. Goulart, F. Bertelli, A. Garcia, and N. Cheung, "Nature inspired algorithms for the solution of inverse heat transfer problems applied to distinct unsteady heat flux orientations in cylindrical castings," *J. Intell. Manuf.*, 2022, doi: 10.1007/s10845-022-01935-y.

[54] E. Rashedi, H. Nezamabadi-pour, and S. Saryazdi, "GSA: A Gravitational Search

Algorithm," *Inf. Sci. (Ny).*, vol. 179, no. 13, pp. 2232–2248, 2009, doi: 10.1016/j.ins.2009.03.004.

[55] E. Eker, M. Kayri, S. Ekinci, and D. Izci, "A New Fusion of ASO with SA Algorithm and Its Applications to MLP Training and DC Motor Speed Control," *Arab. J. Sci. Eng.*, vol. 46, no. 4, pp. 3889–3911, 2021, doi: 10.1007/s13369-020-05228-5.

[56] E. Bottani, G. Casella, and T. Murino, "A hybrid metaheuristic routing algorithm for low-level picker-to-part systems," *Comput. Ind. Eng.*, vol. 160, no. June, p. 107540, 2021, doi: 10.1016/j.cie.2021.107540.

[57] S. Liu, Z. Zhang, C. Guan, J. Liu, and R. Dewil, "Mathematical formulation and a new metaheuristic for the constrained double-floor corridor allocation problem," *J. Manuf. Syst.*, vol. 61, no. August, pp. 155–170, 2021, doi: 10.1016/j.jmsy.2021.08.013.

[58] T. P. Shabeera, S. D. Madhu Kumar, S. M. Salam, and K. Murali Krishnan, "Optimizing VM allocation and data placement for data-intensive applications in cloud using ACO metaheuristic algorithm," *Eng. Sci. Technol. an Int. J.*, vol. 20, no. 2, pp. 616–628, 2017, doi: 10.1016/j.jestch.2016.11.006.

[59] M. F. Ab Aziz, S. A. Mostafa, C. F. Cik, M. A. Mohammed, M. Elhoseny, and A. Abualkishik, "Integrating Elman recurrent neural network with particle swarm optimization algorithms for an improved hybrid training of multidisciplinary datasets," *Expert Syst. Appl.*, vol. 183, no. May, p. 115441, 2021, doi: 10.1016/j.eswa.2021.115441.

[60] A. Gkoulalas-Divanis and V. S. Verykios, "Hybrid Algorithm," pp. 93–118, 2010, doi: 10.1007/978-1-4419-6569-1_16.

[61] M. H. Ali, A. M. A. Soliman, and S. K. Elsayed, "Optimal power flow using archimedes optimizer algorithm," *Int. J. Power Electron. Drive Syst.*, vol. 13, no. 3, pp. 1390–1405, 2022, doi: 10.11591/ijpeds.v13.i3.pp1390-1405.

[62] M. Papadimitrakis, N. Giamarelos, M. Stogiannos, E. N. Zois, N. A. I. Livanos, and A. Alexandridis, "Metaheuristic search in smart grid: A review with emphasis on planning, scheduling and power flow optimization applications," *Renew. Sustain. Energy Rev.*, vol. 145, no. April, p. 111072, 2021, doi: 10.1016/j.rser.2021.111072.

[63] K. Biswas, P. M. Vasant, J. A. G. Vintaned, and J. Watada, "A Review of Metaheuristic

Algorithms for Optimizing 3D Well-Path Designs," *Arch. Comput. Methods Eng.*, vol. 28, no. 3, pp. 1775–1793, 2021, doi: 10.1007/s11831-020-09441-1.

[64] D. Limon-Cantu and V. Alarcon-Aquino, "Multiresolution dendritic cell algorithm for network anomaly detection," *PeerJ Comput. Sci.*, vol. 7, 2021, doi: 10.7717/PEERJ-CS.749.

[65] L. Abualigah *et al.*, "Advances in meta-heuristic optimization algorithms in big data text clustering," *Electron.*, vol. 10, no. 2, pp. 1–29, 2021, doi: 10.3390/electronics10020101.

[66] O. N. Oyelade, A. E. S. Ezugwu, T. I. A. Mohamed, and L. Abualigah, "Ebola Optimization Search Algorithm: A New Nature-Inspired Metaheuristic Optimization Algorithm," *IEEE Access*, vol. 10, pp. 16150–16177, 2022, doi: 10.1109/ACCESS.2022.3147821.

[67] N. D. Lagaros, V. Plevris, and N. Ath, *The Mosaic of Metaheuristic Algorithms in Structural Optimization*, no. 0123456789. Springer Netherlands, 2022.

[68] H. Al-Khazraji, A. R. Nasser, and S. Khlil, "An intelligent demand forecasting model using a hybrid of metaheuristic optimization and deep learning algorithm for predicting concrete block production," *IAES Int. J. Artif. Intell.*, vol. 11, no. 2, pp. 649–657, 2022, doi: 10.11591/ijai.v11.i2.pp649-657.

[69] A. Kumar, Lekhraj, S. Singh, and A. Kumar, "Grey wolf optimizer and other metaheuristic optimization techniques with image processing as their applications: a review," *IOP Conf. Ser. Mater. Sci. Eng.*, vol. 1136, no. 1, p. 012053, 2021, doi: 10.1088/1757-899x/1136/1/012053.

[70] S. Chakraborty, A. K. Saha, S. Sharma, R. Chakraborty, and S. Debnath, "A hybrid whale optimization algorithm for global optimization," *J. Ambient Intell. Humaniz. Comput.*, vol. 2021, 2021, doi: 10.1007/s12652-021-03304-8.

[71] D. Wang, D. Tan, and L. Liu, "Particle swarm optimization algorithm: an overview," *Soft Comput.*, vol. 22, no. 2, pp. 387–408, 2018, doi: 10.1007/s00500-016-2474-6.

[72] J. Cai, "Based on DPC and PSO," vol. 8, 2020, doi: 10.1109/ACCESS.2020.2992903.

[73] Q. Tu, X. Chen, and X. Liu, "Multi-strategy ensemble grey wolf optimizer and its application to feature selection," *Appl. Soft Comput. J.*, vol. 76, pp. 16–30, 2019, doi: 10.1016/j.asoc.2018.11.047.

[74] S. Mirjalili, S. M. Mirjalili, and A. Lewis, “Grey Wolf Optimizer,” *Adv. Eng. Softw.*, vol. 69, pp. 46–61, 2014, doi: 10.1016/j.advengsoft.2013.12.007.

[75] W. chuan Wang, L. Xu, K. wing Chau, and D. mei Xu, “Yin-Yang firefly algorithm based on dimensionally Cauchy mutation,” *Expert Syst. Appl.*, vol. 150, p. 113216, 2020, doi: 10.1016/j.eswa.2020.113216.

[76] H. A. Ahmed, M. F. Zolkipli, and M. Ahmad, “A novel efficient substitution-box design based on firefly algorithm and discrete chaotic map,” *Neural Comput. Appl.*, vol. 31, no. 11, pp. 7201–7210, 2019, doi: 10.1007/s00521-018-3557-3.

[77] A. M. Altabeeb, A. M. Mohsen, and A. Ghallab, “An improved hybrid firefly algorithm for capacitated vehicle routing problem,” *Appl. Soft Comput. J.*, vol. 84, p. 105728, 2019, doi: 10.1016/j.asoc.2019.105728.

[78] S. Shekhawat and A. Saxena, “Development and applications of an intelligent crow search algorithm based on opposition based learning,” *ISA Trans.*, vol. 99, no. xxxx, pp. 210–230, 2020, doi: 10.1016/j.isatra.2019.09.004.

[79] S. Khalilpourazari and S. H. R. Pasandideh, “Sine–cosine crow search algorithm: theory and applications,” *Neural Comput. Appl.*, vol. 32, no. 12, pp. 7725–7742, 2020, doi: 10.1007/s00521-019-04530-0.

[80] S. Mirjalili, “SCA: A Sine Cosine Algorithm for solving optimization problems,” *Knowledge-Based Syst.*, vol. 96, pp. 120–133, 2016, doi: 10.1016/j.knosys.2015.12.022.

[81] Z. Yavo, Y. Haitman, J. M. Francos, and L. L. Scharf, “Matched Manifold Detection for Group-Invariant Registration and Classification of Images,” *IEEE Trans. Signal Process.*, vol. 69, pp. 4162–4176, 2021, doi: 10.1109/TSP.2021.3095723.

[82] X. Yin *et al.*, “Domain Progressive 3D Residual Convolution Network to Improve Low-Dose CT Imaging,” *IEEE Trans. Med. Imaging*, vol. 38, no. 12, pp. 2903–2913, 2019, doi: 10.1109/TMI.2019.2917258.

[83] Y. Chen *et al.*, “Structure-Adaptive Fuzzy Estimation for Random-Valued Impulse Noise Suppression,” *IEEE Trans. Circuits Syst. Video Technol.*, vol. 28, no. 2, pp. 414–427, 2018, doi: 10.1109/TCSVT.2016.2615444.

[84] Z. Chen, X. Jin, L. Li, and G. Wang, “A limited-angle CT reconstruction method based on anisotropic TV minimization,” *Phys. Med. Biol.*, vol. 58, no. 7, pp. 2119–2141, 2013,

doi: 10.1088/0031-9155/58/7/2119.

[85] F. A. Şenel, F. Gökçe, A. S. Yüksel, and T. Yiğit, “A novel hybrid PSO–GWO algorithm for optimization problems,” *Eng. Comput.*, vol. 35, no. 4, pp. 1359–1373, 2019, doi: 10.1007/s00366-018-0668-5.

[86] S. Prithi and S. Sumathi, “Automata Based Hybrid PSO–GWO Algorithm for Secured Energy Efficient Optimal Routing in Wireless Sensor Network,” *Wirel. Pers. Commun.*, vol. 117, no. 2, pp. 545–559, 2021, doi: 10.1007/s11277-020-07882-2.

[87] F. Bennis and R. Kumar, *Nature-Inspired Methods for Metaheuristics Optimization*, vol. 16. 2020.

[88] A. K. Ball, S. S. Roy, D. R. Kisku, N. C. Murmu, and L. dos S. Coelho, “Optimization of drop ejection frequency in EHD inkjet printing system using an improved Firefly Algorithm,” *Appl. Soft Comput. J.*, vol. 94, p. 106438, 2020, doi: 10.1016/j.asoc.2020.106438.

[89] S. K. Majhi, M. Sahoo, and R. Pradhan, “A space transformational crow search algorithm for optimization problems,” *Evol. Intell.*, vol. 13, no. 3, pp. 345–364, 2020, doi: 10.1007/s12065-019-00294-7.

[90] A. G. Hussien *et al.*, “Crow Search Algorithm: Theory, Recent Advances, and Applications,” *IEEE Access*, vol. 8, pp. 173548–173565, 2020, doi: 10.1109/access.2020.3024108.

[91] A. M. Anter, A. E. Hassenian, and D. Oliva, “An improved fast fuzzy c-means using crow search optimization algorithm for crop identification in agricultural,” *Expert Syst. Appl.*, vol. 118, pp. 340–354, 2019, doi: 10.1016/j.eswa.2018.10.009.

[92] Vasant J et al (2018) An unsupervised convolutional neural network-based algorithm for deformable image registration. Phys Med Biol 63(18):185017

[93] R. Fernandez-Beltran, F. Pla, and A. Plaza, “Intersensor Remote Sensing Image Registration Using Multispectral Semantic Embeddings,” *IEEE Geosci. Remote Sens. Lett.*, vol. 16, no. 10, pp. 1545–1549, 2019, doi: 10.1109/LGRS.2019.2904874.

[94] Chung M, Bernheim A, Mei X et al (2020) CT imaging features of 2019 novel coronavirus (2019-nCoV). Radiology 295(1):202–207

[95] N. Mansouri and M. M. Javidi, "A review of data replication based on meta-heuristics approach in cloud computing and data grid," *Soft Comput.*, vol. 24, no. 19, pp. 14503–14530, 2020, doi: 10.1007/s00500-020-04802-1.

[96] A. E. Hassanien, *Advances in Intelligent Systems and Computing 723 Mohamed Mostafa Editors The International Conference on Advanced Machine Learning Technologies and Applications (AMLTA2018)*. 2020.

[97] X. Yang, X. He, J. Zhao, Y. Zhang, S. Zhang, and P. Xie, "COVID-CT-Dataset: A CT Scan Dataset about COVID-19," pp. 1–5, 2020, [Online]. Available: http://arxiv.org/abs/2003.13865.

[98] M. J. White *et al.*, "Continuing undergraduate pathology medical education in the coronavirus disease 2019 (COVID-19) global pandemic the johns hopkins virtual surgical pathology clinical elective," *Arch. Pathol. Lab. Med.*, vol. 145, no. 7, pp. 814–820, 2021, doi: 10.5858/arpa.2020-0652-SA.

[99] G. Wang, X. Xu, X. Jiang, and S. Ding, "Medical image registration based on self-adapting pulse-coupled neural networks and mutual information," *Neural Comput. Appl.*, vol. 27, no. 7, pp. 1917–1926, 2016, doi: 10.1007/s00521-015-1985-x.

[100] Y. W. Chen, C. L. Lin, and A. Mimori, "Multimodal medical image registration using particle swarm optimization," *Proc. - 8th Int. Conf. Intell. Syst. Des. Appl. ISDA 2008*, vol. 3, pp. 127–131, 2008, doi: 10.1109/ISDA.2008.321.

[101] B.-W. Hwang, S. Kim, S.-W. Lee, D.-S. Huang, X.-P. Zhang, and G.-B. Huang, *Advances in Intelligent Computing*, vol. 3644, no. November. 2005.

[102] J. Chen, X. Li, L. Luo, X. Mei, and J. Ma, "Infrared and visible image fusion based on target-enhanced multiscale transform decomposition," *Inf. Sci. (Ny).*, vol. 508, pp. 64–78, 2020, doi: 10.1016/j.ins.2019.08.066.

[103] L. Caraffa, J. P. Tarel, and P. Charbonnier, "The guided bilateral filter: When the joint/cross bilateral filter becomes robust," *IEEE Trans. Image Process.*, vol. 24, no. 4, pp. 1199–1208, 2015, doi: 10.1109/TIP.2015.2389617.

[104] M. Wan *et al.*, "Total variation regularization term-based low-rank and sparse matrix representation model for infrared moving target tracking," *Remote Sens.*, vol. 10, no. 4, 2018, doi: 10.3390/rs10040510.

[105] P. Bergmann, S. Löwe, M. Fauser, D. Sattlegger, and C. Steger, “Improving unsupervised defect segmentation by applying structural similarity to autoencoders,” *VISIGRAPP 2019 - Proc. 14th Int. Jt. Conf. Comput. Vision, Imaging Comput. Graph. Theory Appl.*, vol. 5, pp. 372–380, 2019, doi: 10.5220/0007364503720380.

[106] B. Thai, M. Al-Nasrawi, G. Deng, and Z. Su, “Semi-guided bilateral filter,” *IET Image Process.*, vol. 11, no. 7, pp. 512–521, 2017, doi: 10.1049/iet-ipr.2016.0418.

[107] Y. Tian, Y. Li, and F. Ye, “Multimodal medical image fusion based on nonsubsampled contourlet transform using improved PCNN,” *Int. Conf. Signal Process. Proceedings, ICSP*, vol. 0, pp. 799–804, 2016, doi: 10.1109/ICSP.2016.7877941.

[108] H. Kaur, S. Kumar, K. S. Behgal, and Y. Sharma, “Multi - Modality Medical Image Fusion Using Cross - Bilateral Filter and Neuro - Fuzzy Approach,” pp. 263–277, 2021, doi: 10.4103/jmp.JMP.